

**A Precision Search for Exotic Scalar and Tensor Couplings in
the Beta Decay of Polarized ^{37}K**

by

Melissa Anholm

A Thesis submitted to the Faculty of Graduate Studies of
The University of Manitoba
in partial fulfillment of the requirements of the degree of

DOCTOR OF PHILOSOPHY

Department of Physics and Astronomy
University of Manitoba
Winnipeg

Abstract

Abstract Goes Here

Acknowledgements

People to acknowledge here include: John Behr, Gerald Gwinner, Dan Melconian.
Also: Spencer Behling, Ben Fenker. Also-also: Alexandre Gorelov, James McNeil.
But additionally: Danny Ashery.

Contents

Abstract	ii
Acknowledgements	iii
Contents	vi
List of Figures	vii
List of Tables	x
1 Background and Introduction	1
1.1 Motivation	1
1.2 The Basics of Beta Decay	1
1.3 Mathematical Formalism	2
1.4 Our Decay	3
1.5 Shake-off Electron Spectrum	3
1.6 Fierz Interference – The Physical Signature	4
1.7 On the Superratio, the Supersum, and the Constructed Asymmetry .	5
2 Considerations and Implementation of Atomic Techniques	7
2.1 An Overview of Magneto-Optical Traps	7
2.1.1 Zeeman Splitting	8
2.1.2 Saturation Spectroscopy	8
2.1.3 Doppler Cooling	10
2.1.4 Atom Trapping with a MOT	10
2.2 Optical Pumping	12
2.3 An Overview of the Double MOT System and Duty Cycle	13
2.4 The AC-MOT and Polarization Setup	15
2.5 Measurement Geometry and Detectors	18
2.6 The Photoionization Laser	21

3	Calibrations and Data Selection	24
3.1	Measurements of the Atom Cloud	24
3.1.1	Measurements with the rMCP	25
3.1.2	Measurements with the eMCP	27
3.2	Data Selection and Preliminary Cuts	28
3.3	Further Cuts Using the DSSD	31
3.4	Further Cuts Using the eMCP	32
4	Simulations	40
4.1	Considerations for Software Upgrade Implementation	40
4.2	The Simple Monte Carlo and Response Function	42
4.3	Simulating the Background	49
4.4	Comparing Simulations with Experimental Data	52
5	Analysis and Estimates of Systematic Effects	55
5.1	Overview	56
5.2	BB1 Radius, Energy Threshold, Agreement	56
5.3	Background Modeling – Decay from Surfaces within the Chamber . .	57
5.4	Quantifying the Effects of Backscatter with Geant4	57
5.5	Lineshape Reconstruction	57
5.5.1	Motivation	58
5.5.2	What is it and how does it work?	58
5.5.3	The Math-Specifics	59
5.5.4	The Results – Things That Got Evaluated This Way	60
5.5.5	The low-energy tail uncertainty, and what it does	60
6	Results and Conclusions	63
6.1	Measured Limits on b_{Fierz}	63
6.2	Discussion of Corrections and Uncertainties	63
6.3	Relation to Other Measurements and New Overall Limits	63
6.4	R_{slow} and Other Possible Future Work for the Collaboration	63
6.4.1	Motivation	64
6.4.2	The Decay Process	66
6.4.3	Current Status	67
6.5	Conclusions	67
	Bibliography	68
	Appendices	72

A Notable Differences in Data Selection between this and the Previous Result	72
A.1 Polarization Cycle Selection	72
A.2 Leading Edge / Trailing Edge and Walk Correction	72
A.3 TOF Cut + Background Modelling	72
A.4 BB1 Radius	73
B A PDF	74
B.1 JTW	74
B.2 Holstein	76
C Notation	82
C.1 Comparison Guide	82
C.2 Imported from Another Appendix	82
D SuperRatio	92
E Old SuperRatio	94
F Old Super Corrections	96

List of Figures

1.1	A level diagram for the decay of ^{37}K	4
1.2	Levinger TOF	5
1.3	Here's why it's better to extract b_{Fierz} from an asymmetry, in this case.	6
2.1	Components of a magneto-optical trap, including current-carrying magnetic field coils and counterpropagating circularly polarized laser beams. Diagram taken from [2]	11
2.2	An atomic level diagram for the optical pumping of ^{37}K , taken from [1].	12
2.3	The TRINAT experimental set-up, viewed from above. The two MOT system reduces background in the detection chamber. Funnel beams along the atom transfer path keep the atoms focused.	13
2.4	The duty cycle used for transferring, cooling, trapping, and optically pumping ^{37}K during the June 2014 experiment. Not drawn to scale. Question marks indicate timings that varied either as a result of electronic jitter or as a result of variable times to execute the control code. Atoms are transferred during operation of the DC-MOT. Though the push beam laser itself is only on for 30 ms, the bulk of the DC-MOT's operation time afterwards is needed to collect and cool the transferred atoms. After 100 on/off cycles of optical pumping and the AC-MOT, the DC-MOT resumes and the next group of atoms is transferred in. After 16 atom transfers, the polarization of the optical pumping laser is flipped to spin-polarize the atoms in the opposite direction, in order to minimize systematic errors.	15
2.5	One cycle of trapping with the AC-MOT, followed by optical pumping to spin-polarize the atoms. After atoms are transferred into the science chamber, this cycle is repeated 100 times before the next transfer. The magnetic dipole field is created by running parallel (rather than anti-parallel as is needed for the MOT) currents through the two coils.	16

2.6	A decay event within the TRINAT science chamber. After a decay, the daughter will be unaffected by forces from the MOT. Positively charged recoils and negatively charged shake-off electrons are pulled towards detectors in opposite directions. Although the β^+ is charged, it is also highly relativistic and escapes the electric field with minimal perturbation.	19
2.7	Inside the TRINAT science chamber. This photo is taken from the vantage point of one of the microchannel plates, looking into the chamber towards the second microchannel plate. The current-carrying copper Helmholtz coils and two beta telescopes are visible at the top and bottom. The metallic piece near the center is one of the electrostatic ‘hoops’ used to generate an electric field within the chamber. The hoop’s central circular hole allows access to the microchannel plate, and the two elongated holes on the sides allow the MOT’s trapping lasers to pass unimpeded at an angle of 45 degrees ‘out of the page’. . .	23
3.1	Trap Position along TOF Axis	25
3.2	Trap Position from Camera	26
3.3	Vertical Trap Position from rMCP	27
3.4	rMCP Calibration	28
3.5	Position as measured on the eMCP, after some data cleaning.	33
3.6	Beta-electron TOF, for events with and without eMCP hit position information. A cut will eventually be taken to accept only events sufficiently near the largest peak – in this case the number of events is ‘only’ decreased by a factor of 2.	34
3.7	SOE TOF peaks (eMPC - Scintillator), using the leading edge (LE) and using the trailing edge (TE). Data is sorted according to sunset. For each individual sunset, the TE peak is broader than the LE peak. The centroid of each sunset is also more variable in the TE plots. . .	35
3.8	SOE TOF walk, before (left) and after (right) applying a quartic adjustment to straighten out the effective TOF.	36
3.9	SOE TOF, model and data. In the end, I cut the data to use only events with a TOF between -0.928 ns and +1.416 ns. Max. possible background is like a factor of two too big. Similar quality results no matter how you distribute the Levinger spectra between 4S and 3P, however adding the 0 eV electrons makes a big improvement to the agreement.	37
3.10	Experimental Scintillator Spectra	38
3.11	The superratio asymmetry, averaged over all scintillator energies between 400-4800 keV, is used to compare the experimental data and simulated TOF model as a proxy for the quality of the model to estimate the background. All other cuts have been applied.	39

4.1	Fit to Mono-Energetic Spectrum, 5000 keV	44
4.2	Fit to Mono-Energetic Spectrum, 3000 keV	45
4.3	Fit to Mono-Energetic Spectrum, 1500 keV	46
4.4	Fit to Mono-Energetic Spectrum, 1000 keV	47
4.5	Fit to Mono-Energetic Spectrum, 750 keV	48
4.6	Lineshape Parameter Fits (Part 1)	50
4.7	Lineshape Parameter Fits (Part 2)	51
4.8	Lineshape Parameter Fits (Part 3)	52
4.9	Lineshape Parameter Fits (Part 4)	53
4.10	Goodness of Fit for Modeled Lineshapes	53
5.1	Simulated Beta TOA vs emission angle w.r.t. detector orientation . .	58
5.2	Lineshape Comparison	59
5.3	A_β Position Error	60
5.4	b_{Fierz} Position Error	61
6.1	A superratio asymmetry from the data, and the best fit from simulations.	64
6.2	Some results. I'll want to show at least one of these things. Probably show a separate one for each runset, actually.	65
C.1	"Notes 0"	86
C.2	"Notes 1"	87
C.3	"Notes 2"	88
C.4	"Notes 3"	89
C.5	"Notes 4"	90
C.6	"Notes 5"	91

List of Tables

3.1	Cloud Position and Size	24
3.2	List of Runs	29
3.3	List of Electron Runs	30
5.1	Error Budget	56
C.1	Kinematic Terms Guide	83
C.2	Angular Momentum Notation	83
C.3	Multipole Notation	84
C.4	Selected Integrals from Holstein's Eq. (51)	85

Chapter 1

Background and Introduction

1.1 Motivation

The nuclear weak force is one of four fundamental forces described within physics. It mediates the process of beta decay, which is of particular interest to us here. Although beta decay is generally well understood, it presents a unique opportunity to search for physics beyond the Standard Model within the behaviour of the weak coupling. By observing the kinematics and angular correlations involved in the decay process, one gains access to a wealth of information about the precise form of the operators mediating the decay.

According to the predictions of the Standard Model, beta decay involves only so-called vector (V) and axial-vector (A) couplings, with a relative phase angle producing the left-handed “(V–A)” form of the interaction. There exists an extensive body of experimental evidence to demonstrate that this is overall a very good description of the beta decay process. Despite the success of the (V–A) model, the additional presence of certain other “exotic” couplings cannot be entirely ruled out, and our observable is mostly sensitive to scalar (S) and tensor (T) couplings.

1.2 The Basics of Beta Decay

Standard Model beta decay is well understood. The Fermi description of beta decay can be found in any nuclear physics textbook, but you have to dig slightly harder to understand Gamow-Teller or mixed decays, all of which are relevant here.

via Krane [13] Under the Allowed Approximation, we require that a beta decay may not carry away any orbital angular momentum, because we treat the nucleus as pointlike and work in the CM frame. An Allowed decay can, however, change the total nuclear angular momentum, because the outgoing leptons have spin= 1/2 and therefore carry angular momentum. Therefore, in an allowed decay, the total nuclear angular momentum must always change by either 0 or 1.

From a 2006 paper by Severijns et al [14], the selection rules for an allowed transition are:

$$\Delta I = I_f - I_i = \{0, \pm 1\} \quad (1.1)$$

$$\hat{\Pi}_i \hat{\Pi}_f = +1 \quad (1.2)$$

Then, you can separate the allowed transitions into singlet (anti-parallel lepton spins, $S = 0$ – a Fermi transition) and triplet states (parallel lepton spins, $S = 1$ – a Gamow-Teller transition).

Fermi decays are so-called “vector” interactions, and happen when the spin of the two leptons involved are antiparallel, so there can be no change in angular momentum (at least in the case of the Allowed approximation).

Gamow-Teller decays involve two leptons with parallel spins, so the decay must change the projection of the nuclear angular momentum, M_I , by exactly one unit (in the case of the Allowed approximation). They transition may or may not simultaneously change the total nuclear spin, I , by one unit. These are “axial-vector” interactions. (Note that $I = 0 \rightarrow I = 0$ interactions are never Gamow-Teller decays.

Probably everything in this section is yoinked from [15], pg 212.

1.3 Mathematical Formalism

In order to proceed with a measurement, we must find a master equation to describe the probability of beta decay events with any given distribution of energy and momenta among the daughter particles, as a function of the strength of the specific couplings of interest to us. To do this, two sets of formalisms are combined – the older formalism from Jackson, Treiman, and Wylde (JTW) [5], [16], which describes the effects of all types of Standard Model and exotic couplings of interest to us here, but

which truncates its expression at first order in the (small) parameter of recoil energy, and a newer formalism from Holstein [17], which includes terms up to several orders higher in recoil energy, but which does not include any description of the exotic couplings of particular interest to us. We note that because any exotic couplings present in nature have already been determined to be either small or nonexistent, it is sufficient to describe these parameters with expressions truncated at first order, despite the fact that it is still necessary to describe the larger Standard Model couplings with higher-order terms.

The procedure for combining the two formalisms is described in detail in Appendix B. Integrating the JTW expression over neutrino direction, we find:

$$\begin{aligned} d^3\Gamma dE_\beta d^3\hat{\Omega}_\beta &= \frac{2}{(2\pi)^4} F_\mp(Z, E_\beta) p_\beta E_\beta (E_0 - E_\beta)^2 dE_\beta d^3\hat{\Omega}_\beta \xi \\ &\times \left[1 + b_{\text{Fierz}} \frac{m_e c^2}{E_\beta} + A_\beta \left(\frac{\vec{J}}{J} \cdot \frac{\vec{p}_\beta}{E_\beta} \right) \right], \end{aligned} \quad (1.3)$$

where

$$\xi = G_v^2 \cos \theta_C f_1(E). \quad (1.4)$$

1.4 Our Decay

Here, we focus on the decay ${}^{37}\text{K} \rightarrow {}^{37}\text{Ar} + \beta^+ + \nu_e$. The angular correlations between the emerging daughter particles provide a rich source of information about the type of interaction that produced the decay. Among other useful properties, this is a ‘mirror’ decay, meaning that the nuclear wavefunctions of the parent and daughter are identical up to their isospin quantum number. This property allows us to place strong constraints on the size of the theoretical uncertainties for this decay process within the Standard Model.

1.5 Shake-off Electron Spectrum

Shake-off electrons: where do they come from, and where do they go? [6]. John made some nice plots of these from the eMCP data. I did *not* use it to make

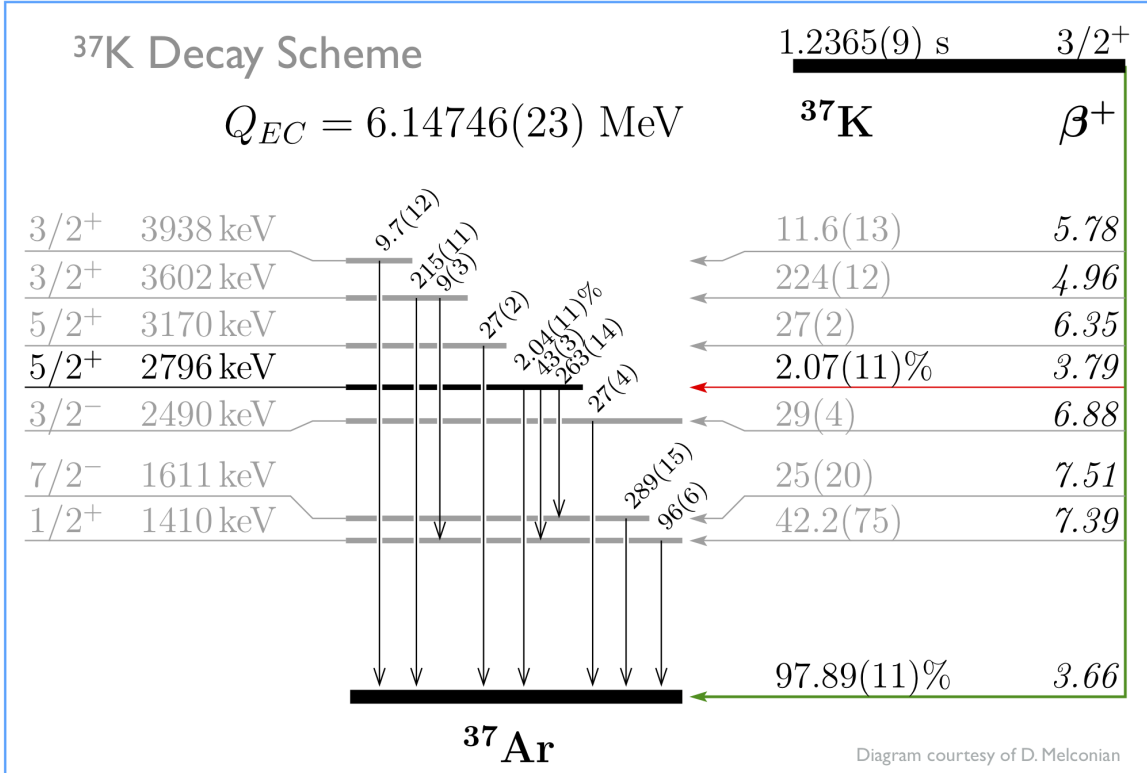


Figure 1.1: A level diagram for the decay of ^{37}K .

a cut on eMCP hit position in the end, despite the fact that it makes the spectrum more clean, because a lot of good events don't have full hit position information, and you lose an awful lot of statistics by making the cut. I used this for modeling the background spectrum, but in the end it wasn't as elegant a result as I might have hoped. Also, it's still an open question exactly which fraction of SOEs come from which atomic shell, but it doesn't change the resulting spectrum very much.

1.6 Fierz Interference – The Physical Signature

The physical effects resulting from the presence of scalar or tensor couplings include a small perturbation to the energy spectrum of betas produced by radioactive decay.

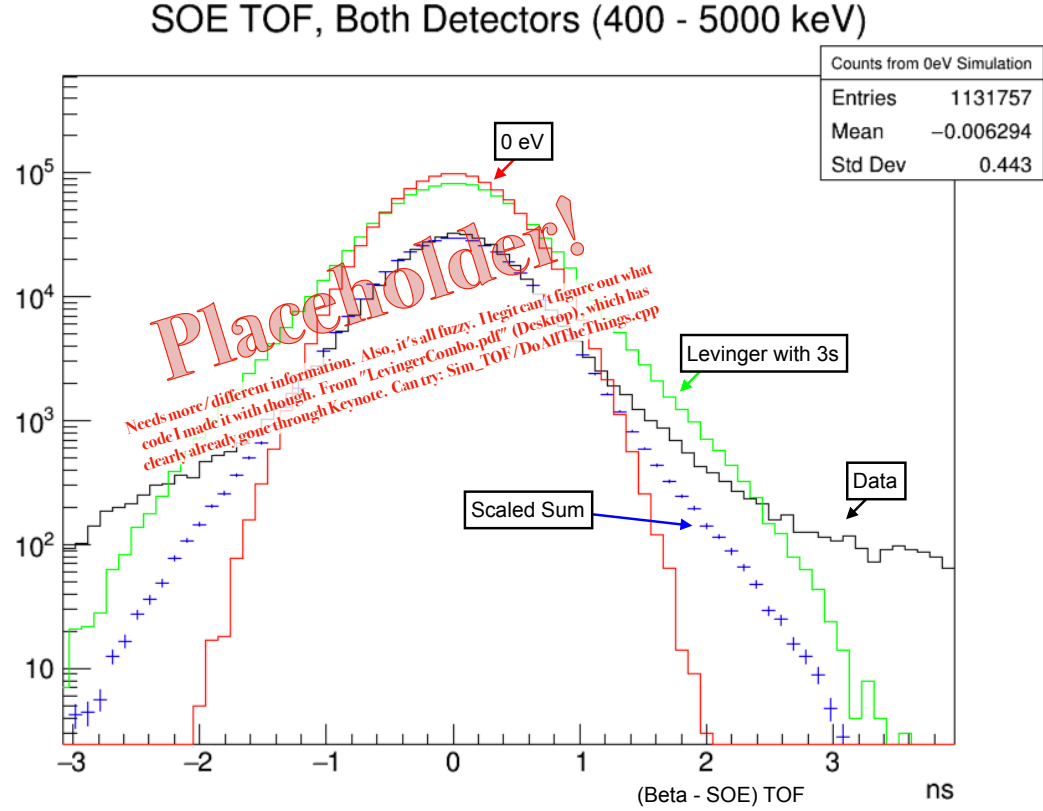


Figure 1.2: Shake-off electron TOF (w.r.t. beta TOA) spectrum, showing how the spectrum is different if one includes different sets of initial electrons to be shaken off. I forget why some of them have 0 eV. Maybe those are the ones from the $^{37}\text{Ar}^+$ Levinger TOF spectra for some different sets of SOE initial orbitals before shake-off. (At least that's what it's supposed to be, after I fix the picture). It's reconstructed event-by-event with beta times-of-flight that would pass some basic 'good event' cuts. Anyway, it turns out, it doesn't much matter what orbitals you lose SOEs from. That's nice. In the end, I used 85+15. (Need to re-plot this.)

1.7 On the Superratio, the Supersum, and the Constructed Asymmetry

The data can be combined into a superratio asymmetry. This has the benefit of causing many systematics to cancel themselves out at leading order. It also will increase the fractional size of the effects we're looking for. This can be shown by using math.

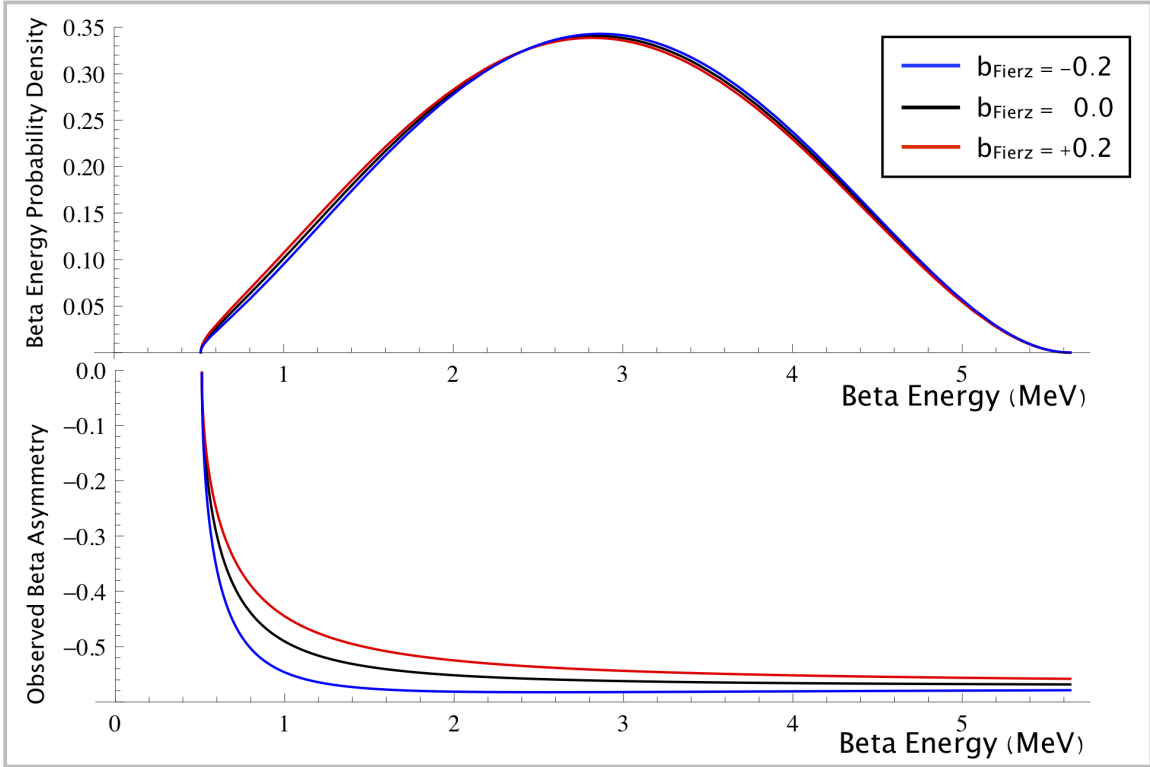


Figure 1.3: Here's why it's better to extract b_{Fierz} from an asymmetry, in this case.

Not all systematics effects are eliminated. We'll want to be careful to propagate through any effects that are relevant. Using the superratio asymmetry as our physical observable makes this process a bit messier for the things that don't cancel out, but it's all just math. Some other groups have performed similar measurements using the supersum as the physical observable. There are pros and cons to both methods. I can show, using a back-of-the-envelope calculation, that for this particular dataset, the superratio asymmetry method produces a better result.

Chapter 2

Considerations and Implementation of Atomic Techniques

2.1 An Overview of Magneto-Optical Traps

Since its initial description by Raab et. al. in 1987 [18], the magneto-optical trap (MOT) has become a widely used technique in many atomic physics laboratories. The MOT produces confined samples of cold, electrically neutral and isotopically pure atoms confined within a small spatial region. It is these properties that make the MOT a valuable tool not only in atomic physics, but for precision measurements in nuclear physics as well, and the TRINAT lab has adopted the technique wholeheartedly.

The technique is used predominantly with alkalis due to their simple orbital electron structure, and once set up it is quite robust. The MOT's trapping force is specific to the isotope for which the trap has been tuned. This feature makes it ideal for use in precision radioactive decay experiments, since the daughters are unaffected by the trapping forces keeping the parent confined.

A typical MOT can be created from relatively simple components: a quadrupole-shaped magnetic field, typically generated by two current-carrying coils of wire, and a circularly polarized laser tuned to match one or more atomic transitions in the isotope of interest. Because a MOT is easily disrupted by interactions with untrapped atoms, the trap must be created within a vacuum system. Finally, a source of atoms to be trapped is required. [See Fig. 2.1.]

The laser, which must be circularly polarized in the appropriate directions and

tuned slightly to the red of an atomic resonance, is split into three perpendicular retroreflected beams, doppler cooling the atoms and (with the appropriate magnetic field) confining them in all three dimensions (see Figure 2.1).

2.1.1 Zeeman Splitting

In the presence of an external magnetic field \vec{B} , the Hamiltonian associated with an atom's orbital electrons will acquire an additional “Zeeman Shift” term, given by [19]

$$H_{\text{Zeeman}} = -\vec{\mu} \cdot \vec{B}, \quad (2.1)$$

where $\vec{\mu}$ is the magnetic moment associated with the orbital under consideration. In the limit where the magnetic field is too weak to significantly disrupt the coupling between the electron's spin- and orbital angular momenta, $\vec{\mu}$ may be treated as being fixed with respect to changes in the magnetic field. It is this weak field regime which will be primarily of interest to us in work with magneto-optical traps.

With $\vec{\mu}$ fixed, it is clear that the magnitude of the energy shift must scale linearly with the strength of the magnetic field. In considering the perturbation to the energy of a particular *transition*, the perturbations to the initial and final states must of course be subtracted:

$$\Delta E_{\text{transition}} = -(\vec{\mu}_f - \vec{\mu}_i) \cdot \vec{B}. \quad (2.2)$$

2.1.2 Saturation Spectroscopy

Consider a single two-level atom in its ground state interacting with a single photon with the same energy as that of the atomic transition between the ground and excited states. If angular momentum selection rules allow it, the photon will be absorbed and the atom will receive a “push” from the incident photon's momentum. After a time, the atom will spontaneously de-excite by emitting a photon in a random direction. Conservation of momentum results in the atom receiving a second push from the emitted photon.

If one considers a cloud of many such atoms within the path of a correctly-tuned (low intensity) laser beam, then provided the atoms are constrained to remain within

the beam path, the result of many such interactions is a biased random walk in physical space for each individual atom, and a net velocity change for the cloud as a whole.

In contrast to the above description of absorption followed by spontaneous emission, a photon interacting with an atom in the excited state may cause the atom to de-excite by emitting a second photon. This mechanism is negligible in the case of a sufficiently low intensity laser beam. However, as the laser intensity increases, so too will the fraction of atoms in the excited state at any given time. As it is only the excited state atoms that are able undergo stimulated emission, this effect becomes increasingly dominant as the intensity of the incident laser increases. In the limit of infinite intensity, stimulated emission and absorption are equally likely to occur, and therefore the population is split evenly between the ground and excited states.

To describe the regime change between atomic interactions with low intensity- and high intensity lasers, we introduce the (on-resonance) saturation intensity, I_{sat} , where

$$I_{\text{sat}} = \frac{\hbar\omega_0^3\gamma}{12\pi c^2} \quad (2.3)$$

is the laser intensity at which the rates of decay by stimulated- and spontaneous emission are equal, $\hbar\omega_0$ is the energy of both the atomic transition and γ describes the linewidth of the atomic transition and equivalently its rate of spontaneous decay from its excited state. We may further define the on-resonance saturation parameter s_0 , for a laser of intensity I as,

$$s_0 := \frac{I}{I_{\text{sat}}} \quad (2.4)$$

In practice, for the project that is the topic of this thesis, the MOT laser operates at about 1/2 of saturation intensity, while the optical pumping and photoionization lasers operate at considerably lower than saturation intensity. However, one can gain a qualitative understanding of many aspects of atom-laser interaction while neglecting saturation concerns.

2.1.3 Doppler Cooling

We now consider a somewhat more general case in which a cloud of two-level atoms lies along the path of two counter-propagating laser beams, both detuned slightly to the red of resonance. For simplicity, this cloud will be treated as being constrained in the other two dimensions such that it must within the laser's path. With two counter-propagating laser beams of equal intensity and detuning, the “push” from interaction with one beam is exactly counteracted by the push from the opposite-propagating beam, and there is no net velocity transfer to the cloud.

Detuning the laser from resonance will of course decrease absorption upon interacting with an atom at rest – however the atoms within the cloud are not at rest, but rather are undergoing thermal motion. As such, within the rest frame of each individual atom, the two laser beams will appear to be Doppler shifted in opposite directions, with the sign dependent on atomic motion. In particular, atoms moving against a laser's direction of propagation will see that laser beam as being blueshifted. Since the laser has been red-detuned within the lab frame, the blueshift moves the laser frequency as seen by the atom back toward resonance, and makes its photons more likely to be absorbed. Similarly, for an atom moving in the same direction as a red-detuned laser beam, this laser will be seen as further red-shifted, and absorption likelihood is decreased. Because of the difference in absorption, such an atom becomes more likely to receive a push back against its (lab frame) direction of motion, slowing it down, and less likely to receive a push to increase its lab frame speed.

The overall effect on a one-dimensional cloud of atoms in the path of two counter-propagating red-detuned lasers is that the atoms will be slowed and cooled. Such a setup is sometimes referred to as a one-dimensional “optical molasses” due to the viscous drag force induced on atomic motion. It is straightforward to extend this model to three dimensions. Although this setup will decrease atomic velocity, it does not include a confining force, so the atoms are still free to move out of the lasers' path, albeit at a decreased speed.

2.1.4 Atom Trapping with a MOT

Really, at the end of the previous section, I described the MOT's trapping mechanism. That's literally what it is. You just need to do it in 3 dimensions, rather than only one. Fortunately, an anti-helmholz(sp?) coil gives us a quadrupole-shaped

magnetic field, which *actually* has a magnetic field that changes linearly along any axis in the region near the center.

Optical molasses + zeeman splitting = magneto-optical trap. Anyway, see Fig. 2.1.

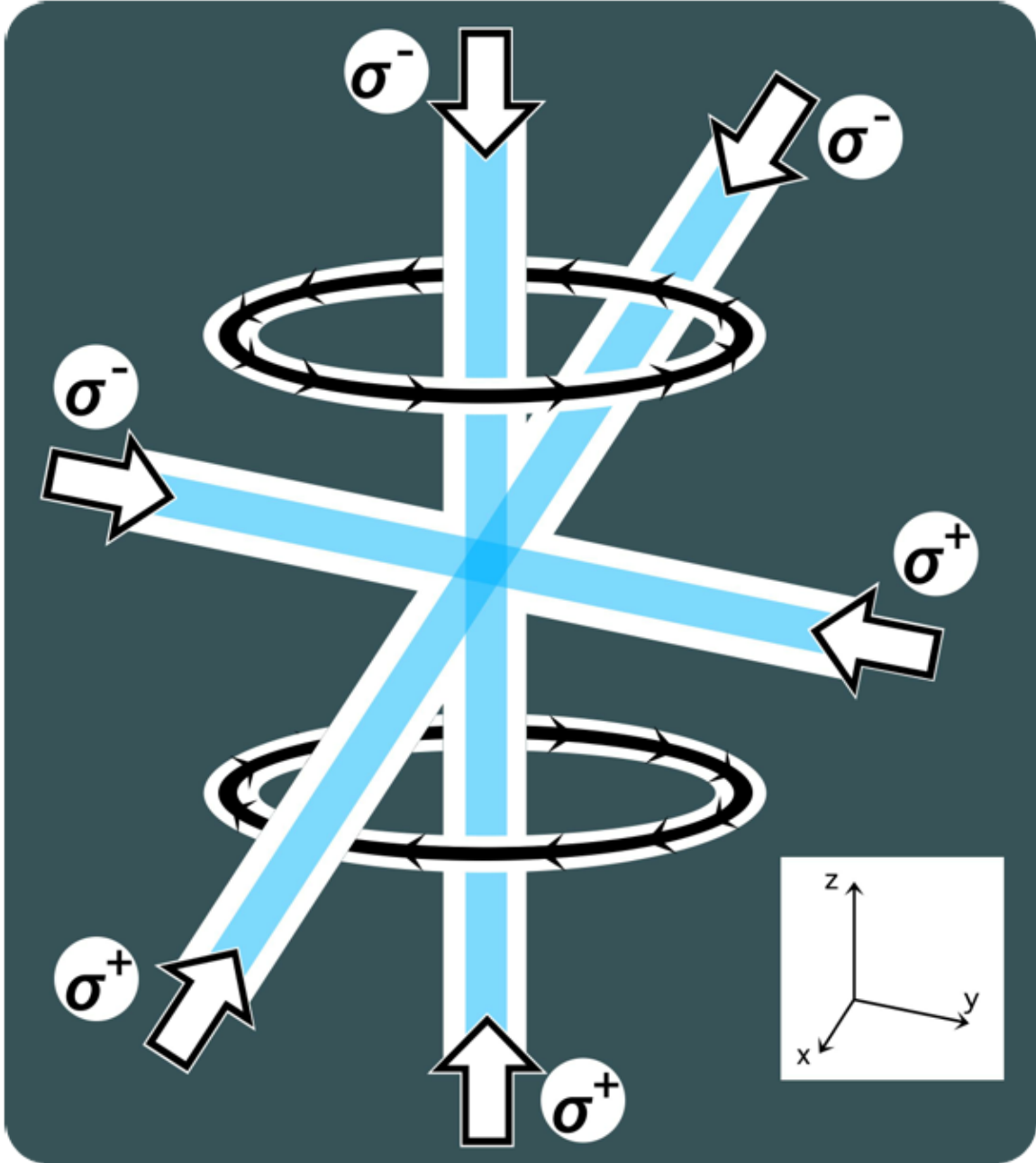


Figure 2.1: Components of a magneto-optical trap, including current-carrying magnetic field coils and counterpropagating circularly polarized laser beams. Diagram taken from [2]

2.2 Optical Pumping

The optical pumping process is described in detail in our collaboration's Ref. [1]. The main detail described here is that the optical pumping is disturbed by any component of magnetic field not along the quantization axis. (Ours is the vertical axis, defined by the direction of the optical pumping light, and along which the detectors are placed.) This required sophistication with an AC MOT described below.

Need a nice, uniform, constant magnetic field for your polarization to larmor precess around. Then, however depolarized (from the axis of the magnetic field) you were to start out, you don't like precess in a way that changes the projection you care about.

But also, I should actually describe the optical pumping, too. And point at Ben's OP paper that we did [1].

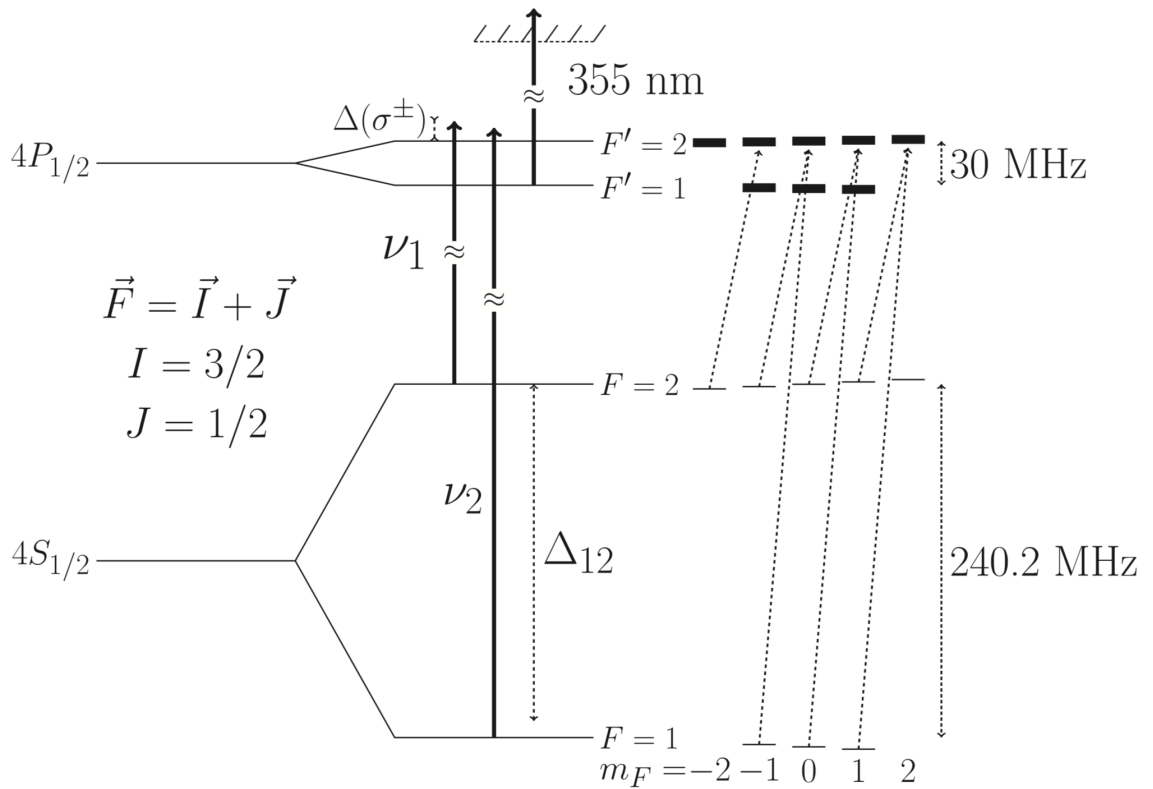


Figure 2.2: An atomic level diagram for the optical pumping of ^{37}K , taken from [1].

2.3 An Overview of the Double MOT System and Duty Cycle

The experimental subject matter of this thesis was conducted at TRIUMF using the apparatus of the TRIUMF Neutral Atom Trap (TRINAT) collaboration. The TRINAT laboratory offers an experimental set-up which is uniquely suited to precision tests of Standard Model beta decay physics, by virtue of its ability to produce highly localized samples of cold, isotopically pure atoms within an open detector geometry. Although the discussion in this chapter will focus on the methodologies used to collect one particular dataset, taken over approximately 7 days of beamtime in June 2014, the full apparatus and the techniques used are fairly versatile, and can be (and have been) applied to several related experiments using other isotopes.

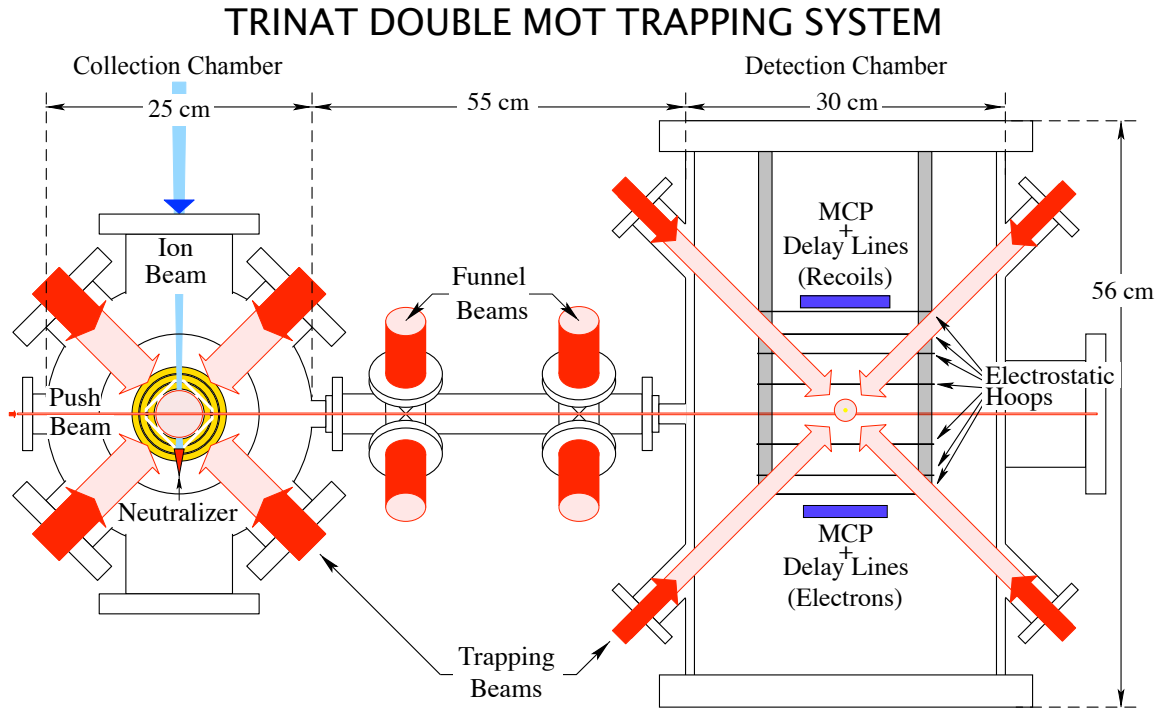


Figure 2.3: The TRINAT experimental set-up, viewed from above. The two MOT system reduces background in the detection chamber. Funnel beams along the atom transfer path keep the atoms focused.

The TRINAT lab accepts radioactive ions delivered by the ISAC beamline at TRIUMF. These ions are collected on the surface of a hot zirconium foil where they are electrically neutralized, and subsequently escape from the foil into the first of two ex-

perimental chambers (the “collection chamber”). Further details on the neutralization process are presented in a previous publication [20]. Within the collection chamber, atoms of one specific isotope – for the purposes of this thesis, ^{37}K – are continuously collected into a magneto-optical trap from the tail end of the thermal distribution. Although this procedure preferentially traps only the slowest atoms, once trapped, atoms will be cooled further as a side-effect of the MOT’s trapping mechanism. The result is a small (~ 1 mm diameter), cold (~ 1 mK) cloud of atoms of a particular isotope.

These properties of the atomic cloud allow for a relatively clean transfer of linear momentum from an appropriately tuned laser beam to the atoms within the cloud, and we use this mechanism to “push” the atoms out of the collection MOT and into the “detection chamber”, where they are loaded into a second MOT (see Fig. 2.3). During regular operation, atoms are transferred approximately once per second.

There is no need to release previously trapped atoms in the second MOT when a new group of atoms is loaded. Although the trap loses atoms over time as a result of a variety of physical processes, during typical operation the majority of atoms loaded in a given transfer will still be trapped at the time the next set of atoms is loaded, and after several transfer cycles, something like a steady state is obtained.

Because the transfer and trapping mechanisms rely on tuning laser frequencies to specific atomic resonances, these mechanisms act on only a single isotope, and all others remain unaffected. The result is a significant reduction of background contaminants within the detection chamber relative to initial beamline output. The transfer methodology is discussed in some detail within another publication [21].

We now turn our attention to what happens to the atom cloud in the detection chamber between loading phases (see Fig. 2.4). One of the goals for the 2014 ^{37}K beamtime required that the atom cloud must be spin-polarized, as well as being cold and spatially confined. Although the MOT makes it straightforward to produce a cold and well confined cloud of atoms, it is fundamentally incompatible with techniques to polarize these atoms. The physical reasons behind this are discussed in Section 2.4.

Once the newly transferred set of ^{37}K atoms has been collected into the cloud, the entire MOT apparatus cycles 100 times between a state where it is ‘on’ and actively confining atoms, and a state where it is ‘off’ and instead the atoms are spin-polarized by optical pumping while the atom cloud expands ballistically before being re-trapped. These 100 on/off cycles take a combined total of 488 ms. The laser components of

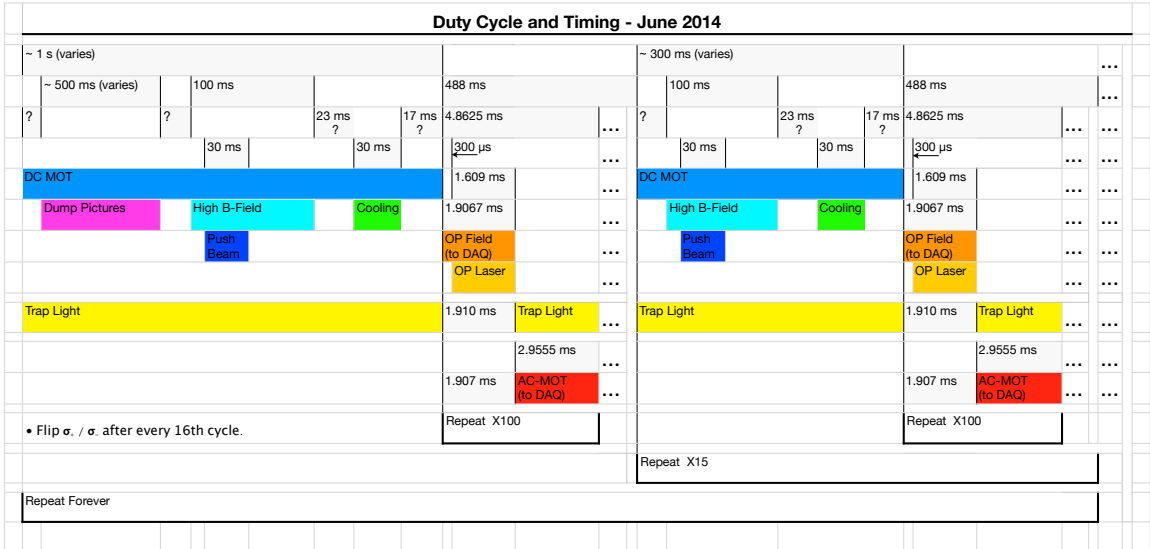


Figure 2.4: The duty cycle used for transferring, cooling, trapping, and optically pumping ^{37}K during the June 2014 experiment. Not drawn to scale. Question marks indicate timings that varied either as a result of electronic jitter or as a result of variable times to execute the control code. Atoms are transferred during operation of the DC-MOT. Though the push beam laser itself is only on for 30 ms, the bulk of the DC-MOT's operation time afterwards is needed to collect and cool the transferred atoms. After 100 on/off cycles of optical pumping and the AC-MOT, the DC-MOT resumes and the next group of atoms is transferred in. After 16 atom transfers, the polarization of the optical pumping laser is flipped to spin-polarize the atoms in the opposite direction, in order to minimize systematic errors.

the trap are straightforward to cycle on and off on these timescales, but the magnetic field is much more challenging to cycle in this manner.

Immediately following each set of 100 optical pumping cycles, another set of atoms is transferred in from the collection chamber to the detection chamber, joining the atoms that remain in the trap (see Fig. 2.4). The details of the trapping and optical pumping cycles are described further in Section 2.4, and the optical pumping technique and its results for this beamtime are the subject of a recent publication [1].

2.4 The AC-MOT and Polarization Setup

Citation for Harvey and Murray goes here [7]. Also, myself [2].

Here's a diagram of our AC-MOT running one AC-MOT/OP cycle, in Fig. 2.5.

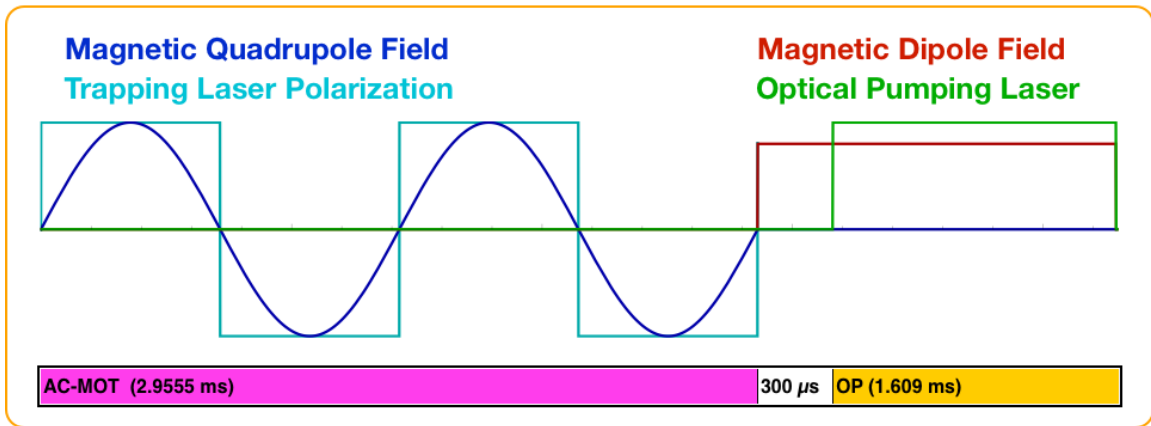


Figure 2.5: One cycle of trapping with the AC-MOT, followed by optical pumping to spin-polarize the atoms. After atoms are transferred into the science chamber, this cycle is repeated 100 times before the next transfer. The magnetic dipole field is created by running parallel (rather than anti-parallel as is needed for the MOT) currents through the two coils.

Normal MOTs are DC-MOTs. They just sort-of go. It's continuous. We used an AC-MOT though! The point of an AC-MOT is to shut off the magnetic field as quickly as possible. With a well-controlled and uniform magnetic field, we can optically pump the atoms, which I think I'm going to describe in the upcoming section (2.2).

Sadly, this also removes our trapping mechanism. We could keep the optical molasses after the field is off if we wanted to, but we don't, because we wouldn't be able to optically pump the atoms then. But at least the atoms are cold-ish (we can measure! I think it's done indirectly in that one table, or for realsies in Ben's thesis), so we can let them just chill for a little while before we have to re-trap them. Don't lose too much.

Anyway, the idea of the AC-MOT is to run a sinusoidal current through your anti-Helmholtz coils. You'll get eddy currents in your nearby metal *stuff* when you have a changing current, and those will *also* make a magnetic field. So, the idea with an AC-MOT is that with a sinusoid, you have clear control over what the eddy currents are actually doing, and you can just shut the current off when the eddy currents are zero (current in the anti-Helmholtz coils will be close to zero at this time too, depending on frequency of the sinusoid...), so you can reduce the size of the eddy currents by like an order of magnitude. Eddy currents in general take a while to die away, so it's good to make them as small as possible. ...Also, eddy currents making a

magnetic field will screw up your optical pumping, because um, reasons? I think it's not just the detuning, it's also something about the Larmor precession.

As alluded to in the previous section (2.3), the measurement in question required a spin-polarized sample of atoms, and a precise knowledge of what that polarization was. This was primarily needed in order to facilitate a measurement of A_β that was performed on the same data that is the subject of discussion here. [22] While this is arguably less critical to a measurement of b_{Fierz} , it can still be an asset for eliminating systematic effects. We use only the polarized portion of the duty cycle in order to minimize other systematic errors, such as the scintillator energy calibration and overall trap position. It also makes for a more straightforward interpretation of the relationship of the measured values of A_β and b_{Fierz} when the systematic effects are the same for both measurements. Finally, using only polarized data allows us to make use of the ‘superratio’ construction in data analysis, a powerful tool for reducing (many) systematic errors at the expense of statistical precision (see Chapter 1.6). The Magneto-Optical Trap is a well-known technique from atomic physics, used to confine and cool neutral atoms [18], and it is also discussed in more detail in Chapter 2.

The TRINAT science chamber includes 6 ‘viewports’ specifically designed to be used for the trapping laser (see Fig. 2.7.).

A MOT also requires a quadrupolar magnetic field, which we generate with two current-carrying anti-Helmholtz coils located within the vacuum chamber itself. The coils themselves are hollow, and are cooled continuously by pumping temperature-controlled water through them.

One feature which makes our MOT unusual has been developed as a result of our need to rapidly cycle the MOT on and off – that is, it is an “AC-MOT”. Rather than running the trap with one particular magnetic field and one set of laser polarizations to match, we run a sinusoidal AC current in the magnetic field coils, and so the sign and magnitude of the magnetic field alternate smoothly between two extrema, and the trapping laser polarizations are rapidly swapped to remain in sync with the field [7][2]. See Figure 2.5.

We spin-polarize ^{37}K atoms within the trapping region by optical pumping [1]. A circularly polarized laser is tuned to match the relevant atomic resonances, and is directed through the trapping region along the vertical axis in both directions. When a photon is absorbed by an atom, the atom transitions to an excited state and its total angular momentum (electron spin + orbital + nuclear spin) along the vertical

axis is incremented by one unit. When the atom is de-excited a photon is emitted isotropically, so it follows that if there are available states of higher and lower angular momentum, the *average* change in the angular momentum projection is zero. If the atom is not yet spin-polarized, it can absorb and re-emit another photon, following a biased random walk towards complete polarization.

In order to optimally polarize a sample of atoms by this method, it is necessary to have precise control over the magnetic field. This is because absent other forces, a spin will undergo Larmor precession about the magnetic field lines. In particular, the magnetic field must be aligned along the polarization axis (otherwise the tendency will be to actually depolarize the atoms), and it must be uniform in magnitude over the region of interest (otherwise its divergencelessness will result in the field also having a non-uniform direction, which results in a spatially-dependent depolarization mechanism). Note that this type of magnetic field is not compatible with the MOT, which requires a linear magnetic field gradient in all directions (characteristic of a quadrupolar field shape), and has necessitated our use of the AC-MOT as described in (Sub-)Section 2.4.

2.5 Measurement Geometry and Detectors

MCPs. Hoops. Only one MCP works at a time! Blarg. Upon decay, atoms literally aren't trapped anymore by the trap. No trapping forces, no slowing forces, because it's all isotope-specific.

Back-to-back MCPs in an electric field to tag events from the trap, and to measure the trap position and polarization. Hoops to produce the electric field. The electric field sucks negatively charged electrons into one MCP, and positively charged ions into the other. See Fig. 2.6

Back-to-back beta detectors along the polarization axis.

Many laser ports to make the MOT functional, and for optical pumping. Fancy mirror geometry to combine optical pumping and trapping light along the vertical axis. Water-cooled (anti-)Helmholz coils within the chamber for the AC-MOT, fast switching to produce an optical pumping field.

Detectors are positioned about the second MOT for data collection. The detection chamber operates at ultra-high vacuum (UHV) and provides not only the apparatus

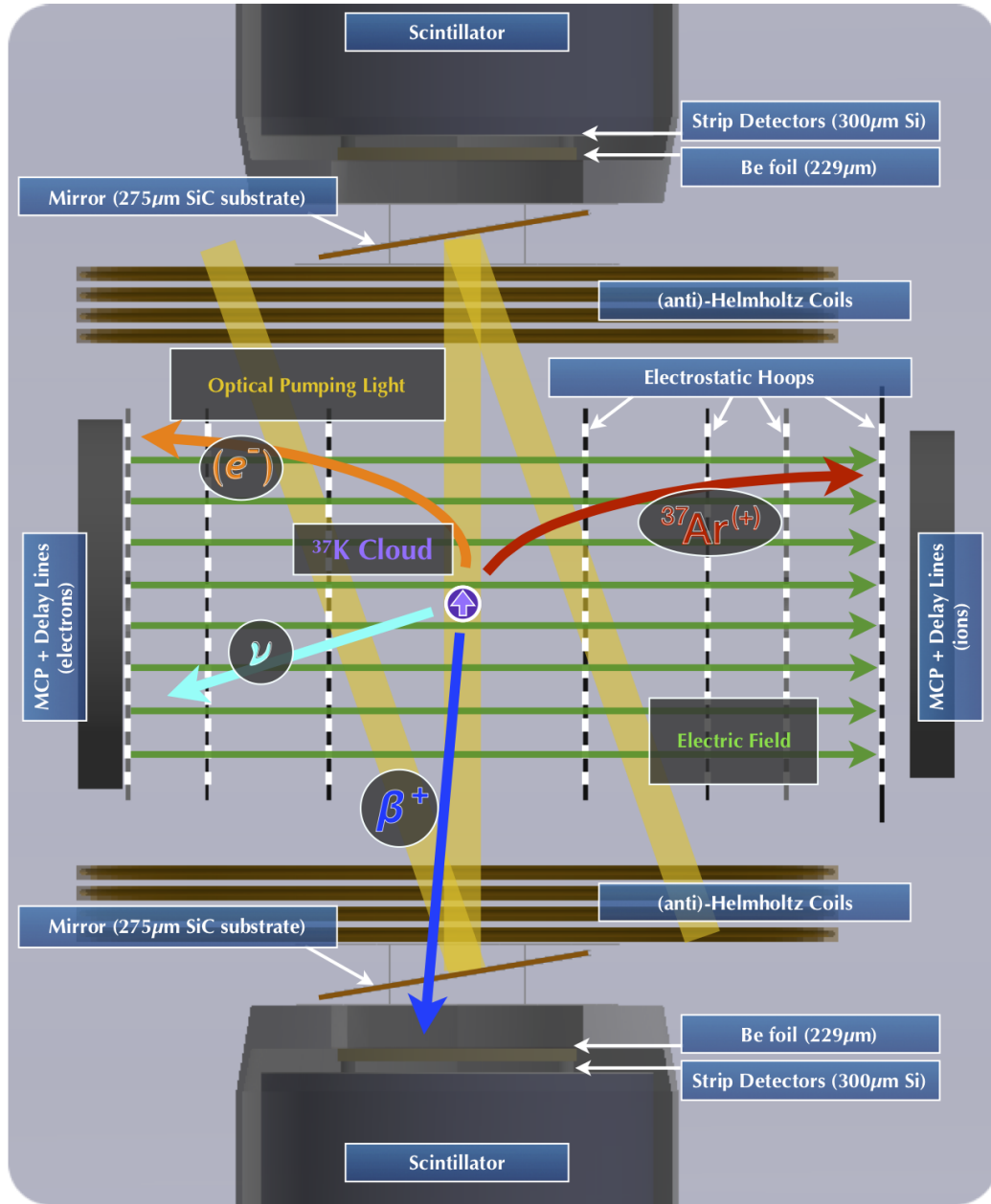


Figure 2.6: A decay event within the TRINAT science chamber. After a decay, the daughter will be unaffected by forces from the MOT. Positively charged recoils and negatively charged shake-off electrons are pulled towards detectors in opposite directions. Although the β^+ is charged, it is also highly relativistic and escapes the electric field with minimal perturbation.

necessary to intermittently confine and then spin-polarize atoms, but also the variety of detectors and implements required to quantify their position, temperature, and

polarization. The detection chamber further boasts an array of electrostatic hoops to collect both positively and negatively charged low energy particles into two microchannel plates (MCPs), and a further set of two beta detectors positioned along the polarization axis, each of which consists of a 40x40 pixel double-sided silicon strip detector (DSSD) and a scintillator and photomultiplier tube (PMT).

The beta detectors, located above and below the atom cloud along the axis of polarization (see Figure 2.6), are each the combination of a plastic scintillator and a set of silicon strip detectors. Using all of the available information, these detectors are able to reconstruct the energy of an incident beta, as well as its hit position, and provide a timestamp for the hit's arrival. Together the upper and lower beta detectors subtend approximately 1.4% of the total solid angle as measured with respect to the cloud position.

The two sets of beta detectors were positioned directly along the axis of polarization. Each beta detector consists of a plastic scintillator and photo-multiplier tube (PMT) placed directly behind a 40×40-pixel double-sided silicon strip detector (DSSD). The scintillator is used to measure the overall energy of the incoming particles, as well as to assign a timestamp to these events, while the DSSD is used both to localize the hit position to one (or in some cases, two) individual pixel(s), and also to discriminate between different types of incoming particles. In particular, though the scintillator will measure the energy of an incoming beta or an incoming gamma with similar efficiency, the beta will lose a portion of its kinetic energy as it passes through the DSSD into the scintillator. By contrast, an incident gamma will deposit only a very small amount of energy in the DSSD layer, making it possible to reject events with insufficient energy deposited in the DSSD as likely gamma ray events. Given that the decay of interest to us emits positrons, we expect a persistent background 511 keV gamma rays that are not of interest to us, so it is extremely important that we are able to clean these background events from our spectrum.

It must be noted that the path between the cloud of trapped atoms and either beta detector is blocked by two objects: a 275 μm silicon carbide mirror (necessary for both trapping and optical pumping), and a 229 μm beryllium foil (separating the UHV vacuum within the chamber from the outside world). In order to minimize beta scattering and energy attenuation, these objects have had their materials selected to use the lightest nuclei with the desired material properties, and have been manufactured to be as thin as possible without compromising the experiment. As the

$^{37}\text{K} \rightarrow ^{37}\text{Ar} + \beta^+ + \nu_e$ decay process releases $Q = 5.125$ MeV of kinetic energy [23], the great majority of betas are energetic enough to punch through both obstacles without significant energy loss before being collected by the beta detectors.

On opposing sides of the chamber, and perpendicular to the axis of polarization, two stacks of ~ 80 mm diameter microchannel plates (MCPs) have been placed (see Figure 2.7) as detectors, providing a time stamp when a particle is incident on their surfaces. Behind each stack of MCPs there is a set of delay lines, which provide position sensitivity for these detectors.

In order to make best use of these MCPs, we create an electric field in order to draw positively charged particles into one MCP, while drawing negatively charged electrons into the other MCP. Seven electrostatic hoops have been placed within the chamber (see Figure 2.7), and are connected to a series of high voltage power supplies. See Sections 2.6 and 6.4.2 for a discussion of what sort of charged particles we expect to observe in these detectors and how they are created.

Scientific data has been collected at field strengths of 66.7 V/cm, 150 V/cm, 395 V/cm, 415 V/cm, and 535 V/cm. It should be noted that these field strengths are too low to significantly perturb any but the least energetic of the (positively charged) betas from the decay process, and these low energy betas would already have been unable to reach the upper and lower beta detectors due to interactions with materials in the SiC mirror and Be foil vacuum seal.

2.6 The Photoionization Laser

In order to measure properties of the trapped ^{37}K cloud, a 10 kHz pulsed laser at 355 nm is directed towards the cloud. These photons have sufficient energy to photoionize neutral ^{37}K from its excited atomic state, which is populated by the trapping laser when the MOT is active, releasing 0.77 eV of kinetic energy, but do not interact with ground state ^{37}K atoms. The laser is of sufficiently low intensity that only $\sim 1\%$ of excited state atoms are photoionized, so the technique is only very minimally destructive.

Because an electric field has been applied within this region (see Section ??) the $^{37}\text{K}^+$ ions are immediately pulled into the detector on one side of the chamber, while the freed e^- is pulled towards the detector on the opposite side of the chamber.

Because $^{37}\text{K}^+$ is quite heavy relative to its initial energy, it can be treated as moving in a straight line directly to the detector, where its hit position on the microchannel plate is taken as a 2D projection of its position within the cloud. Similarly, given a sufficient understanding of the electric field, the time difference between the laser pulse and the microchannel plate hit allows for a calculation of the ion's initial position along the third axis.

With this procedure, it is possible to produce a precise map of the cloud's position and size, both of which are necessary for the precision measurements of angular correlation parameters that are of interest to us here. However, it also allows us to extract a third measurement: the cloud's polarization.

The key to the polarization measurement is that only atoms in the excited atomic state can be photoionized via the 355 nm laser. While the MOT runs, atoms are constantly being pushed around and excited by the trapping lasers, so this period of time provides a lot of information for characterizing the trap size and position. When the MOT is shut off, the atoms quickly return to their ground states and are no longer photoionized until the optical pumping laser is turned on. As described in Section ??, and in greater detail in [1], the optical pumping process involves repeatedly exciting atoms from their ground states until the atoms finally cannot absorb any further angular momentum and remain in their fully-polarized (ground) state until they are perturbed. Therefore, there is a sharp spike in excited-state atoms (and therefore photoions) when the optical pumping begins, and none if the cloud has been fully polarized. The number of photoion events that occur once the sample has been maximally polarized, in comparison with the size and shape of the initial spike of photoions, provides a very precise characterization of the cloud's final polarization [1].

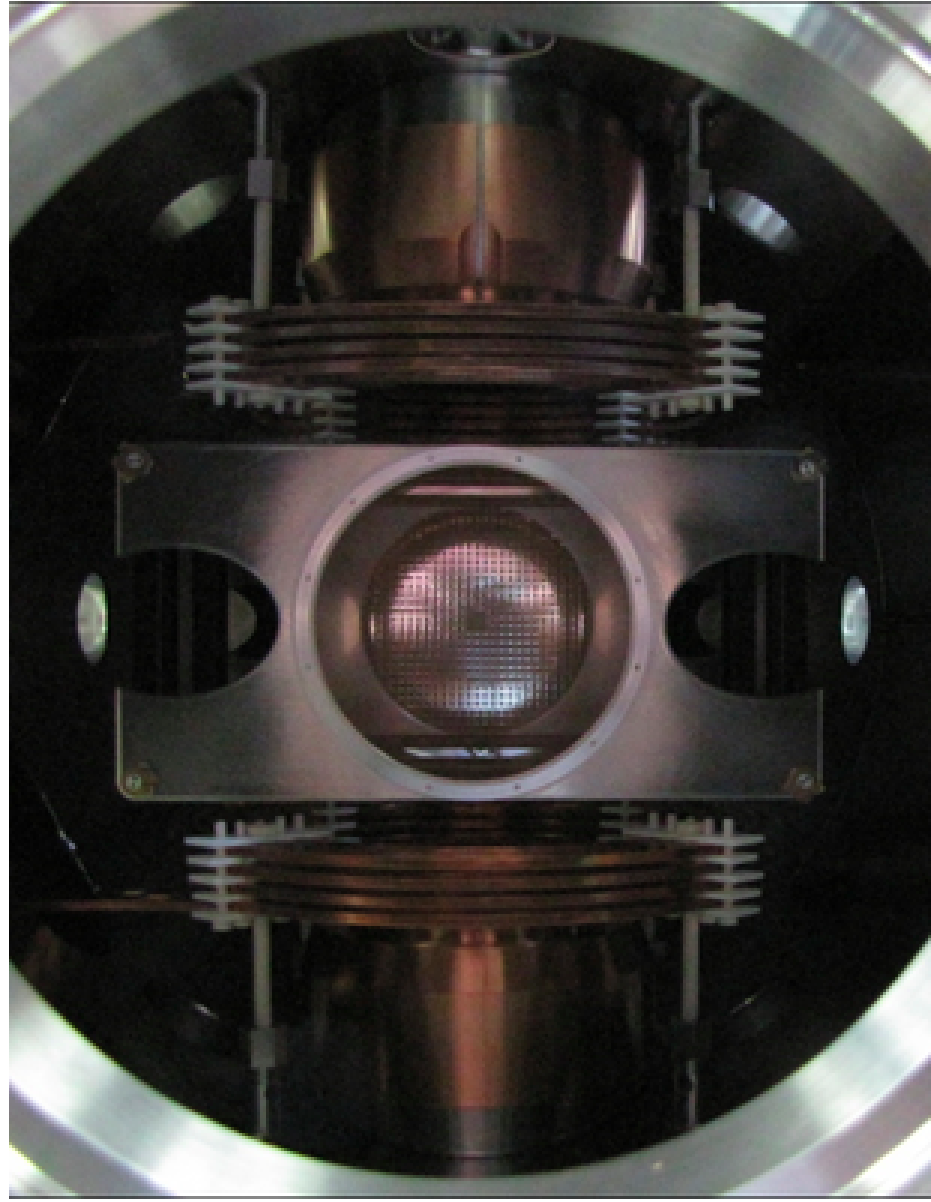


Figure 2.7: Inside the TRINAT science chamber. This photo is taken from the vantage point of one of the microchannel plates, looking into the chamber towards the second microchannel plate. The current-carrying copper Helmholtz coils and two beta telescopes are visible at the top and bottom. The metallic piece near the center is one of the electrostatic ‘hoops’ used to generate an electric field within the chamber. The hoop’s central circular hole allows access to the microchannel plate, and the two elongated holes on the sides allow the MOT’s trapping lasers to pass unimpeded at an angle of 45 degrees ‘out of the page’.

Chapter 3

Calibrations and Data Selection

I really need an excuse to include more pictures of data. Also, more pictures of simulations.

3.1 Measurements of the Atom Cloud

Anyway, here is a nice table describing the atom cloud, for each of 3 runsets, and I'll immediately reference it right now, as Table 3.1:

		Initial Position	Final Position	Initial Size	Final Size
Runset B	x	1.77 \pm 0.03	2.06 \pm 0.08	0.601 \pm 0.013	1.504 \pm 0.047
	y	-3.51 \pm 0.04	-3.33 \pm 0.05	1.009 \pm 0.013	1.551 \pm 0.018
	z	-0.661 \pm 0.005	-0.551 \pm 0.021	0.891 \pm 0.004	1.707 \pm 0.015
Runset C	x	2.22 \pm 0.05	2.33 \pm 0.11	1.18 \pm 0.04	1.538 \pm 0.087
	y	-3.68 \pm 0.04	-3.31 \pm 0.06	0.965 \pm 0.012	1.460 \pm 0.030
	z	-0.437 \pm 0.09	-0.346 \pm 0.037	0.927 \pm 0.007	1.797 \pm 0.026
Runset D	x	2.274 \pm 0.012	2.46 \pm 0.06	0.386 \pm 0.016	1.382 \pm 0.046
	y	-4.54 \pm 0.04	-4.28 \pm 0.04	0.986 \pm 0.08	1.502 \pm 0.013
	z	-0.587 \pm 0.04	-0.481 \pm 0.018	0.969 \pm 0.003	1.861 \pm 0.013

Table 3.1: Cloud Positions and Sizes – Measured immediately before and immediately following the optical pumping phase of the trapping cycle. All entries are expressed in units of mm, and the “size” parameters describe the gaussian width.

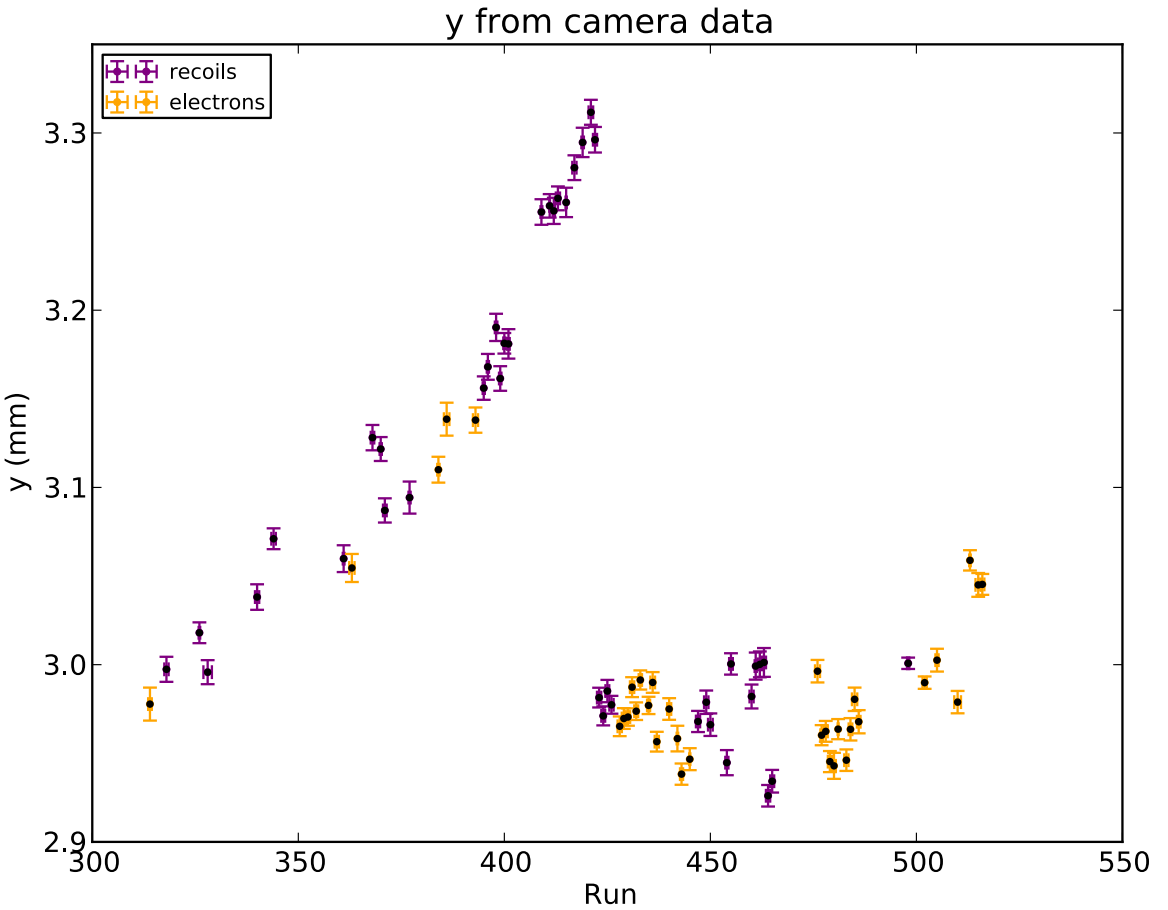


Figure 3.1: Trap Position along the “Time-of-Flight” Axis. Electron runs and recoil runs plotted by run number. (I should probably re-plot this. Maybe combine info with Fig. (3.2).)

3.1.1 Measurements with the rMCP

I did this, and they’re absolutely needed to make any sense of the trap position data. These calibrations are done during AC-MOT time, and we’re actually interested in the rMCP data taken during OP time. Can I find pictures to estimate the size of the change resulting from the magnetic field? In any case, the change is pretty small.

Now, the unsorted bullet points for the rMCP stuff!

Using the “other” data set with the rMCP: Measure the trap position/size/velocity/expansion with the rMCP and with the camera. Necessitates calibrating the rMCP, which is its own whole thing. Also measure polarization.

- rMCP calibration probably gets its own section, if not its own chapter..

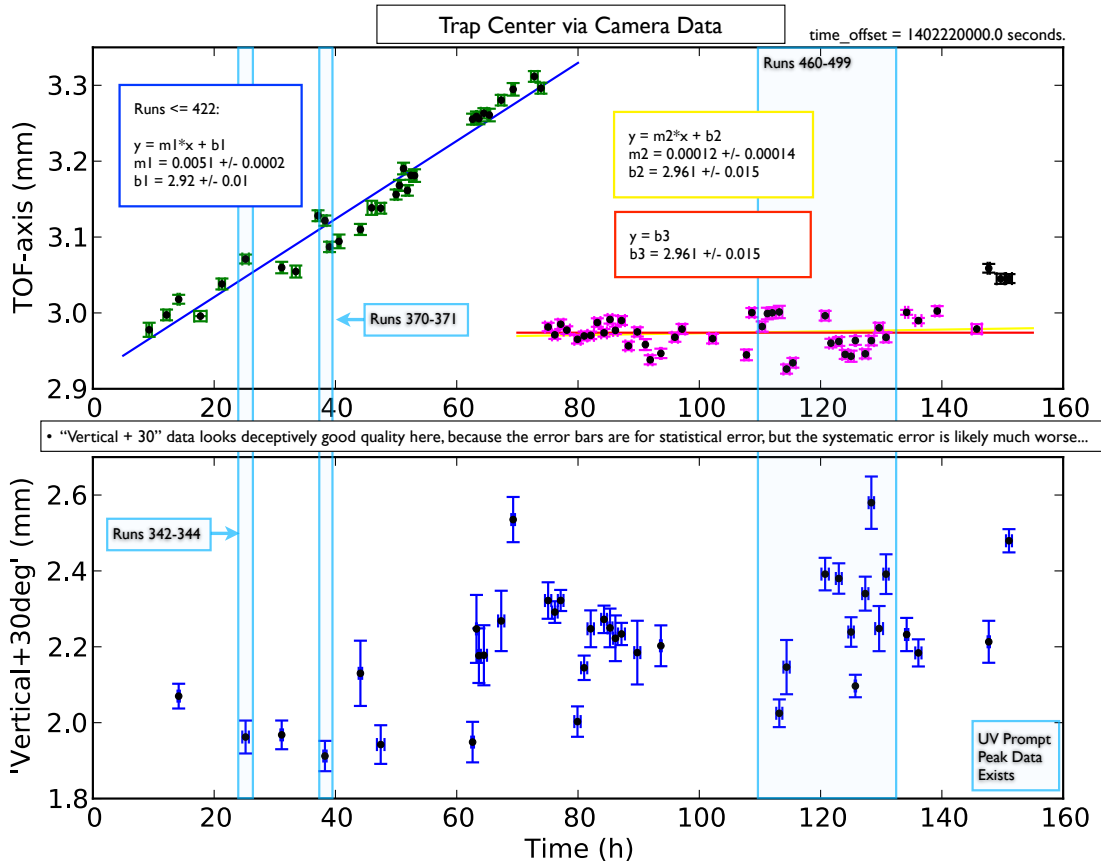


Figure 3.2: Trap Position along the “Time-of-Flight” Axis and the “Vertical+30” Axis. All runs plotted by time of run. ([Need to re-plot this.](#))

- We took the mask off before the 2014 run, to give us more detector area. Use previous reference calibration *with the mask* during the test run in Nov 2013. The delay line’s non-linearities should be the same, assuming we can get the centering the same. Cables have changed and stuff, so we have to re-center the pre-calibration image to where the old pre-calibration image was. ... So, center the new runs w.r.t the old run.
- We’ll want to make some sum cuts for these things. We might like them to be identical, or at least identical-ish, but the peaks don’t really look the same. So we’ll settle for “decent sum cuts for all!”. ... So, apply sum cuts to the new runs and old run.
- Calibrate the old run, with the mask. In fact, I don’t remember which order I

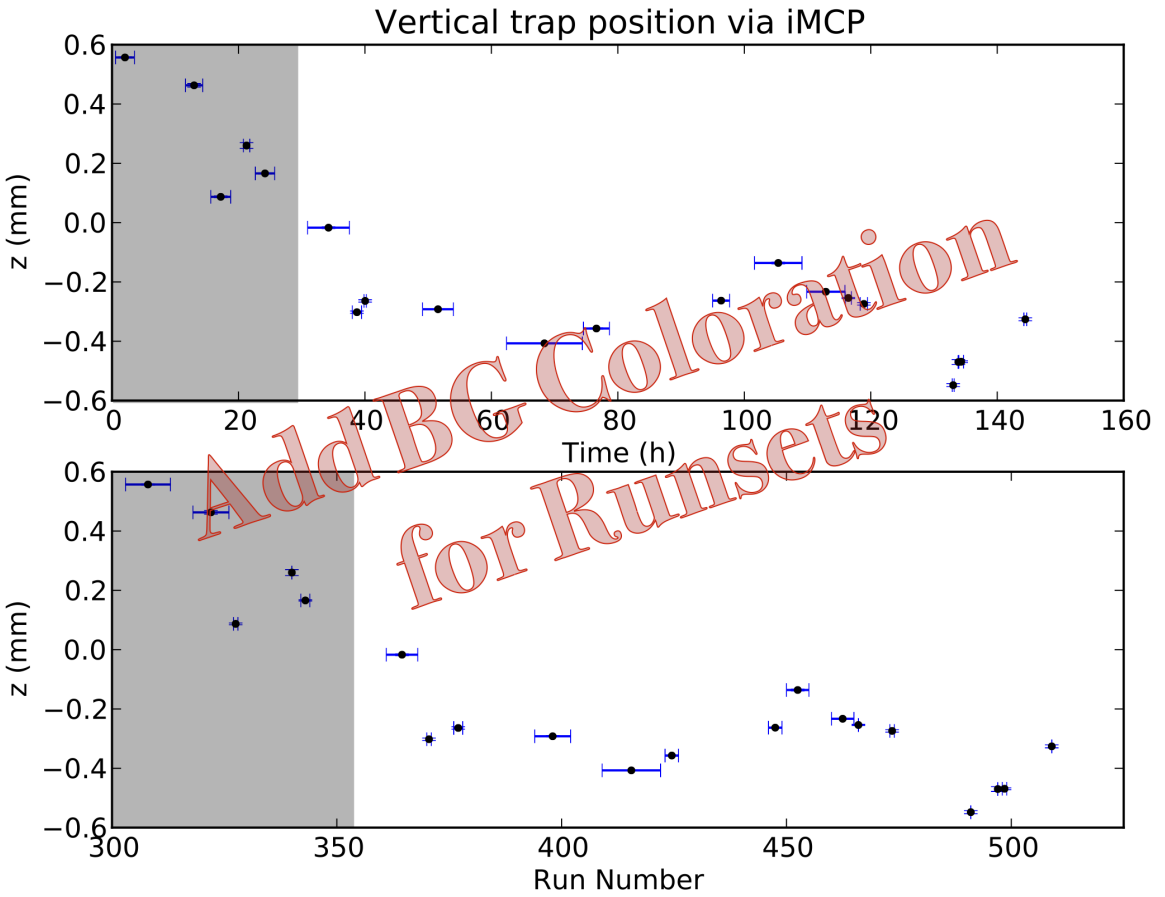


Figure 3.3: Trap Position along the Vertical Axis, plotted as a function of time of run (top) and run number (bottom).

did things in. But I have a record of it here, somewhere...

3.1.2 Measurements with the eMCP

I can describe the eMCP calibration here, even though it mostly wasn't implemented by me. It is tangentially relevant to data selection and background estimation by providing an experimental energy spectrum for shake-off electrons. It's actually a pretty neat algorithm that I basically wasn't involved with.

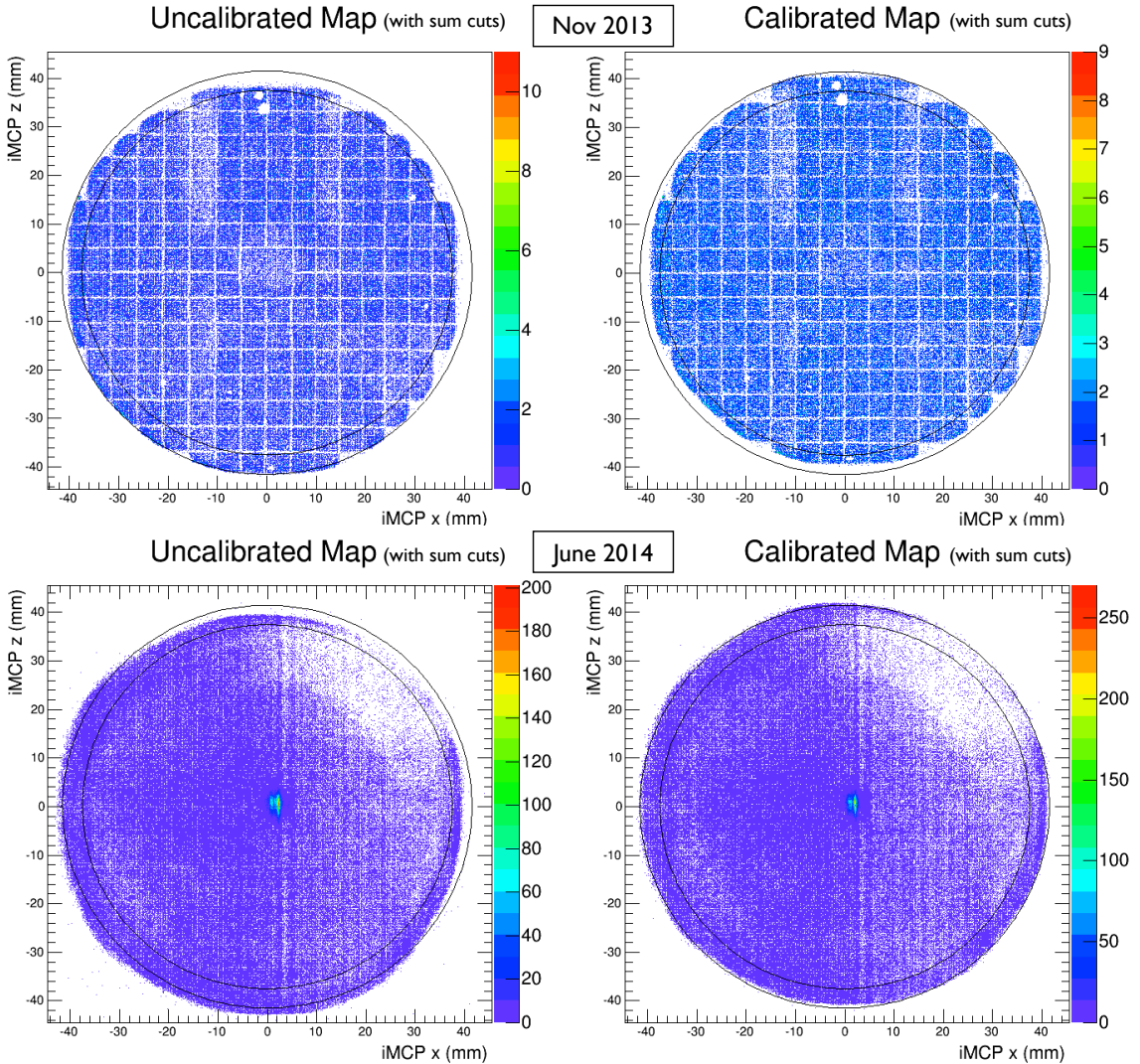


Figure 3.4: rMCP Calibration. Definitely comment about how this calibration went here, in the figure caption. (Do I definitely want a picture with the stupid line-y runs? Maybe it's better to just *not*...)

3.2 Data Selection and Preliminary Cuts

Although the detection chamber was designed to feature two MCP detectors on opposing sides of an applied electric field intended for simultaneous use (see Section 2.5), in practice the two detectors produced quite a bit of feedback when operated at the same time. In order to salvage usable data from the beamtime, we ended up running only one detector at a time, but switched which detector was in use every few hours,

collecting approximately the same amount of data with each detector. Thus, the runs are sorted into ‘electron’ and ‘recoil’ runs, depending on what the detector in use was intended to detect.

While the beta asymmetry and Fierz interference are best evaluated using the electron runs, the recoil runs are best for evaluating the polarization (a dominant uncertainty in the beta asymmetry measurement) and the cloud position. The polarization measurement is the subject of a recent publication (see [1]), and the cloud position evaluation is discussed in more detail in Chapter 3.

The data is further split up into four runsets: A, B, C, and D based on when certain detection settings were adjusted, and each of these runsets contains both electron and recoil runs. These four runsets were then treated separately for nearly all parts of the analysis. In particular, Data Set A was neglected completely during analysis after it was determined that one scintillator had an improperly set hardware threshold such that lower energy betas weren’t being detected at all. Additionally, there was a QDC module failure between Runsets B and C, resulting in an abrupt change in calibration for the two scintillators.

	Electron Runs	Recoil Runs	OP Delay
Runset A	314, 362, 363, 383, 384, 385, 386, 393, 420.	303, 308-313, 318, 326, 327, 328, 340, 342, 343, 376, 377, 378, 394, 395, 396, 398-402, 409-419.	$300\ \mu s$
Runset B	428-437, 440-445.	421-426, 446, 447, 449.	$300\ \mu s$
Runset C	476, 477.	450, 454, 455, 460-466, 473, 474.	$700\ \mu s$
Runset D	478-489, 502, 503, 504, 505, 510, 513.	491, 497, 498, 499, 509.	$400\ \mu s$

Table 3.2: A list of 2014 online runs with potentially usable data. Runset A was discarded completely due to problems with hardware threshold settings. There was a QDC module failure before Run 450, so it and all subsequent runs were performed using a different module, and as a result the scintillator calibrations changed slightly at this time. Anyway, the point of this thing is to show which electron runs and recoil runs go together, for the purposes of evaluating polarization and cloud attributes.

Before proceeding further, several basic cuts are performed on the data. For the Electron Runs which are to be processed directly into a physical measurement, we

	OP Delay	Electric Field	Usable Events
Runset A	300 μ s	66.67 V/cm	0
Runset B	300 μ s	150.0 V/cm	173,640
Runset C	700 μ s	150.0 V/cm	18,129
Runset D	400 μ s	150.0 V/cm	207,596

Table 3.3: Electron Runs and Parameters.

consider only events in which there was a recorded hit *both* on the eMCP *and* on (at least) one of the scintillators. The required scintillator hit, of course, is potentially a beta, and so it is obvious why this must be present. The eMCP hit requirement – particularly with the timing of the eMCP hit occurring within a certain time range relative to the scintillator hit – is used to tag beta decay events originating from the cloud, as opposed to those originating from some other surface within the chamber. The precise time interval to be used, and how its results should be evaluated, is discussed in Section 3.4, but for the first pass through the data it is good enough to simply require that an eMCP hit occurred. Although not every beta decay event from the cloud will produce a hit on the eMCP, this requirement eliminates a great deal of background that would otherwise be challenging to evaluate.

Because the eMCP hit is required as a ‘tag’ of good events, it is also necessary to remove from direct consideration any event which is coincident with a pulse of the photoionization laser. When photoionization occurs within the atom cloud, an orbital electron is removed from the atom and will be accelerated by the electric field into the eMCP, just as a shake-off electron from a decay might be. If, by chance, this photoelectron arrives in coincidence with a scintillator hit, it would be interpreted as a decay event from the trap – unless we preemptively discard it.

Over the course of the runtime, there were several instances where we noted an apparent electrical discharge within the experimental chamber, producing enormous backgrounds for a short time. The detectors typically recovered quickly afterward, so it was neither necessary nor useful to stop an entire run to wait for the system to recover. Instead, the time when the discharge occurred was recorded, and events within approximately one minute of the spark time were discarded.

We use only the “fully polarized” events for which we have a detailed understanding of the nuclear polarization (described in more detail in [1]). This means we must

use *only* events from the “optical pumping” portion of the duty cycle (see Fig. 2.4), and discard events when the DC- or AC-MOT is active. After the AC-MOT is shut off, there is a short delay before optical pumping begins (see Table 3.2) to allow the magnetic field to decay, and it is only after $100\ \mu s$ of optical pumping that we consider the atoms to be fully polarized. Furthermore, because the magnetic field from the DC-MOT is slow to decay (relative to the field from the AC-MOT), all events from the first five AC/OP cycles after every atom transfer are discarded. A secondary benefit of our insistence on considering only polarized data is that the scintillators’ gains are more stable in the presence of only the (small, stable) magnetic field used for optical pumping than they are in the presence of a larger oscillating magnetic field used for trapping.

Finally, because this analysis depends heavily on energy measurements from the two scintillators as a proxy for beta energy, it is necessary to remove events in which the pulser LED fired. Although the pulser LED is useful for evaluating the stability of the scintillators, in the case where an LED pulse occurs together with a true beta hit in the scintillator, it may change the measured energy. Therefore, we discard all events that include an LED pulse.

3.3 Further Cuts Using the DSSD

Although it was not possible to use the DSSD in real-time analysis or event triggering, the DSSDs may be used, after the data has been collected, to distinguish between different types of particles incident on the detector, as more energy will be deposited by heavier particles. When a scintillator hit is triggered by a particle originating within the experimental chamber, that particle will typically have passed through the DSSD before arriving at the scintillator.

In the present experiment, the two primary particles that will concern us are β^+ particles originating from the decay of ^{37}K , and γ rays, which may be produced through a variety of processes, e.g. directly from the 2% decay branch, through annihilation of β^+ particles upon their interaction with regular-matter electrons, or bremsstrahlung radiation from emitted β s.

We would like to look specifically at events involving β^+ particles arriving direct from a decay within the atom cloud, and the DSSD may be used to eliminate events

in which the scintillator is triggered by a γ . An incident β will typically deposit some portion of its energy in the DSSD as it passes through, however an incident γ will deposit significantly less energy; for this setup the energy deposited by a γ is generally indistinguishable from background on the DSSDs. Therefore, we require that a ‘good’ event must include a ‘good’ hit to the DSSD as well as a hit to the associated scintillator.

In order to proceed at this point, and because the DSSD readout records so much information, it is necessary to develop some criteria to determine whether or not we will accept any given DSSD readout as a β hit.

We read out the full waveform for every strip at each event with a scintillator hit, but in post-processing take *only* the ‘time’ and ‘energy’ from the peak waveform height and the time in the waveform at which that occurs. Each strip will have its own noise spectrum and energy calibration. To classify an event as a good DSSD hit, we require at least one ‘x’ strip and one ‘y’ strip record an energy above the noise threshold. We require that the x strip and the y strip agree (to within some number of standard deviations) in amount of energy deposited, and in the time at which that hit occurred. In order to avoid problems resulting from the strips’ non-uniform noise thresholds, we further require that the energy deposited be greater than some lower-end cutoff which is selected so as to be higher than every individual strip’s noise threshold. In this case, the DSSD’s lower energy uniform threshold was set at 50 keV.

We also elect to use only events where a beta hit the DSSD within a 15.5 mm radius of the center of the detector, so as to avoid scattering effects from the collimator walls.

3.4 Further Cuts Using the eMCP

The eMCP features a set of three delay lines, intended to be used to record the position of a hit, as in Fig. 3.5. Though only two delay lines is sufficient to determine the position within the plane of the MCP if they are both hit, the presence of a third delay line allows for some redundancy. In practice, however, a large fraction of otherwise ‘good’ events include a hit on the eMCP, but have insufficient information recorded on the delay line channels to reconstruct a position.

Because a SOE from the trap is most likely to land in the centre of the plate, while the background from other sources is roughly constant across the plate, it might make

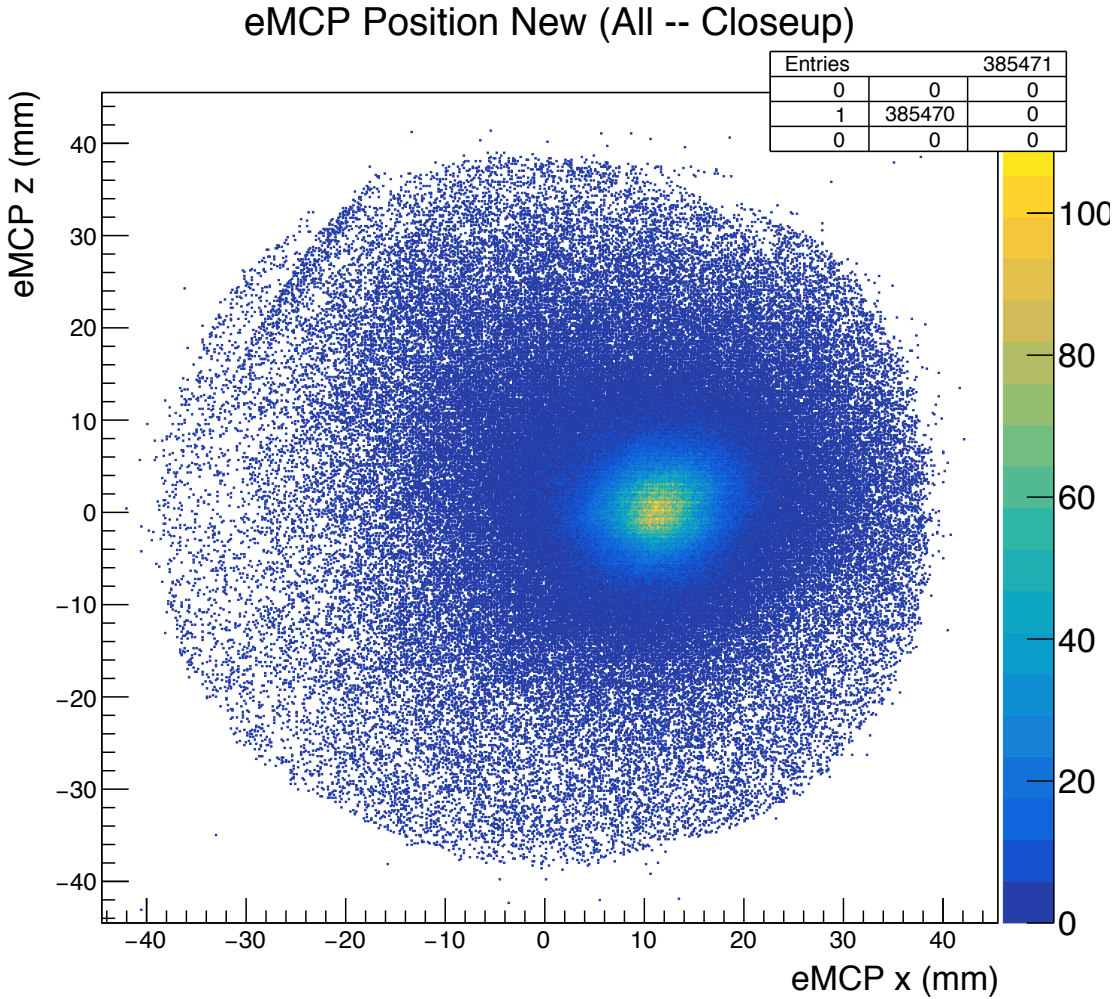


Figure 3.5: Position as measured on the eMCP, after some data cleaning.

sense to accept only events where the eMCP hit is within some radius of the central peak. This methodology was seriously considered because the remaining data has a much lower fraction of background events polluting it – however this results in a loss of around half of the events even for the most generous eMCP radius cuts (see Fig. 3.6). Therefore, it was decided that no position cuts on the eMCP would be made in the final analysis.

Several years after the data was initially collected, a problem was discovered with our low-level analyzer software, which we had been using to convert large and unwieldy MIDAS data sets into somewhat smaller and more manageable ROOT data sets. In particular, for every timestamp recorded, our raw MIDAS data actually included both

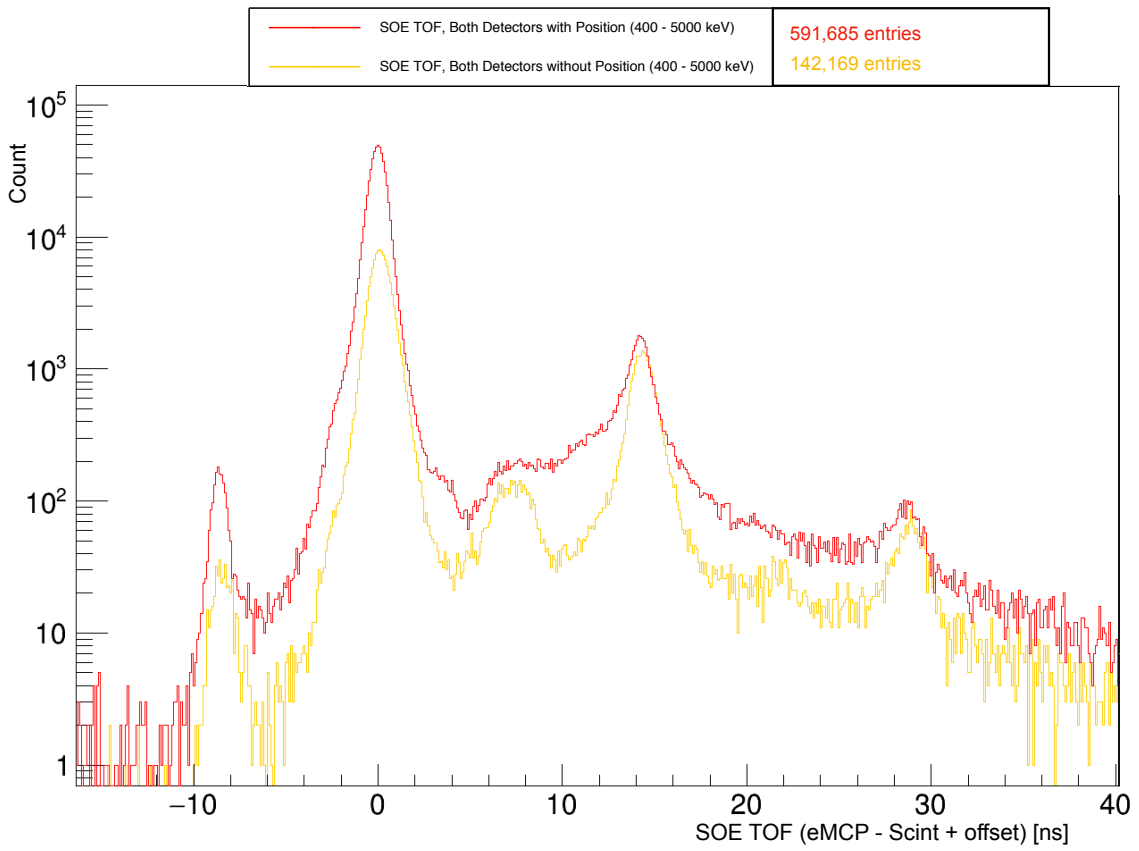


Figure 3.6: Beta-electron TOF, for events with and without eMCP hit position information. A cut will eventually be taken to accept only events sufficiently near the largest peak – in this case the number of events is ‘only’ decreased by a factor of 2.

a timestamp for the leading edge (LE) of the pulse, and a timestamp for the trailing edge (TE). The analyzer had—for years—been reporting the timestamp associated with the trailing edge of the pulse. Initially it was unclear if there might have been a reason behind this choice, but a closer examination of the data showed that the LE data included less timing jitter and noise, as well as a sharper peak for timing pulses across the board (as in Fig. 3.7), with some channels showing a larger effect than others. This was corrected, and the entirety of this analysis has been performed now using the cleaner LE spectra.

The place where this change between the TE and LE timestamps had the biggest impact on the analysis is in the shake-off electron time-of-flight spectra, on which a cut must eventually be taken. Although this problem was not discovered in time

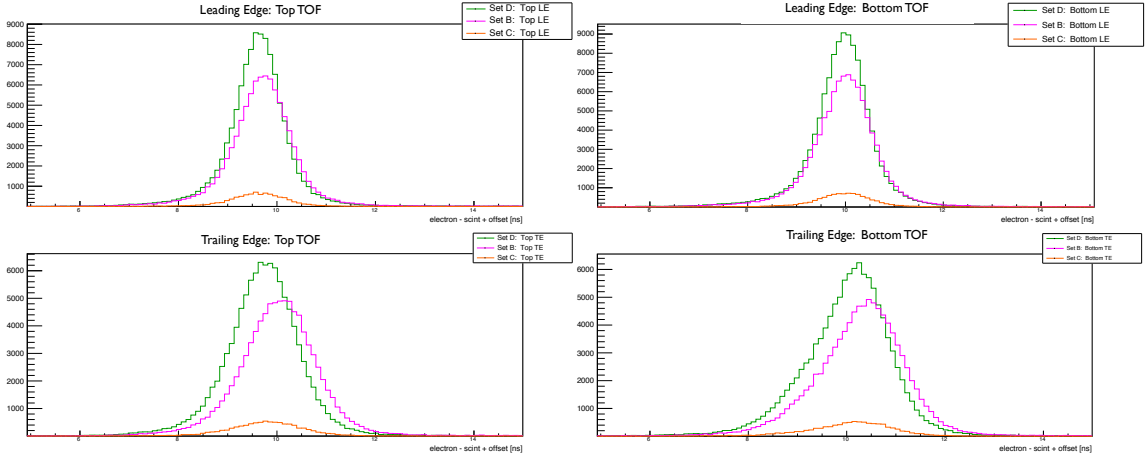


Figure 3.7: SOE TOF peaks (eMPC - Scintillator), using the leading edge (LE) and using the trailing edge (TE). Data is sorted according to runset. For each individual runset, the TE peak is broader than the LE peak. The centroid of each runset is also more variable in the TE plots.

to be used in the previous measurement of A_β using this same data [22], it likely would have had a negligible effect on the final result, because the SOE TOF cut that was used there was comparatively loose, and the evaluation of the background that remained was not a dominant systematic effect.

With the data reprocessed using the leading edge for timestamps, I wanted to eliminate as much background as possible from the SOE TOF spectrum. With this goal in mind, the next step was to correct the scintillator timing for its low energy ‘walk’ (see Fig. 3.8). A quartic polynomial was fit to each of the 2D timing vs energy spectra (the top and bottom detectors were treated separately), and the result was used to produce a ‘straightened’ SOE TOF spectrum with respect to measured scintillator energy, and as expected, the resulting SOE TOF spectrum was a bit more sharply peaked.

With the SOE TOF spectra cleaned up, a cut can be taken to reduce the fraction of background events. Informed by the model of background spectra described in Section 4.3, a was made to include only a 2.344 ns window around the primary peak in further analysis . (see Fig. 3.9).

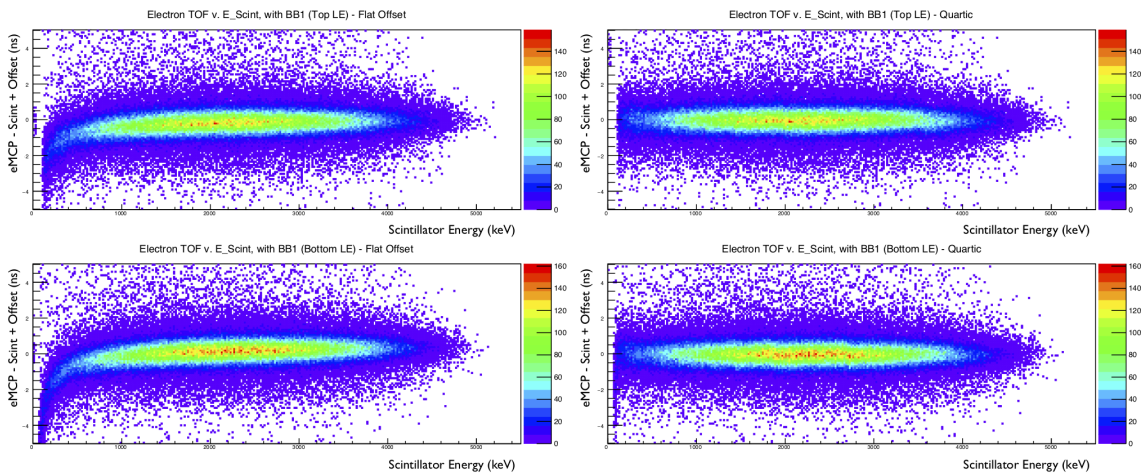


Figure 3.8: SOE TOF walk, before (left) and after (right) applying a quartic adjustment to straighten out the effective TOF.

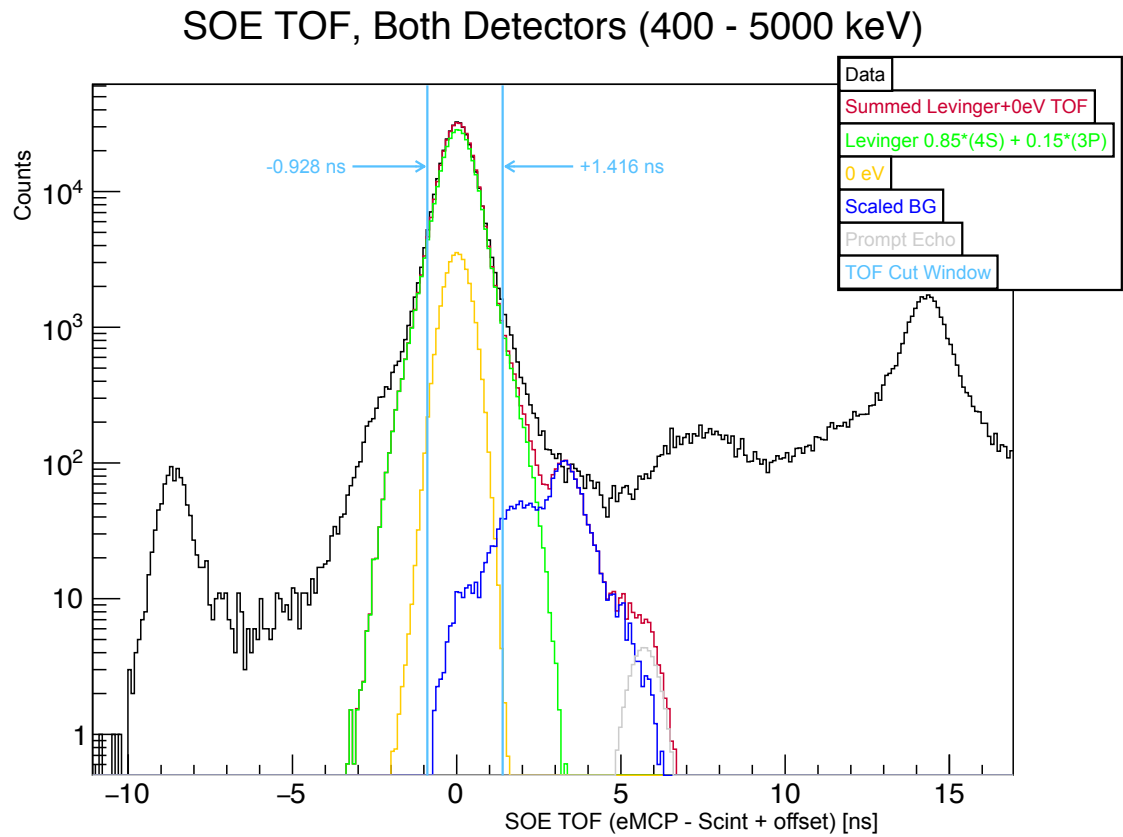


Figure 3.9: SOE TOF, model and data. In the end, I cut the data to use only events with a TOF between -0.928 ns and +1.416 ns. Max. possible background is like a factor of two too big. Similar quality results no matter how you distribute the Levinger spectra between 4S and 3P, however adding the 0 eV electrons makes a big improvement to the agreement.

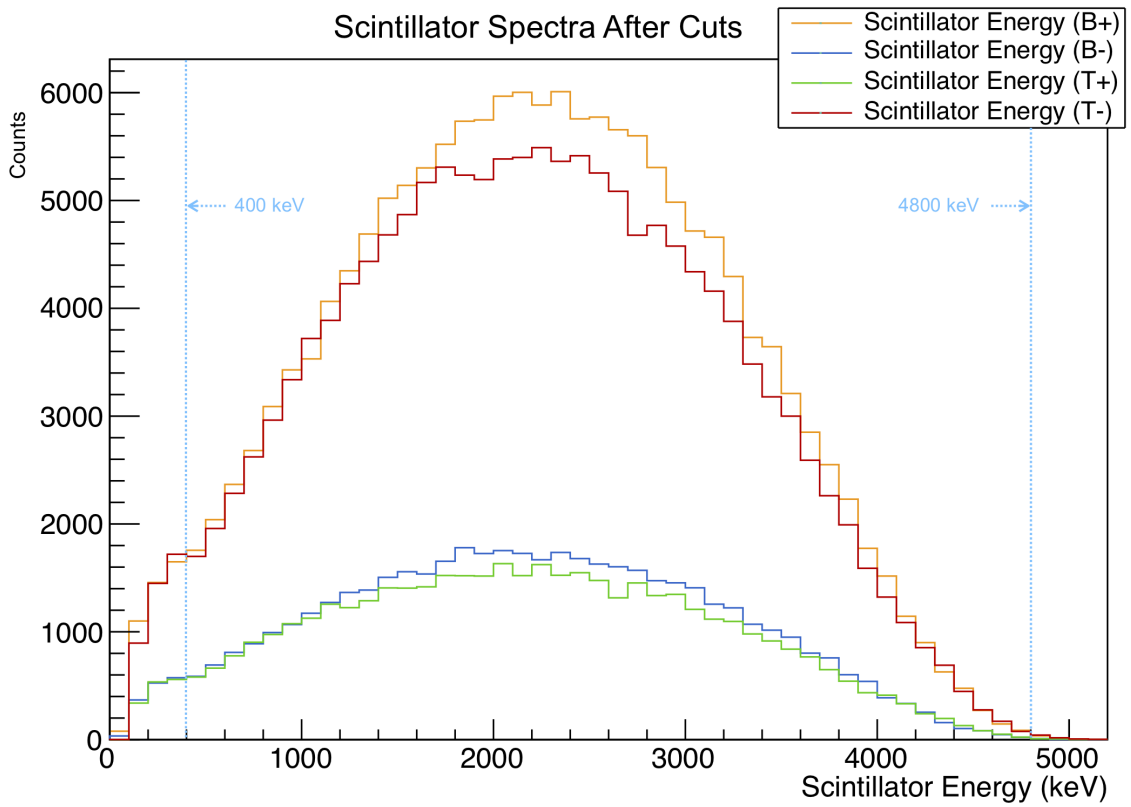


Figure 3.10: Experimental Scintillator Spectra, for both detectors in both polarization states. These spectra are what remain after all cuts have been taken. All runsets are included.

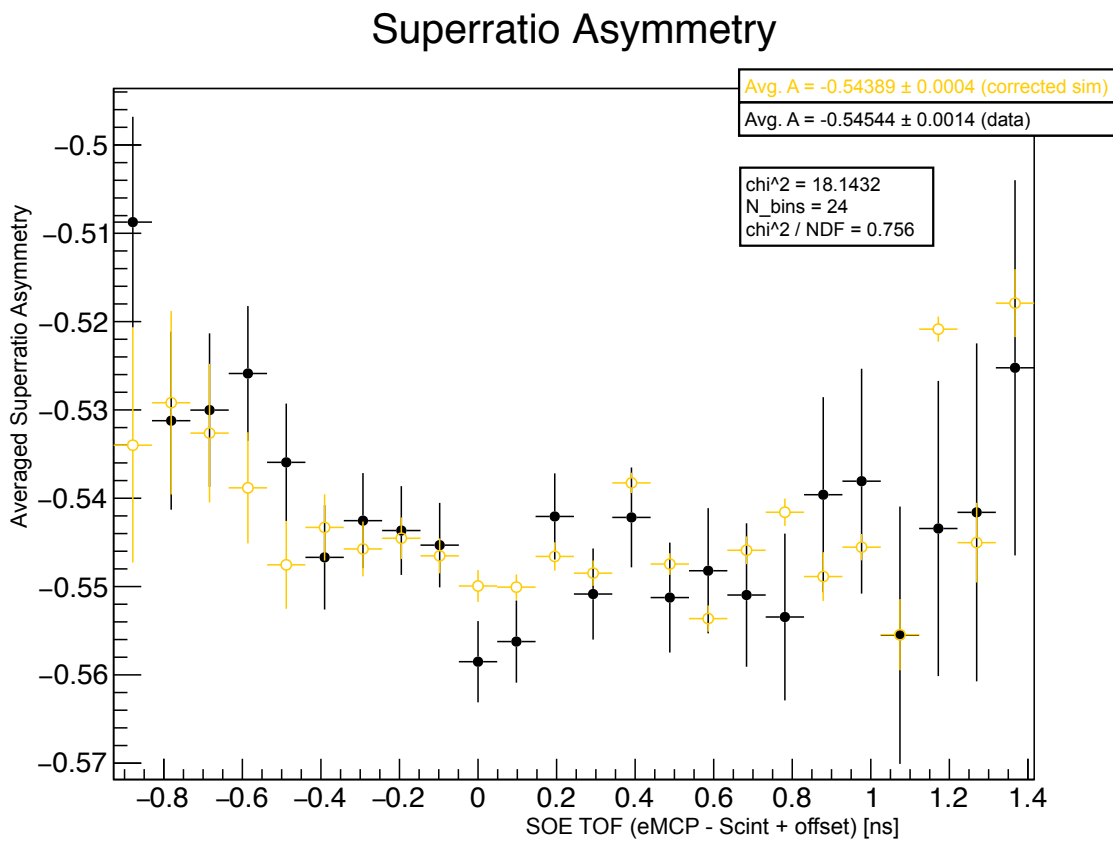


Figure 3.11: The superratio asymmetry, averaged over all scintillator energies between 400-4800 keV, is used to compare the experimental data and simulated TOF model as a proxy for the quality of the model to estimate the background. All other cuts have been applied.

Chapter 4

Simulations

I really need an excuse to include more pictures of data. Also, more pictures of simulations.

The TRINAT collaboration has created a Geant4 (G4) simulation which models the geometry and materials within the experimental chamber, and uses a monte carlo algorithm to describe generalized physical processes such as particle scattering and energy loss, within the geometry specific to the experiment. This software library has been maintained and updated over several generations of graduate students.

4.1 Considerations for Software Upgrade Implementation

Prior to the simulations required for this particular experiment, two different sets of changes to the G4 code were needed – the first to enable multithreading, and the second to introduce certain BSM interactions to the decay distribution.

Enabling multithreading allows for a single instance of the Geant4 simulation to run on several processors at once, effectively speeding up the overall simulation by a factor of the number of processors used. In the years since the simulation was originally created, the Geant4 collaboration had created libraries intended specifically to support multithread usage, and since the running G4 simulations had historically been very time consuming for the TRINAT collaboration, the decision was made to implement multithreading within our own monte carlo software, on the hopes that this would enable faster progress in analysis.

Enabling multithreading support turned out to be quite time consuming, and in the end it might have been faster to have spent those months running simulations one processor at a time. Perhaps the improvement will prove valuable for use in future TRINAT experiments.

The TRINAT G4 monte carlo package had never been used to directly model interactions beyond the standard model within the decay physics. It had previously been set up by the collaboration to use a probability density function (PDF) including most of the terms from Holstein's Eq. (51) [17], which describes both electron and neutrino momenta from polarized beta decay. This treatment is quite robust, and includes corrections at recoil-order, as well as certain other corrections of similar size.

Unfortunately, terms arising from interactions beyond the standard model are not included in Holstein's description of the decay process. To understand the kinematic results of the exotic interactions of interest to us here, we turn to the classic JTW treatment of beta decay [5] [16]. In addition to the (expected) vector and axial interactions, JTW also describes the interaction in terms of (exotic) scalar and tensor interactions, should such be present. Despite JTW's broad ability to describe beta decay under a variety of physical models, this treatment includes only the leading-order terms, and smaller terms, such as recoil-order corrections, are neglected entirely.

Because the present project is a precision measurement of the Fierz interference, a term which arises from scalar and tensor couplings, it was imperative to create an event generator for our G4 simulations that could account for these exotic interactions while also including in its PDF the higher-order effects which, in some cases, can mimic the effects of a scalar or tensor current.

While it might have been possible to directly combine JTW's result with Holstein's Eq. (51), it should be noted that JTW's expression is not compatible in general with the principle of conservation of momentum; as recoil momentum is neglected entirely, the description is only of two leptons emerging from a nucleus in directions that do not directly oppose one another. Therefore, the prospect of combining these two slightly incompatible expressions directly might be enough to give one pause. On an experimental level, the mathematical description of an emerging neutrino is only of interest to us to the extent we can reconstruct it based on detecting both a beta and the recoiling nucleus from a single decay event, and within the present experiment we do not have simultaneous access to both a beta detector and a recoil detector.

In light of the above considerations, it was decided that an entirely new event

generator must be created, based instead on Holstein’s Eq. (52), in which neutrino momentum has been integrated over and is therefore no longer an explicit part of the PDF [17]. As one might guess, Holstein’s Eq. (52) is greatly simplified in comparison to Holstein’s Eq. (51). A similar integration over all possible neutrino momenta can also be performed on the JTW PDF, causing several terms to vanish. The result in both the Holstein and JTW cases is a PDF over only beta energy and direction as measured with respect to nuclear polarization, and the two expressions can be combined in a straightforward manner by comparing similar terms.

It is this combined Holstein+JTW expression that forms the basis of the new G4 event generator. It must be noted that although the largest effect from any present scalar or tensor interactions would likely (depending on certain phase angles) be in a non-zero value of b_{Fierz} , these interactions can also introduce a perturbation to A_β at a higher order. In order for any precision experimental measurement of b_{Fierz} to be generalized to limits on the parameter space of scalar and tensor currents, it is important to incorporate an accurate representation of the results of such exotic interactions on *all* available observables, and the new G4 event generator does this.

4.2 The Simple Monte Carlo and Response Function

Because of the large number of systematic effects to be examined, and because of the processor time required to run a high statistics Geant4 simulation even after enabling multithreading support, it was desirable to develop a procedure by which it would be possible to evaluate certain systematic effects while avoiding the computationally intensive simulations that might traditionally be used. To this end, a fast-running Simple Monte Carlo (SMC) was developed together with an empirical “response function” similar to the one described by Clifford et al [10] to describe probabilistic beta energy loss before its detection in a scintillator. In the end, the lineshape description became quite involved, and it is unclear whether, in the end, any time was saved this way.

The purpose of the SMC was to *quickly* generate initial particle kinematics probabilistically for beta decay events, and it uses the very same event generator based on Holstein’s Eq. (52) [17] that was developed for use with the more sophisticated Geant4 simulations. However, unlike in a G4 simulation, the SMC makes no attempt

to track particles through the chamber, and instead simply calculates detector hits based on initial particle momentum. This procedure obviously neglects scattering effects, which can (in differing regimes) both *increase* and *decrease* the number of beta particles incident on a detector. Furthermore, this procedure also neglects any energy absorption in materials through which the beta passes before hitting a scintillator – and the beta *must* pass through several such materials (see Fig. 2.6).

To make the best use of the SMC for evaluating systematic errors, the energy lost before a beta hits a scintillator must be accounted for somehow in order to ensure all relevant physical effects are propagated through. In particular, before hitting a scintillator, a beta must pass through a $275\,\mu\text{m}$ thick silicon carbide mirror, a $229\,\mu\text{m}$ thick beryllium foil, and finally a set of $300\,\mu\text{m}$ thick double-sided silicon strip detectors (DSSDs), before finally having its remaining energy absorbed within a scintillator. Although the DSSDs are themselves detectors with the ability to record the amount of energy deposited by an incident particle, there are some known problems in achieving a uniform level of precision across the full surface of the DSSDs, so adding the DSSD energy back to the scintillator energy to produce a better estimate of the original beta energy has the potential to create some problems for the analysis. Furthermore, given the presence of the mirror, an object with a similar thickness and scattering properties to the DSSDs, re-adding the energy lost in the DSSDs would not eliminate the need to estimate probabilistic energy loss in similar materials.

In order to create a quantitative description of the effective response function, which varies with initial beta energy, we have created an analytic function of 14 parameters for each of four detector and polarization combinations (56 parameters in total), to represent the final beta energy spectra in the scintillators. The values of these parameters must be determined empirically, by a fit to simulated spectra. Since the final response function is expected to be a function of initial beta energy, we must allow for these parameters to also vary as a function of initial beta energy. To effect this result, the TRINAT Geant4 simulation is used to generate a series of ‘mono-energetic’ spectra. That is, for each energy value under consideration (selected to span the energy range of betas in our decay), events are generated in which every outgoing beta initially has the same amount of kinetic energy, and the angular distribution of these betas is physically appropriate for the polarization and beta energy under consideration. Both polarization states must be considered separately. These mono-energetic betas are propagated through the experimental geometry via Geant4, and

the resulting scintillator spectra are recorded. Cuts identical to those imposed on the experimental data are implemented (see Chapter 3). Several such spectra are shown for the Bottom Detector in the ‘-’ polarization state, with their best fits and the residuals thereof in Figs. 4.1, 4.2, 4.3, 4.4, and 4.5.

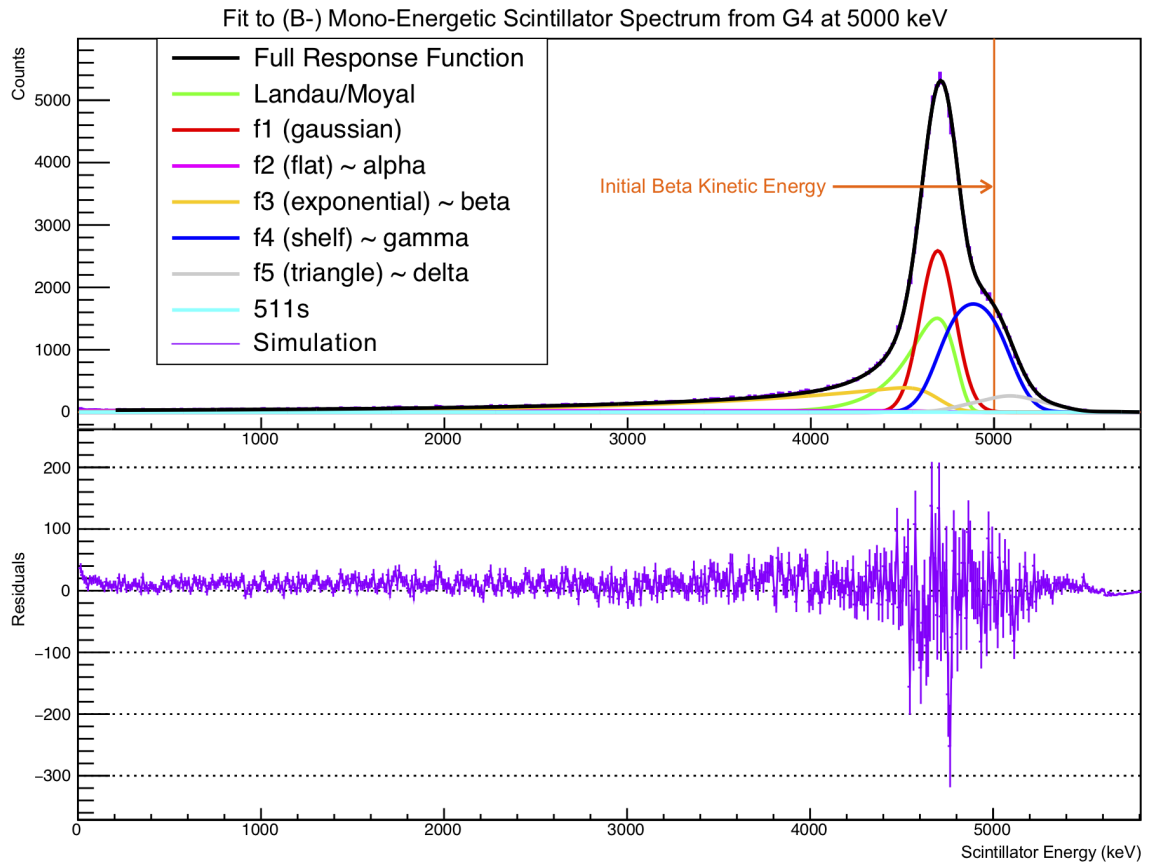


Figure 4.1: Fit to Mono-Energetic Spectrum, 5000 keV (B-)

$$R(E_0, \text{Detector}, \text{Polarization}) = p_{\text{norm}} (f_{\text{moyal}} + f_1 + f_2 + f_3 + f_4 + f_5) + f_{511} \quad (4.1)$$

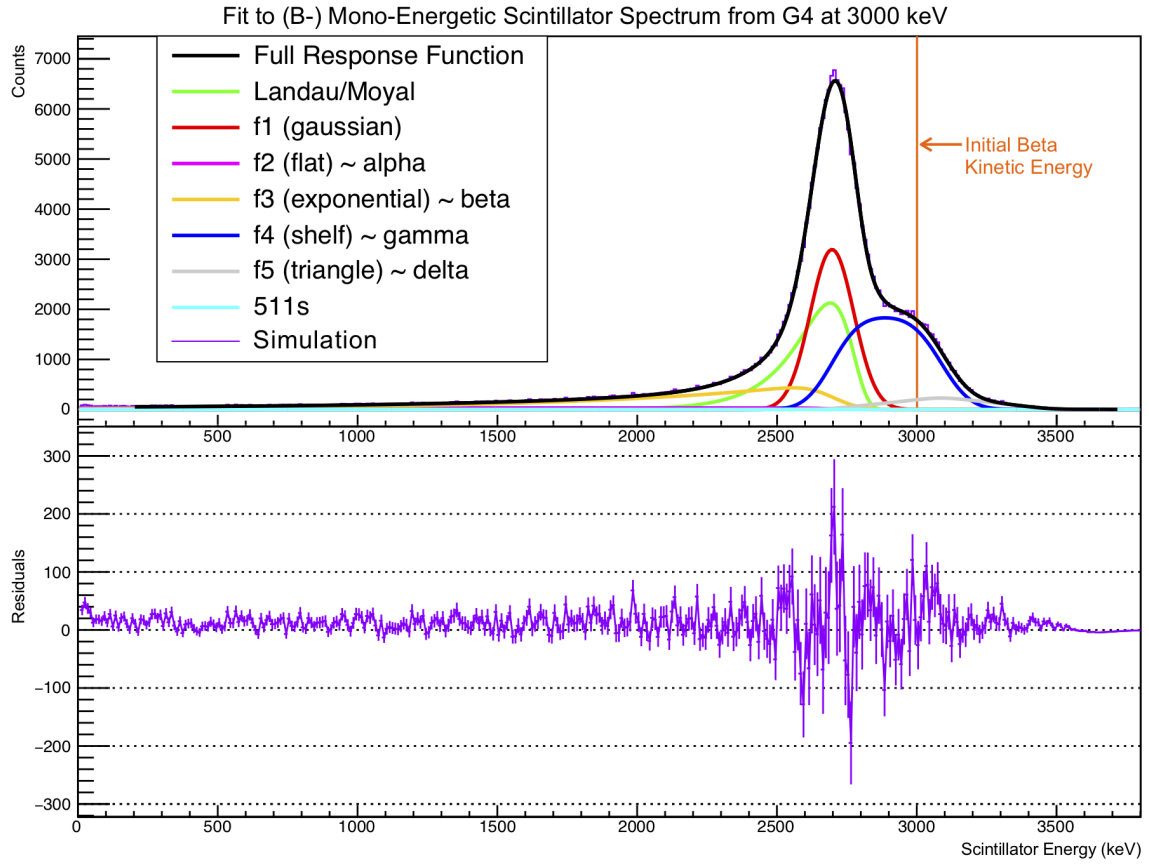


Figure 4.2: Fit to Mono-Energetic Spectrum, 3000 keV (B-)

where

$$\begin{aligned}
 f_{\text{moyal}}() &= (1 - p_{\text{gfrac}}) \left(1 + \frac{-p_\alpha - p_\beta}{|E_0|} - \frac{p_\Delta}{p_\gamma p_W} - p_\gamma p_W \right) \\
 &\times \left(\frac{e^{\left(\frac{x - (E_0 - \frac{1}{2}p_{dE0})}{2p_{lres}|E_0 - \frac{1}{2}p_{dE0}|} \right)} e^{\left(-\frac{1}{2}e^{\left(\frac{x - (E_0 - \frac{1}{2}p_{dE0})}{2p_{lres}|E_0 - \frac{1}{2}p_{dE0}|} \right)} \right)}}}{\sqrt{2\pi p_{lres} |E_0 - \frac{1}{2}p_{dE0}|}} \right) \quad (4.2)
 \end{aligned}$$

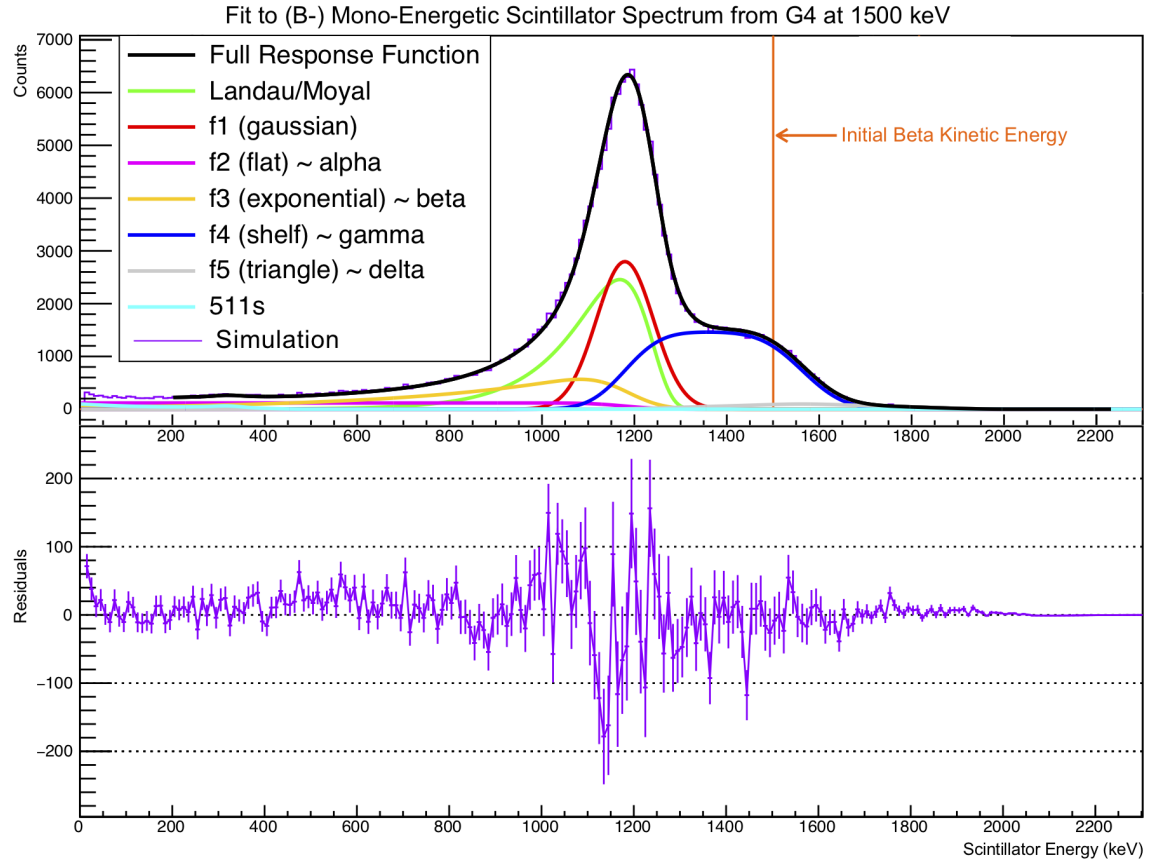


Figure 4.3: Fit to Mono-Energetic Spectrum, 1500 keV (B-)

$$\begin{aligned}
 f_1() &= p_{\text{gfrac}} \left(1 + \frac{-p_\alpha - p_\beta}{|E_0|} - \frac{p_\Delta}{p_\gamma p_W} - p_\gamma p_W \right) \left(\frac{e^{\left(-\frac{(x - (E_0 + \frac{1}{2} p_{dE0}))^2}{2 p_{\text{toeres}} |E_0 + \frac{1}{2} p_{dE0}|} \right)}}{\sqrt{2\pi p_{\text{toeres}} |E_0 + \frac{1}{2} p_{dE0}|}} \right) \\
 f_2() &= \frac{p_\alpha}{|E_0|} \left(\frac{1 - \text{Erf} \left[\frac{(x - |E_0|)}{\sqrt{2 p_{\text{toeres}} |E_0|}} \right]}{2 |E_0|} \right)
 \end{aligned} \tag{4.3}$$

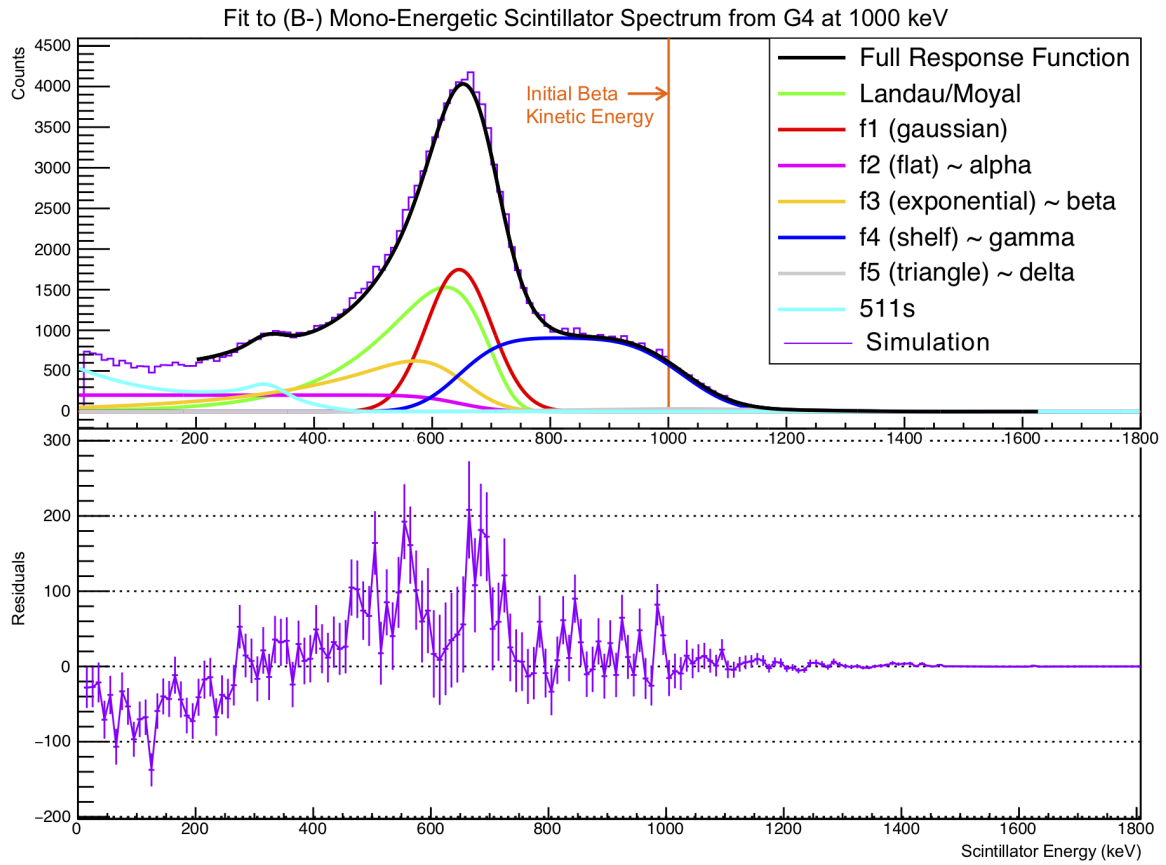


Figure 4.4: Fit to Mono-Energetic Spectrum, 1000 keV (B-)

$$f_3() = \frac{p_\beta}{|E_0|} \left(\frac{e^{\frac{p_k * (x - E_0)}{|E_0|}} * e^{\frac{p_{\text{toeres}} p_k^2}{2|E_0|}}}{2(1 - e^{-p_k})} \right) \left(1 - \text{Erf} \left[\frac{(x - E_0 + p_{\text{toeres}} p_k)}{\sqrt{2 p_{\text{toeres}} |E_0|}} \right] \right) \quad (4.4)$$

$$f_4() = \frac{p_\gamma}{2} \left(\text{Erf} \left[\frac{x - E_0}{\sqrt{(2 p_{\text{toeres}} |E_0|)}} \right] - \text{Erf} \left[\frac{x - E_0 - p_W}{\sqrt{2 p_{\text{toeres}} |E_0 + p_W|}} \right] \right) \quad (4.5)$$

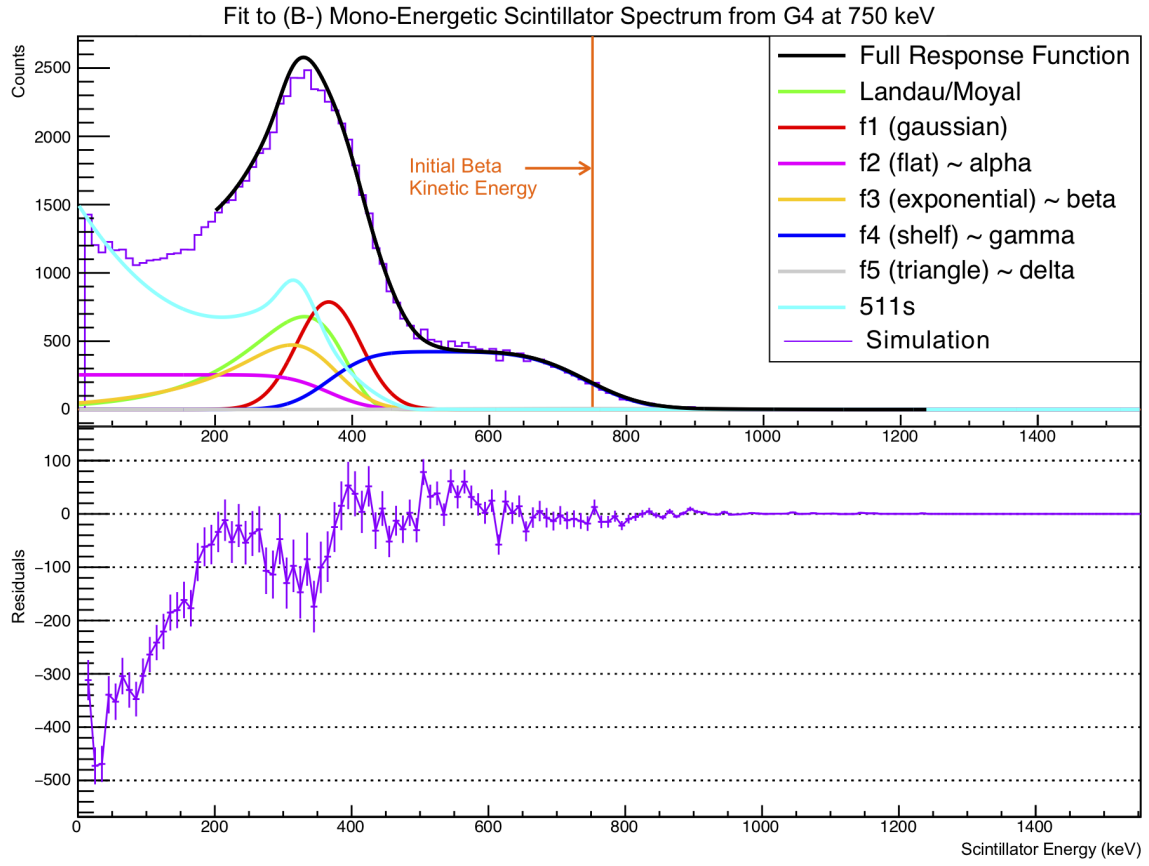


Figure 4.5: Fit to Mono-Energetic Spectrum, 750 keV (B-)

$$\begin{aligned}
 f5 = & \frac{p_\Delta}{2 p_\gamma p_W^3} \left[(x - E_0) \left(\operatorname{Erf} \left[\frac{(x - E_0)}{\sqrt{2 p_{\text{toeres}} |E_0|}} \right] - 2 \operatorname{Erf} \left[\frac{(x - E_0 - p_W)}{\sqrt{2 p_{\text{toeres}} |E_0 + p_W|}} \right] \right. \right. \\
 & + \operatorname{Erf} \left. \left[\frac{(x - E_0 - 2p_W)}{\sqrt{2 p_{\text{toeres}} |E_0 + 2p_W|}} \right] \right) + (2 p_W) \left(\operatorname{Erf} \left[\frac{(x - E_0 - p_W)}{\sqrt{2 p_{\text{toeres}} |E_0 + p_W|}} \right] \right. \\
 & - \operatorname{Erf} \left. \left[\frac{(x - E_0 - 2p_W)}{\sqrt{2 p_{\text{toeres}} |E_0 + 2p_W|}} \right] \right) + (2 p_{\text{toeres}} |E_0|) \left(\left(\frac{e^{\left(\frac{-(x - E_0)^2}{(4 p_{\text{toeres}} |E_0|)} \right)}}{\sqrt{2\pi p_{\text{toeres}} |E_0|}} \right) \right. \\
 & \left. \left. + \left(\frac{-2e^{\left(\frac{-(x - E_0 - p_W)^2}{(4 p_{\text{toeres}} |E_0 + p_W|)} \right)}}{\sqrt{2\pi p_{\text{toeres}} |E_0 + p_W|}} \right) + \left(\frac{e^{\left(\frac{-(x - E_0 - 2p_W)^2}{(4 p_{\text{toeres}} |E_0 + 2p_W|)} \right)}}{\sqrt{2\pi p_{\text{toeres}} |E_0 + 2p_W|}} \right) \right) \right) \quad (4.6)
 \end{aligned}$$

$$f_{511} = |p_{\text{scale}}| \left[\left(\frac{195}{17} \sqrt{\frac{2}{\pi}} e^{\left(\frac{-(x-308)^2}{578} \right)} \right) + \left(40 + \frac{(x-210)^2}{900} \right) \left(1 - \text{Erf} \left[\frac{x-334}{30} \right] \right) \right. \\ \left. + \left(\frac{(x-505)^2}{1440} \right) \left(1 - \text{Erf} \left[\frac{x-505}{30} \right] \right) \left(1 + \text{Erf} \left[\frac{x-334}{30} \right] \right) \right] \quad (4.7)$$

- ... And then, you have values of all the parameters, as measured at a bunch of input energies. Make sure all the fits converge and don't do something crazy.
- Fit all the parameters as a function of energy to empirical functions. Doesn't even matter what the form of the functions are, as long as it fits well.
- the parameters extracted from the mono-energetic beta spectrum fits, and empirical functions to model how these parameters vary with beta energy, are shown in Figs. 4.6, 4.7, 4.8, and 4.9.
- How good are these fits, you ask? See Fig. 4.10

4.3 Simulating the Background

Our experiment has some background. It's annoying and stupid, but as long as we can estimate how much of it there is and what it does, it's basically fine.

- TOF cut requires a whole extra model of background in the TOF spectrum..
- Suppose background in the TOF spectrum is coming from decays of atoms that have gotten themselves stuck to surfaces within the chamber...
- Run G4 to get a beta TOF spectrum (w.r.t. the decay)
- Run COMSOL (credit to Alexandre) to track low-energy SOEs through the electric field from wherever they started, into the detectors. Energy spectra from Levinger.
- Combine G4 and COMSOL spectra, event-by-event, while requiring that both the beta detector and the eMCP are hit according to the set of random numbers

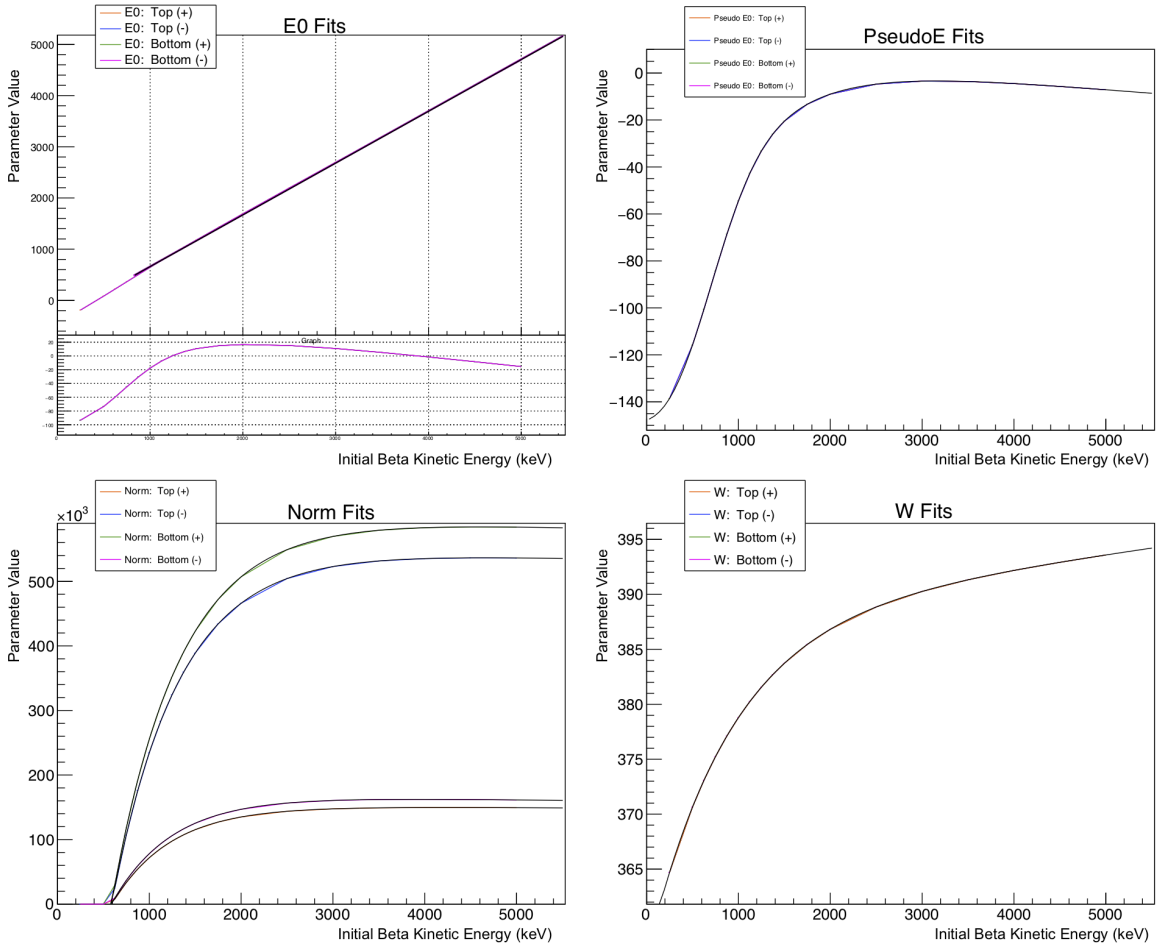


Figure 4.6: Lineshape Parameter Fits (Part 1)

generated by each monte carlo separately. Then, the beta and SOE will each have a TOF from decay to detector, and subtracting one from the other gives a timing spectrum that can be observed experimentally. See Fig. 3.9.

- Upper limit for the fraction of events generated this way can be estimated by assuming that all losses from the trap not due to radioactive decay emerge isotropically from the trap and then stick to whatever chamber wall is in its path. This upper limit is too big by a factor of 2.
- For each of those 3 simulations, sort the “good” data according to emission angle relative to the detector. Do each detector individually. For both polarizations.
- Assemble the (simulated) superratio asymmetry. We’ll compare it to data, and

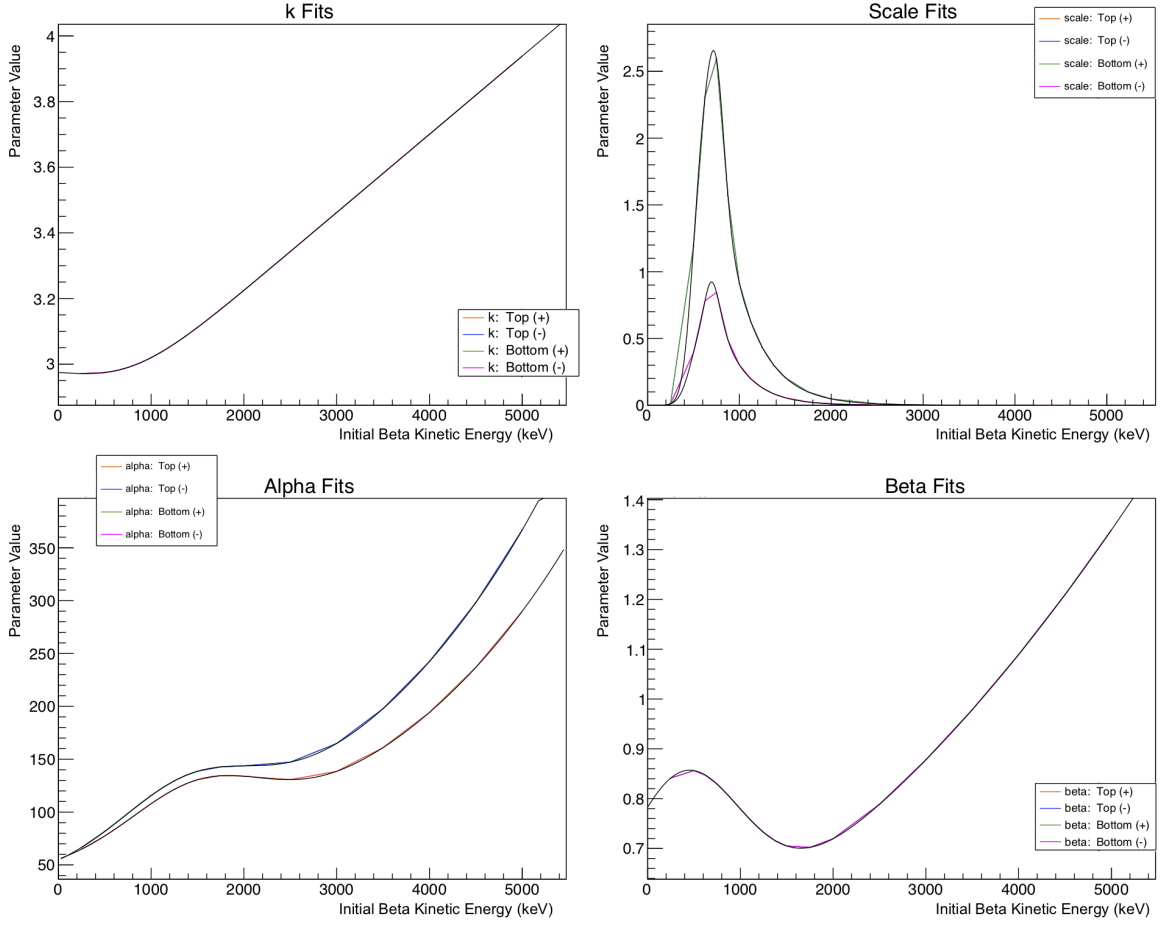


Figure 4.7: Lineshape Parameter Fits (Part 2)

the χ^2 from that comparison will be our figure of merit.

- We can make a whole 2D parameter space for different values of A_β and b_{Fierz} , and compare them all (via their superratio asymmetries) to the experimental data. We get the “best” values of A_β and b_{Fierz} , where χ^2 is minimized.
- We can do this whole thing again for simulated data sets with different values of parameters that we vary as systematics. Note how the best values of A_β and b_{Fierz} change when each of the systematics are varied.

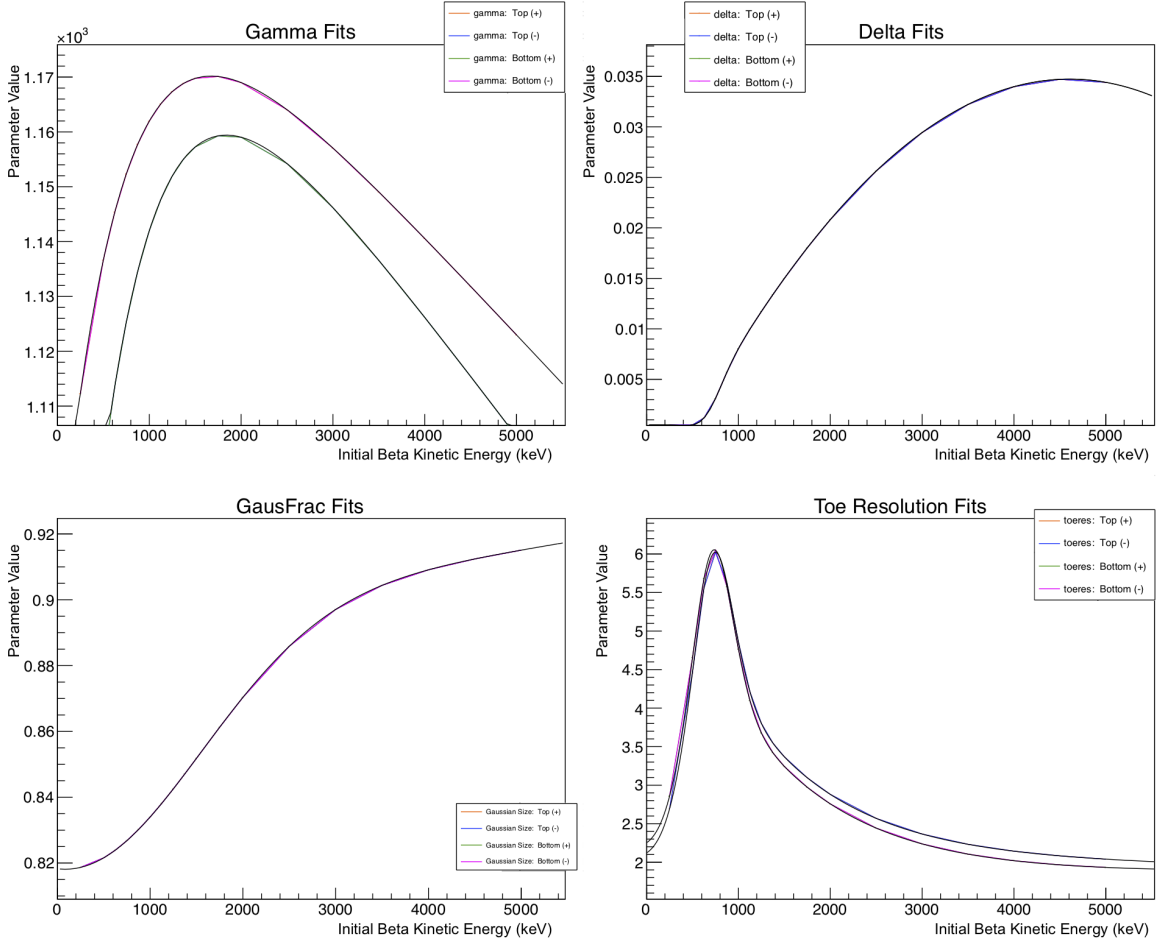


Figure 4.8: Lineshape Parameter Fits (Part 3)

4.4 Comparing Simulations with Experimental Data

- Run 3 sets of G4 simulations with a bunch of statistics (N events, for data with like $N/10$ events). Each one has the same nominal value of A_β , but with 3 different values of the scalar coupling C_S : zero, and $+/-$ (whatever). Keep $C_T = 0$. Because reasons, we're not really able to distinguish between C_S and C_T in this experiment anyway, so might as well keep the analysis simple.
- Just run one set of $0.02*N$ events for the two percent branch. We can't neglect it, but it isn't going to change much when we adjust BSM couplings. Just use the old event generator from Holstein Eq. (51).
- Match cuts in simulated data up to the cuts on experimental data. Obviously.

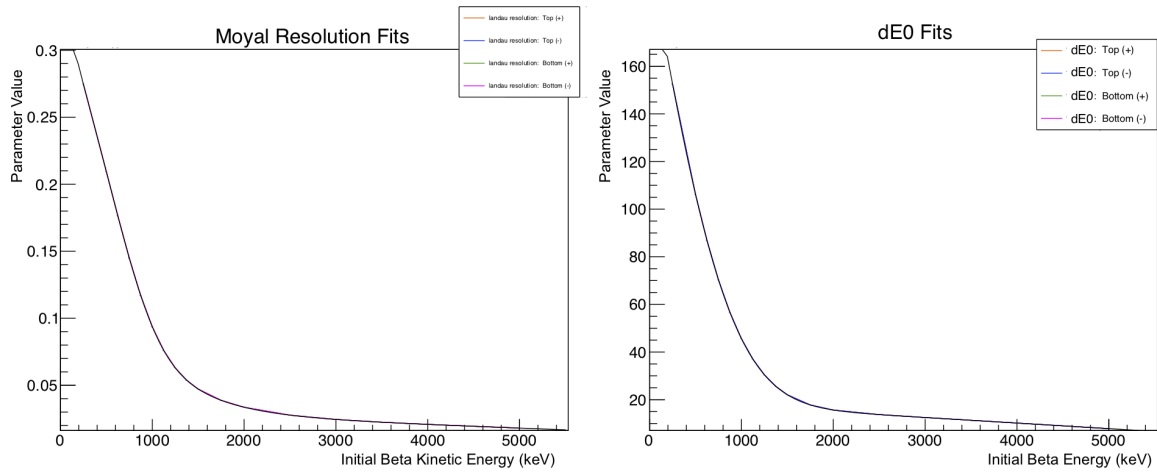


Figure 4.9: Lineshape Parameter Fits (Part 4)

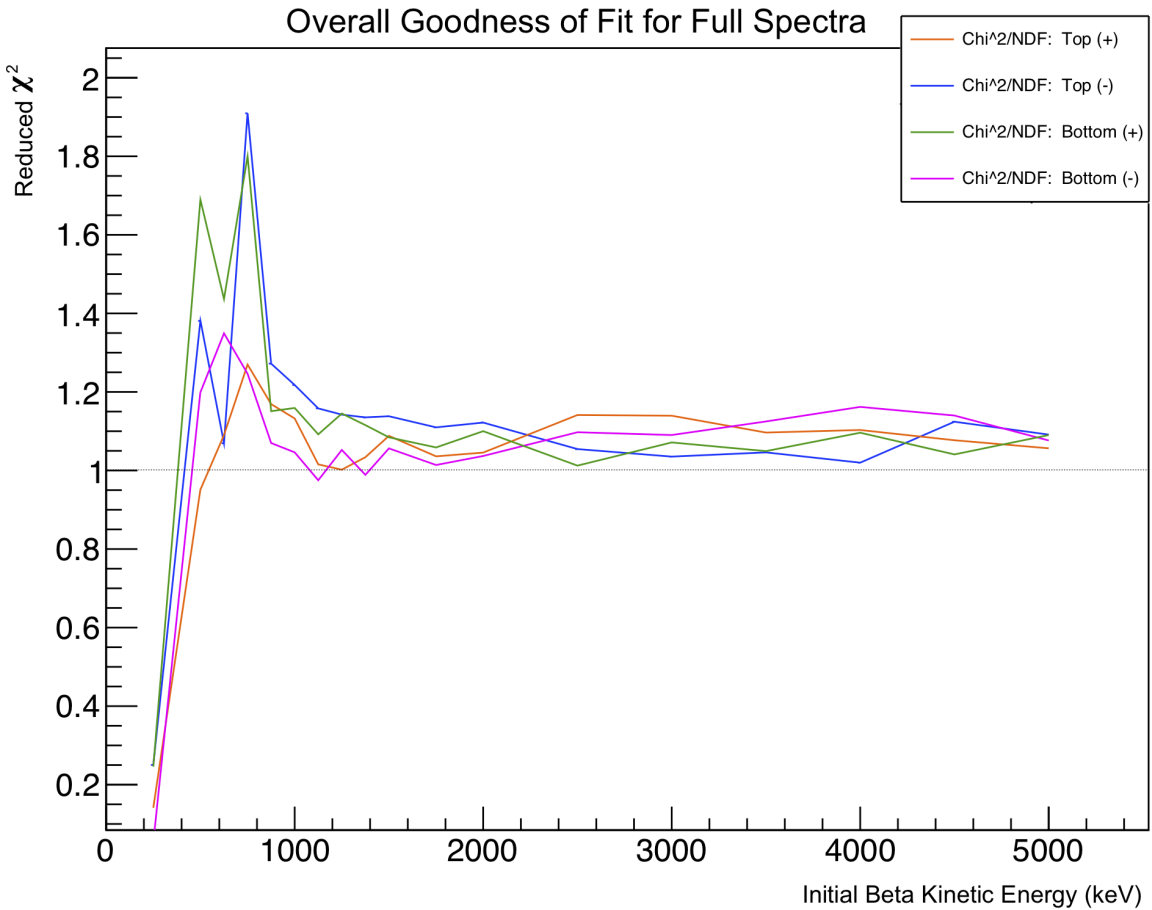


Figure 4.10: Goodness of Fit for Modeled Lineshapes

DSSD cut, DSSD energy, one hit DSSD, one hit scint. TOF cut, which requires a whole extra model of background in the TOF spectrum (see Section 4.3).

Chapter 5

Analysis and Estimates of Systematic Effects

I really need an excuse to include more pictures of data. Also, more pictures of simulations.

Analysis is critical to a precision measurement, as most of the research is in determining systematic uncertainties by self-consistent analysis and simulations. Each detector in this experiment is critical and has independent calibrations and cuts. Full explanation is here (and in two following chapters) justifying choice of the deterministic cuts, because in the analysis in this thesis the data was not blinded. The main goal of blinding was nevertheless achieved— to make sure all analysis is done completely with full redundancy of checks wherever possible— so the discipline entailed must be described in full detail. Here there are details of detectors: eMCP rMCP beta DSSD scintillator.

The collaboration has done an independent analysis fixing $bFierz$ to zero. Differences with that analysis are interleaved in this section. Critical physics improvements concern an emcp-beta timing walk correction which enabled an improved cut against background, also incorporating a more complete modelling of decay backgrounds from untrapped atoms. Technical corrections include a correct treatment of the polarization cycle. An arbitrary change in the δE radius cut is kept self-consistent.

5.1 Overview

A summary of systematics goes here. In words, yes, but also in table form.

Source	b_{Fierz}		A_β	
	Uncertainty	Correction	Uncertainty	Correction
Scintillator Calibration	0.003	-	0.0003	-
Scintillator Threshold	0.004	-	0.0004	-
DSSD Individual Strip SNR	0.006	-	0.0007	-
DSSD Energy Agreement	0.005	-	0.0006	-
DSSD Detection Radius	0.006	-	0.0017	-
DSSD Energy Threshold	0.005	-	0.0005	-
Atomic Cloud	0.002	(...)	0.0002	(...)
Background	0.004	(...)	0.0003	(...)
Beta Scattering	0.031	(...)	0.0025	(...)
Low Energy Tail	0.008	-	0.0007	-
Mirror Thickness	0.026	-	0.0025	-
DSSD Thickness	0.026	-	0.0025	-
Be Foil Thickness	0.026	-	0.0025	-
Total Systematics	0.056	-	0.0055	-
Statistics	0.084	-	0.0082	-

Table 5.1: Error Budget goes here.

Choice of low-energy scintillator threshold has a large systematic effect...

5.2 BB1 Radius, Energy Threshold, Agreement

BB1 radius cut can help to eliminate scattered events. Energy threshold selection and statistical agreement between BB1 detectors' energies only makes a small effect on results. BB1 radius itself has a pretty big effect on the result, but we can at least just G4 it away. The remaining systematic effect is pretty small.

In the end, we get our results from the scintillator energy only, without summing the BB1 energy back in. Energy absorbed in DSSDs is only used as (a) a tag for events, and (b) contributing to the total beta energy loss before the beta arrives at the scintillator.

5.3 Background Modeling – Decay from Surfaces within the Chamber

So many surfaces, all of which can get stray 37K atoms stuck to them. Then they decay from a place that isn't the actual trap center, and it contaminates our stuff.

We model the beta TOF from the surfaces in G4, event by event. This is necessary because scattered events will have their TOF changed to account for a longer beta pathlength, and we're preferentially cutting away the events that don't have a TOF in the appropriate range.And then have COMSOL generate electron TOFs for SOEs starting from the start points picked by G4. Ran COMSOL for 0 eV SOEs, and again for Levinger spectrum SOEs. Used 9% 0eV SOEs in the end. I forget which Levinger distribution I used in the end. The point is, for each event, you've simulated a beta TOF that may or may not be scattered off of something before it hits a detector, and you have a SOE TOF for an event originating at that same point, so you subtract them to model the TOF you'd measure in an experiment. Also, because you've done the scattering with G4, you get the beta energy corrected for any scattering that happened. This way, one can estimate how many "bad" events are eliminated with the TOF cut, as well as the fraction of "bad" events left in what remains.

5.4 Quantifying the Effects of Backscatter with Geant4

Beta decay (back-)scatter from surfaces within the experimental chamber is a significant systematic, and it must be evaluated, quantified, and corrected for. This is done via a series of GEANT4 simulations. While only a small fraction of events are affected, the process results in an energy loss in the beta that can, if not understood, be misinterpreted as the exact signal we're searching for. It is therefore imperative that this be well understood.

5.5 Lineshape Reconstruction

Clifford tells us what to do. [10].

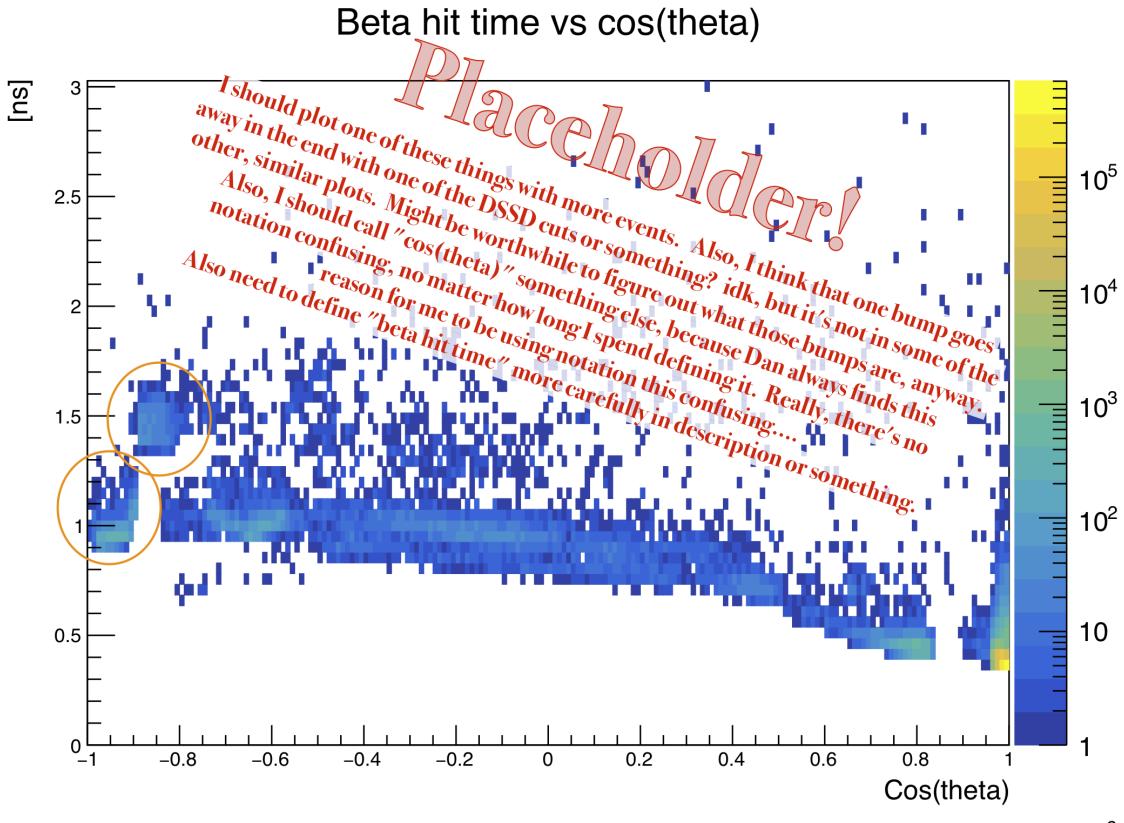


Figure 5.1: Simulated Beta TOA vs emission angle w.r.t. detector orientation

5.5.1 Motivation

This process is used because the (back-)scatter, which it itself an important systematic, is largely independent of a wide variety of other experimental effects. These other effects must all be evaluated, but it is computationally prohibitive to re-evaluate the scattering with every other effect under consideration.

5.5.2 What is it and how does it work?

Mono-energetic beta decay events are generated in GEANT4, which outputs an energy spectrum for unscattered and forward-scattered beta events in the detector. These spectra are fit to a function to model the scintillator resolution, as well as energy loss in materials that the beta passed through before arriving at the scintillator. These spectrum fits are performed for a set of beta energies, and parameters are extrapolated

to be applied to betas emitted at intermediate energies. Thus, the whole spectrum can be modeled. Pictures will make this clearer.

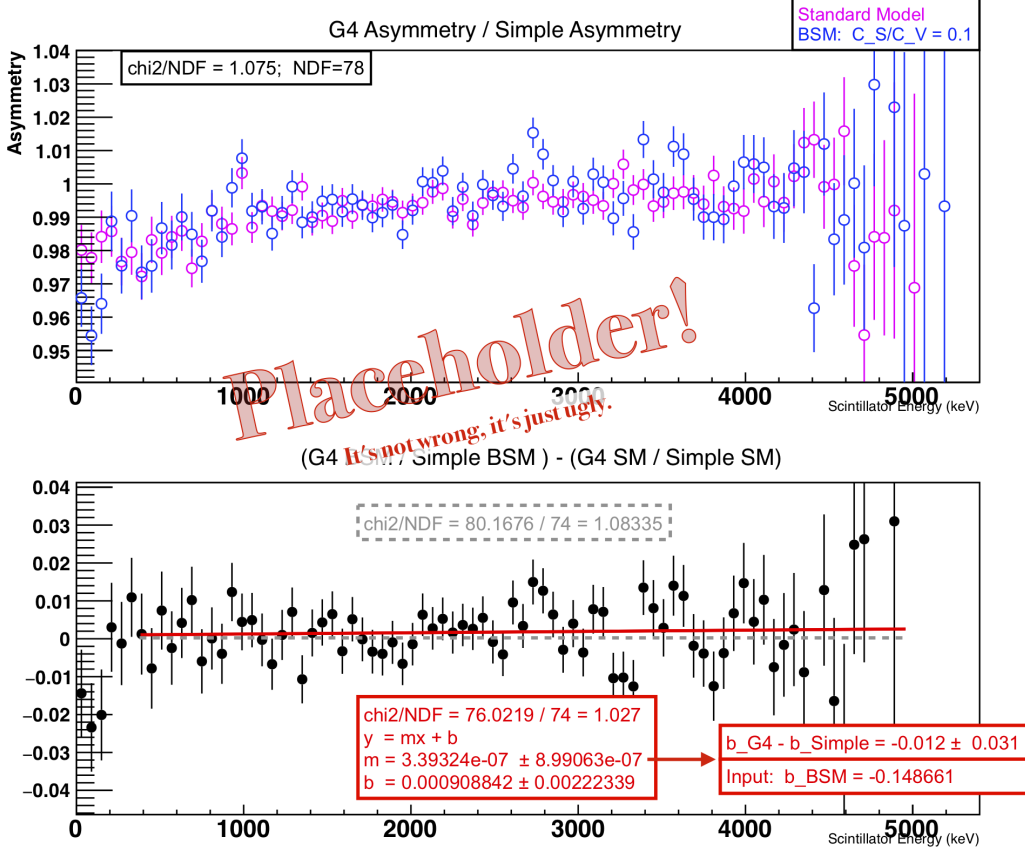


Figure 5.2: I'm not actually sure if this picture shows what I want it to. The point is, if I apply this rough lineshape to stuff that I SimpleMC-ed, then I can evaluate that way various systematic effects that would be time-consuming to actually simulate with G4. This picture is *supposed* to be a demonstration that this approach actually works...

5.5.3 The Math-Specifics

I'll write down the specific functions I'm using, and the parameter values I'm using. (Maybe this should go in an appendix instead?) I'll describe the adjustments I make to the spectrum so that it can work even for the dataset where the scintillators' resolutions have changed.

5.5.4 The Results – Things That Got Evaluated This Way

As it turns out, only cloud parameters were evaluated this way. Trap position, size, sail velocity, temperature. But then we varied the lineshape anyhow, to account for G4 doing a bad job of modelling the bremsstrahlung (sp?).

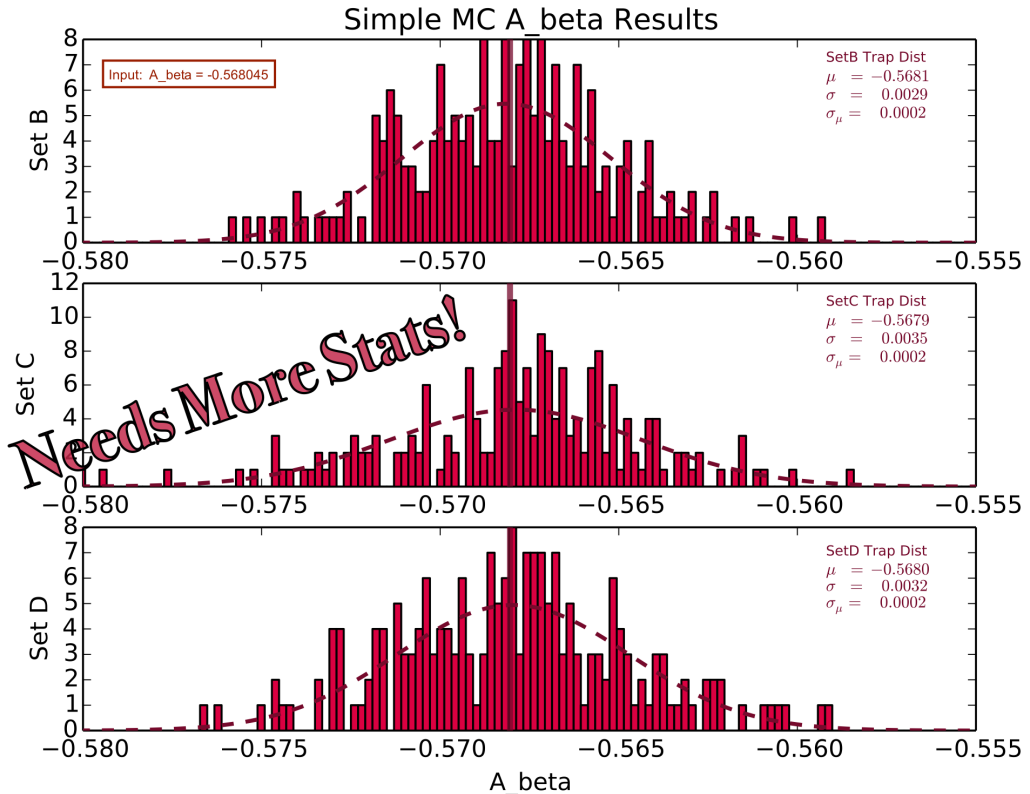


Figure 5.3: Estimated uncertainty in A_β resulting from uncertainty and variation in the cloud parameters. Evaluated by the lineshape reconstruction method.

5.5.5 The low-energy tail uncertainty, and what it does

Bremsstrahlung. It does Bremsstrahlung.

This subsection has the collaboration's evaluation of the uncertainty from the scintillator detector's lineshape tail. The energy from a monoenergetic beta is not always fully absorbed in a plastic scintillator. Although most backscattered betas are vetoed by the DSSD, some produce bremsstrahlung photons, and these frequently

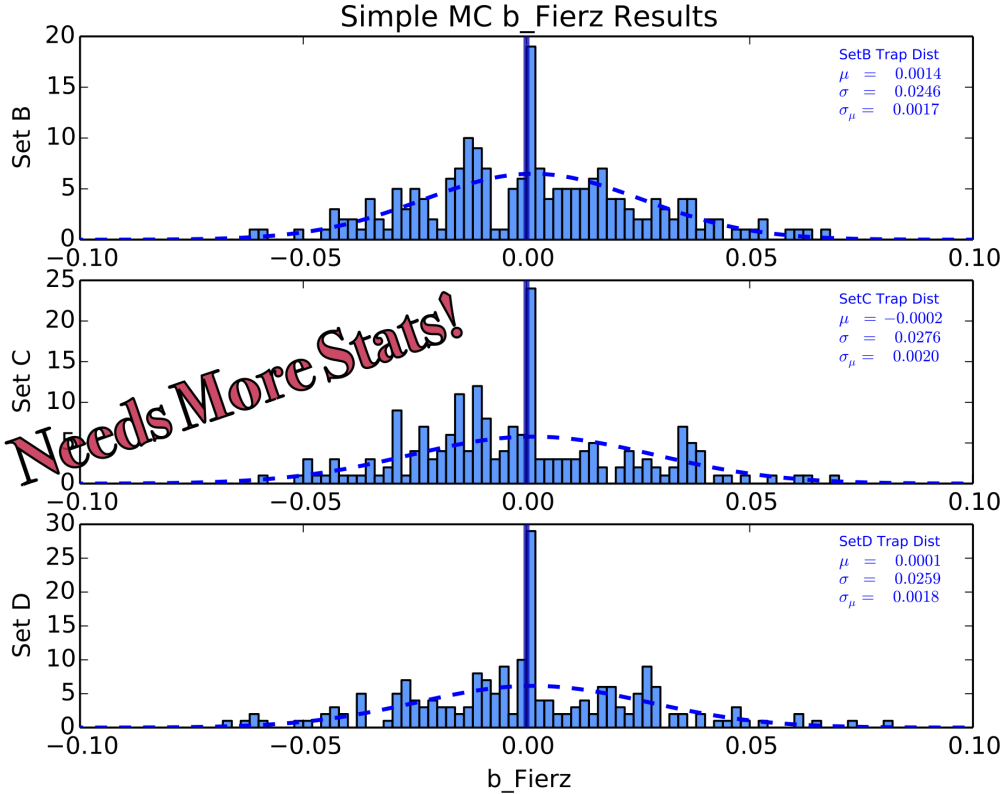


Figure 5.4: Estimated uncertainty in b_{Fierz} resulting from uncertainty and variation in the cloud parameters. Evaluated by the lineshape reconstruction method.

escape low-Z plastic scintillator— all cross-sections are known to high accuracy, but there is always uncertainty entailed in the MC implementation. This lineshape tail will then effectively move events from higher to lower measured energy, artificially altering the lower-energy asymmetries and mimicking the effects of a Fierz term.

Since this detector effect is difficult to disentangle from the other scattering effects off volumes, the collaboration adds a linear function down to zero for the tail to a Gaussian for the peak, with linewidth varying by photon statistics [10]. The convolution of this simple detector response function with v/c then scales the centroid MC, with the lineshape tail varied by $\pm 10\%$ of its value, a generic uncertainty accepted by the community for MC electromagnetic simulations. The fit b_{Fierz} centroid changes by ± 0.0076 , summarized as the 0.008 “Low Energy Tail” in the systematics table at the start of this chapter. Compared to other uncertainties of the present data set,

this is small enough that the accuracy of this estimate is adequate.

Chapter 6

Results and Conclusions

6.1 Measured Limits on b_{Fierz}

Results go here, with measured limits described and quantified in all formats anyone could ever care about.

6.2 Discussion of Corrections and Uncertainties

6.3 Relation to Other Measurements and New Overall Limits

In which I'll show exclusion plots and write down new limits, combining my result with results from the literature. Or, y'know, maybe I'll just talk about doing that.

6.4 R_{slow} and Other Possible Future Work for the Collaboration

The nuclear weak force is known to be a predominantly left-handed vector and axial-vector (V-A) interaction. An experiment is proposed to further test that observation, constraining the strength of right-handed (V+A) currents by exploiting the principle of conservation of angular momentum within a spin-polarized beta decay

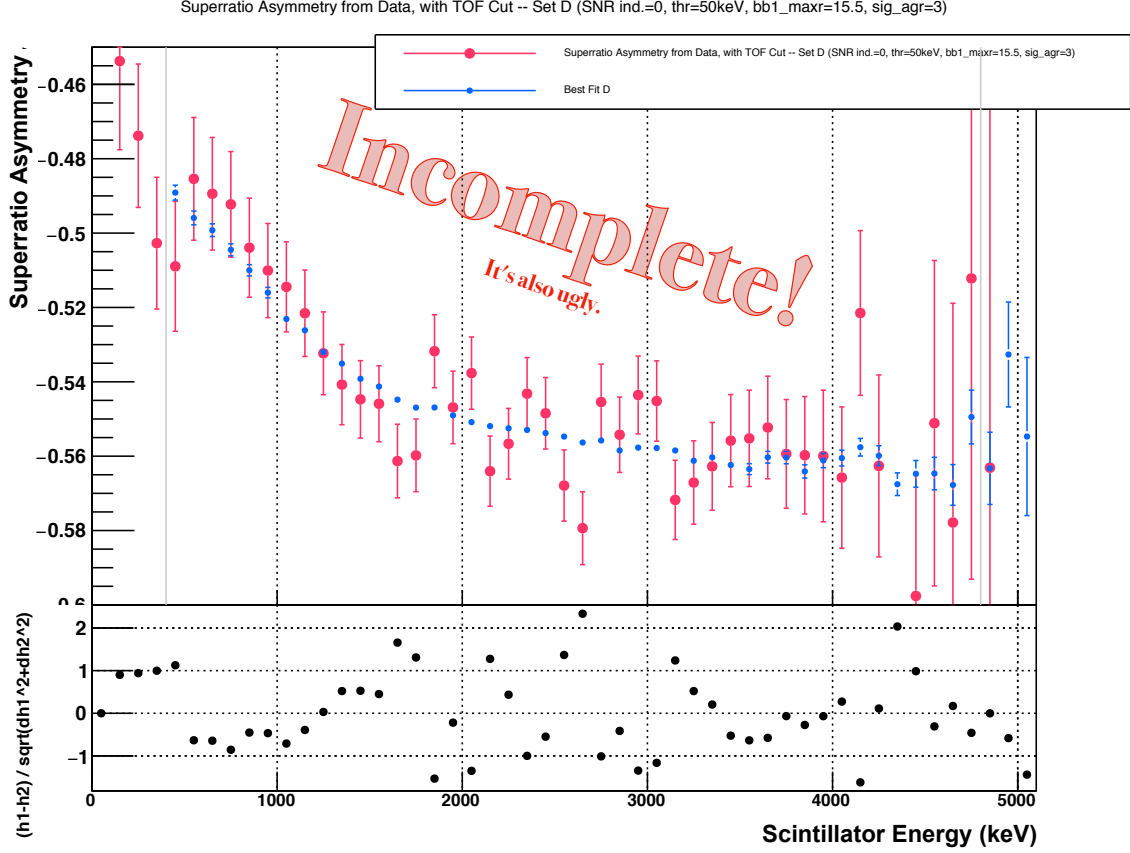


Figure 6.1: A superratio asymmetry from the data, and the best fit from simulations.

process. Here, we focus on the decay $^{37}\text{K} \rightarrow ^{37}\text{Ar} + \beta^+ + \nu_e$. The angular correlations between the emerging daughter particles provide a rich source of information about the type of interaction that produced the decay.

6.4.1 Motivation

The nuclear weak force has long been known to be a predominantly left-handed chiral interaction, meaning that immediately following an interaction (such as a beta decay) with a weak force carrying boson (W^+ , W^- , Z), normal-matter leptons (such as the electron and electron neutrino) emerge with left-handed chirality while the anti-leptons (e.g. the positron and electron anti-neutrino) emerge with right-handed chirality. In the limit of massless particles, the particle's chirality is the same as its helicity. Thus, in a left-handed model, the direction of an (ultrarelativistic) normal

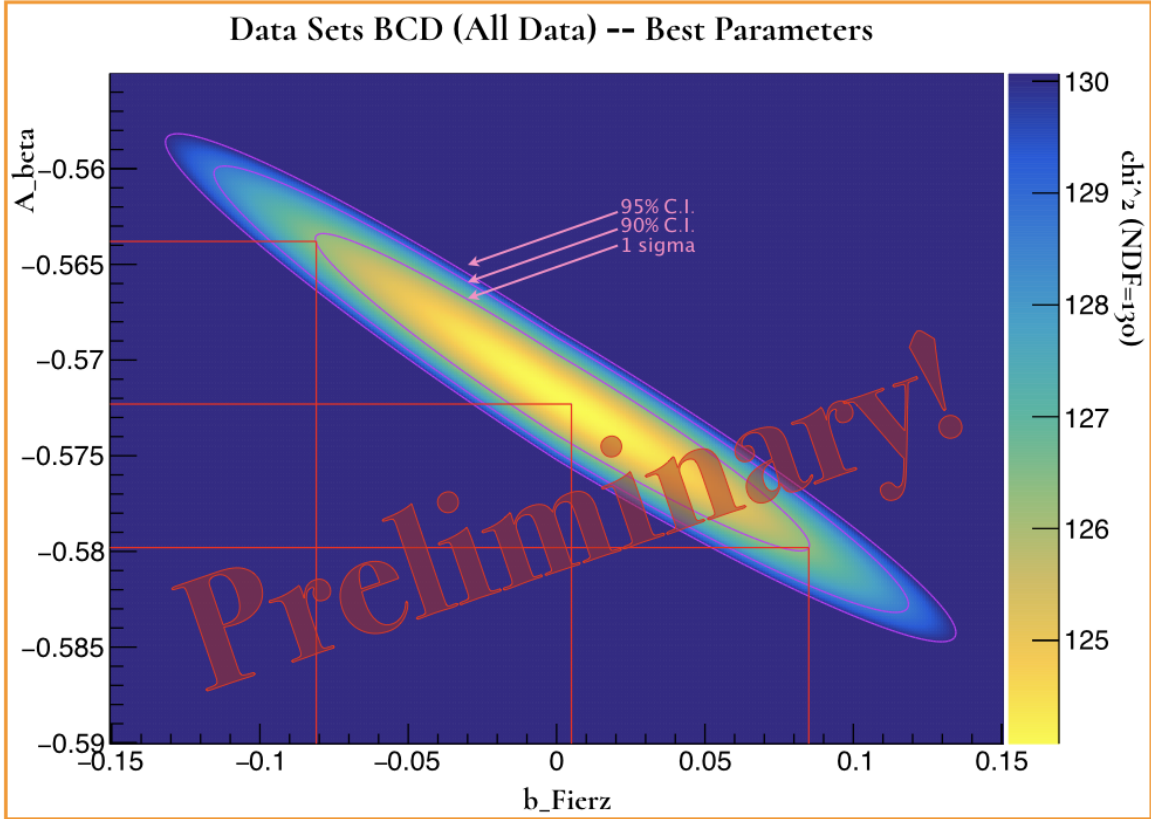


Figure 6.2: Some results. I'll want to show at least one of these things. Probably show a separate one for each runset, actually.

lepton's spin is antiparallel direction of its motion, and the direction of spin for an anti-lepton is parallel to its direction of motion. For a non-relativistic particle the property of chirality is fairly abstract, and describes the appropriate group representation and projection operators to be used in calculations. It should be noted that a fully chiral model is also one which is maximally parity violating.

This odd quirk of the nuclear weak force is not only *predominantly* true, but it is, to the best of our current scientific knowledge, *always* true – that is, attempts to measure any right-handed chiral components of the weak force have produced results consistent with zero [14][25]. This project proposes a further measurement to constrain the strength of the right-handed component of the weak interaction.

6.4.2 The Decay Process

The kinematics of nuclear β^+ decay are described by the following probability density function:

$$\begin{aligned}
W(\langle I \rangle | E_\beta \hat{\Omega}_\beta \hat{\Omega}_\nu) = & \left(\frac{1}{2\pi} \right)^5 F(-Z, E_\beta) p_\beta E_\beta (E_0 - E_\beta)^2 dE_\beta d\hat{\Omega}_\beta d\hat{\Omega}_\nu \xi \left[1 + a_{\beta\nu} \frac{\vec{p}_\beta \cdot \vec{p}_\nu}{E_\beta E_\nu} + b_{\text{Fierz}} \frac{m_e}{E_\beta} \right. \\
& + c_{\text{align}} \left(\frac{\frac{1}{3} \vec{p}_\beta \cdot \vec{p}_\nu - (\vec{p}_\beta \cdot \hat{j})(\vec{p}_\nu \cdot \hat{j})}{E_\beta E_\nu} \right) \left(\frac{I(I+1) - 3\langle (\vec{I} \cdot \hat{i})^2 \rangle}{I(2I-1)} \right) \\
& \left. + \frac{\langle \vec{I} \rangle}{I} \left(A_\beta \frac{\vec{p}_\beta}{E_\beta} + B_\nu \frac{\vec{p}_\nu}{E_\nu} + D_{\text{TR}} \frac{\vec{p}_\beta \times \vec{p}_\nu}{E_\beta E_\nu} \right) \right],
\end{aligned} \tag{6.1}$$

where \vec{I} is the nuclear spin-polarization, $F(-Z, E_\beta)$ is the Fermi function, and parameters ξ , $a_{\beta\nu}$, b_{Fierz} , c_{align} , A_β , B_ν , and D_{TR} are functions that vary with the strengths of the vector, axial, scalar, and tensor couplings (constant throughout nature), as well as the Fermi and Gamow-Teller nuclear matrix elements (specific to the individual decay) [5][16].

The decay may be treated as a three-body problem in which the available kinetic energy is divided up between the beta, the neutrino, and the recoiling ^{37}Ar nucleus, and (of course) the total linear and angular momentum are conserved. While the neutrino cannot be detected directly, its kinematics may be reconstructed from observations of the beta and the recoiling daughter nucleus. By placing detectors above and below the decaying atom along the axis of its polarization, we are able to obtain information about the outgoing beta's energy and momentum, in the cases of interest to us, where it is emitted along (or close to) the axis of polarization.

The recoiling ^{37}Ar nucleus is a bit trickier to work with, but the task is not impossible. One useful feature of the $^{37}\text{K} \rightarrow {}^{37}\text{Ar}$ transition is that, in addition to the β^+ emitted in the decay itself, one or more *orbital* electrons from the parent atom are typically lost. In the majority of decay events only one orbital electron is ‘shaken off’ and so the daughter ^{37}Ar atom is electrically neutral [20][26]. In the remaining cases, two or more orbital electrons are lost this way, and the daughter atom is positively charged. If we apply an electric field perpendicular to the direction of polarization, these positively charged $^{37}\text{Ar}^{(+n)}$ ions may be collected into a detector, from which hit position and time of flight information may be extracted. These shake-off electrons

are emitted with an average energy of only ~ 2 eV so to a very good approximation the other decay products are not perturbed by the presence of shake-off electrons.

It should be noted that for the class of decays of greatest interest, where the beta and the neutrino emerge back-to-back along the polarization axis, the recoiling daughter nucleus will have zero momentum along the directions perpendicular to this axis, and on average less total energy than if the beta and neutrino were emitted in a parallel direction. Henceforth, daughter nuclei from a back-to-back decay as shown in Figure ?? will be described as ‘slow’ recoils. In terms of observables, this means that if the electric field is configured to point along one of the axes perpendicular to the polarization direction, then when the recoiling ion is swept away into a detector, the slow recoil’s hit position should be exactly along the projection of the polarization axis. Furthermore, the slow recoil’s time of flight should be in the middle of the time of flight spectrum, since other recoils will be emitted with momentum towards or away from the detector.

6.4.3 Current Status

In June 2014, after several years of preparatory work beforehand (the author has been continuously involved with this project since 2010), approximately 7 days of beam time at TRIUMF was dedicated to the TRINAT ^{37}K beta decay experiment. Approximately half of this data is suitable for use in this project. During this period, approximately 10,000 atoms were held within the trap at any given time. The cleaned spectra show around 50,000 polarized beta-recoil coincidence events in total, divided among measurements at three different electric field strengths (535 V/cm, 415 V/cm, 395 V/cm).

A fit to simulation has shown that the data that has already been collected has sufficient statistical power to measure the *fractional* contribution of any polarized ‘new physics’ beta decay parameter (ie right-handed, scalar, and tensor currents within the weak interaction) to a sensitivity of $\sim 2\%$ of its true value. Systematic limitations are still being assessed.

6.5 Conclusions

Conclusions go here.

Bibliography

- [1] Fenker, B., Behr, J. A., Melconian, D., Anderson, R. M. A., Anholm, M., Ashery, D., Behling, R. S., Cohen, I., Craiciu, I., Donohue, J. M., Farfan, C., Friesen, D., Gorelov, A., McNeil, J., Mehlman, M., Norton, H., Olchanski, K., Smale, S., Thériault, O., Vantyghem, A. N. and Warner, C. L., *Precision measurement of the nuclear polarization in laser-cooled, optically pumped ^{37}K* , New Journal of Physics, Vol. 18, No. 7, pp. 073028, 2016.
- [2] Anholm, M., Characterizing the AC-MOT, Master's thesis, University of British Columbia, 2014.
- [3] Falkowski, A., González-Alonso, M. and Naviliat-Cuncic, O., *Comprehensive analysis of beta decays within and beyond the Standard Model*, Journal of High Energy Physics, Vol. 2021, No. 4, pp. 1–36, 2021.
- [4] Hong, R., Sternberg, M. G. and Garcia, A., *Helicity and nuclear β decay correlations*, American Journal of Physics, Vol. 85, No. 1, pp. 45–53, 2017.
- [5] Jackson, J. D., Treiman, S. B. and Wyld, H. W., *Possible Tests of Time Reversal Invariance in Beta Decay*, Phys. Rev., Vol. 106, pp. 517–521, May 1957.
- [6] Levinger, J. S., *Effects of Radioactive Disintegrations on Inner Electrons of the Atom*, Phys. Rev., Vol. 90, pp. 11–25, Apr 1953.
- [7] Harvey, M. and Murray, A. J., *Cold Atom Trap with Zero Residual Magnetic Field: The AC Magneto-Optical Trap*, Phys. Rev. Lett., Vol. 101, pp. 173201, Oct 2008.
- [8] Sun, X., Adamek, E., Allgeier, B., Bagdasarova, Y., Berguno, D. B., Blatnik, M., Bowles, T. J., Broussard, L. J., Brown, M. A.-P., Carr, R., Clayton, S.,

- Cude-Woods, C., Currie, S., Dees, E. B., Ding, X., Filippone, B. W., García, A., Geltenbort, P., Hasan, S., Hickerson, K. P., Hoagland, J., Hong, R., Holley, A. T., Ito, T. M., Knecht, A., Liu, C.-Y., Liu, J., Makela, M., Mammei, R., Martin, J. W., Melconian, D., Mendenhall, M. P., Moore, S. D., Morris, C. L., Nepal, S., Nouri, N., Pattie, R. W., Pérez Gálvan, A., Phillips, D. G., Picker, R., Pitt, M. L., Plaster, B., Salvat, D. J., Saunders, A., Sharapov, E. I., Sjue, S., Slutsky, S., Sondheim, W., Swank, C., Tatar, E., Vogelaar, R. B., VornDick, B., Wang, Z., Wei, W., Wexler, J. W., Womack, T., Wrede, C., Young, A. R. and Zeck, B. A., *Improved limits on Fierz interference using asymmetry measurements from the Ultracold Neutron Asymmetry (UCNA) experiment*, Phys. Rev. C, Vol. 101, pp. 035503, Mar 2020.
- [9] Saul, H., Roick, C., Abele, H., Mest, H., Klopf, M., Petukhov, A. K., Soldner, T., Wang, X., Werder, D. and Märkisch, B., *Limit on the Fierz Interference Term b from a Measurement of the Beta Asymmetry in Neutron Decay*, Phys. Rev. Lett., Vol. 125, pp. 112501, Sep 2020.
 - [10] Clifford, E., Hagberg, E., Koslowsy, V., Hardy, J., Schmeing, H. and Azuma, R., *Measurements of the response of a hybrid detector telescope to mono-energetic beams of positrons and electrons in the energy range 0.8–3.8 MeV*, Nuclear Instruments and Methods in Physics Research, Vol. 224, No. 3, pp. 440–447, 1984.
 - [11] Saul, H., Roick, C., Abele, H., Mest, H., Klopf, M., Petukhov, A. K., Soldner, T., Wang, X., Werder, D. and Märkisch, B., *Limit on the Fierz Interference Term b from a Measurement of the Beta Asymmetry in Neutron Decay*, Phys. Rev. Lett., Vol. 125, pp. 112501, Sep 2020.
 - [12] de Shalit, A. and Talmi, I., Nuclear Shell Theory.
 - [13] Krane, K. S., Introductory Nuclear Physics, Wiley, New York, 1988.
 - [14] Severijns, N., Beck, M. and Naviliat-Cuncic, O., *Tests of the standard electroweak model in nuclear beta decay*, Rev. Mod. Phys., Vol. 78, pp. 991–1040, September 2006.
 - [15] Wong, S., Introductory Nuclear Physics, Prentice Hall Advanced Reference Series Prentice Hall Labora, Prentice Hall, 1990.

- [16] Jackson, J. D., Treiman, S. B. and Wyld, H. W., *Coulomb Corrections in Allowed Beta Transitions*, Nuclear Physics, Vol. 4, pp. 206–212, Nov. 1957.
- [17] Holstein, B. R., *Recoil effects in allowed beta decay: The elementary particle approach*, Reviews of Modern Physics, Vol. 46, No. 4, pp. 789–814, Oct. 1974.
- [18] Raab, E. L., Prentiss, M., Cable, A., Chu, S. and Pritchard, D. E., *Trapping of Neutral Sodium Atoms with Radiation Pressure*, Phys. Rev. Lett., Vol. 59, pp. 2631–2634, Dec 1987.
- [19] Corney, A., Atomic and Laser Spectroscopy, Oxford University Press, New York, 1977.
- [20] Gorelov, A., Behr, J., Melconian, D., Trinczek, M., Dubé, P., Häusser, O., Giesen, U., Jackson, K., Swanson, T., D'Auria, J., Dombsky, M., Ball, G., Buchmann, L., Jennings, B., Dilling, J., Schmid, J., Ashery, D., Deutsch, J., Alford, W., Asgeirsson, D., Wong, W. and Lee, B., *Beta-neutrino correlation experiments on laser trapped ^{38m}K , ^{37}K* , Hyperfine Interactions, Vol. 127, No. 1, pp. 373–380, 2000.
- [21] Swanson, T. B., Asgeirsson, D., Behr, J. A., Gorelov, A. and Melconian, D., *Efficient transfer in a double magneto-optical trap system*, J. Opt. Soc. Am. B, Vol. 15, No. 11, pp. 2641–2645, Nov 1998.
- [22] Fenker, B., Gorelov, A., Melconian, D., Behr, J. A., Anholm, M., Ashery, D., Behling, R. S., Cohen, I., Craiciu, I., Gwinner, G., McNeil, J., Mehlman, M., Olchanski, K., Shidling, P. D., Smale, S. and Warner, C. L., *Precision Measurement of the β Asymmetry in Spin-Polarized ^{37}K Decay*, Phys. Rev. Lett., Vol. 120, pp. 062502, Feb 2018.
- [23] Audi, G., Wapstra, A. and Thibault, C., *The AME2003 Atomic Mass Evaluation*, Nuclear Physics A, Vol. 729, No. 1, pp. 337 – 676, 2003.
- [24] Holstein, B. R., *Erratum: Recoil effects in allowed beta decay: The elementary particle approach*, Rev. Mod. Phys., Vol. 48, pp. 673–673, Oct 1976.
- [25] Severijns, N. and Naviliat-Cuncic, O., *Symmetry tests in nuclear beta decay*, Annual Review of Nuclear and Particle Science, Vol. 61, pp. 23–46, 2011.

- [26] Melconian, D. G., Measurement of the Neutrino Asymmetry in the Beta Decay of Laser-Cooled, Polarized ^{37}K , Ph.D. thesis, Simon Fraser University, 2005.

Appendix A

Notable Differences in Data Selection between this and the Previous Result

A.1 Polarization Cycle Selection

Data used for our recent PRL article was slightly less polarized than we thought it was, due to an oversight in the data selection procedure.

A.2 Leading Edge / Trailing Edge and Walk Correc- tion

Using the leading edge rather than the trailing edge to mark the timing of TDC pulses cleans up jitter, eliminates background, and changes the relative delays between different inputs. It is immediately relevant to the shape of the ‘walk correction’ on scintillator timing pulses, which give a different prediction for beta arrival time as a function of scintillator energy.

A.3 TOF Cut + Background Modelling

A SOE-beta time-of-flight cut is necessary to reduce background. The above mentioned walk correction directly results in an change in which specific events are selected in a given TOF cut. It further results in an adjustment to the expected

fraction of background events in any such cut.

A.4 BB1 Radius

Possibly my default radius cut on the DSSDs is a bit different. The region of the parameter space that I'm taking for the systematic uncertainty on this is definitely a bit different.

Appendix B

A PDF For The People

B.1 JTW

Here's a master equation from JTW to describe beta decay kinematics [5], [16]:

$$\begin{aligned} d^5\Gamma_{\text{JTW}} &\equiv \frac{F_\mp(Z, E_\beta)}{(2\pi)^5} p_\beta E_\beta (E_0 - E_\beta)^2 dE_\beta d^3\hat{\Omega}_\beta d^3\hat{\Omega}_\nu \\ &\times \xi \left[1 + a_{\beta\nu} \frac{\vec{p}_\beta \cdot \vec{p}_\nu}{E_\beta E_\nu} + b_{\text{Fierz}} \frac{m_e c^2}{E_\beta} + c_{\text{align}} T_{\text{align}}(\vec{J}) \left(\frac{\vec{p}_\beta \cdot \vec{p}_\nu}{3E_\beta E_\nu} - \frac{(\vec{p}_\beta \cdot \hat{\vec{j}})(\vec{p}_\nu \cdot \hat{\vec{j}})}{E_\beta E_\nu} \right) \right. \\ &\left. + \frac{\vec{J}}{J} \cdot \left(A_\beta \frac{\vec{p}_\beta}{E_\beta} + B_\nu \frac{\vec{p}_\nu}{E_\nu} + D_{\text{TR}} \frac{\vec{p}_\beta \times \vec{p}_\nu}{E_\beta E_\nu} \right) \right] \end{aligned} \quad (\text{B.1})$$

where, for convenience, we have defined a nuclear alignment term,

$$T_{\text{align}}(\vec{J}) \equiv \frac{J(J+1) - 3\langle(\vec{J} \cdot \hat{\vec{j}})^2\rangle}{J(2J-1)}. \quad (\text{B.2})$$

Note that this master equation depends on neutrino momentum, which we cannot observe directly. Furthermore, we cannot reconstruct neutrino momenta in our decay events either, because it would be necessary to account for the momentum of the recoiling daughter nucleus, treating the decay as a three-body problem. From an experimental standpoint, we failed to measure the momenta of the daughters in conjunction with the “tagged” beta decay events with which we are primarily con-

cerned in this thesis. From a theoretical standpoint, JTW has intentionally neglected recoil-order terms – meaning that the daughter nucleus is treated, for the purpose of kinetic energy calculations, as being infinitely massive, and as such it must have no change in kinetic energy from the decay. This approximation makes it a bit tricky to correctly re-formulate Eq. (B.1) in terms of the momentum of the daughter instead of the momentum of the neutrino.

Fortunately, it is possible to simplify Eq. (B.1) by integrating over all possible neutrino directions, such that the result no longer depends on parameters that we do not observe. The neutrino energy itself is not a free variable in this equation, because the energy release in the decay is fixed, and given the approximation that none of that energy is allocated to the recoiling daughter, it is very straightforward to calculate the neutrino energy for a decay event in which the beta energy is known.

The result of performing this integration over neutrino direction is:

$$\begin{aligned} d^3\Gamma dE_\beta d^3\hat{\Omega}_\beta &= \frac{2}{(2\pi)^4} F_\mp(Z, E_\beta) p_\beta E_\beta (E_0 - E_\beta)^2 dE_\beta d^3\hat{\Omega}_\beta \xi \\ &\times \left[1 + b_{\text{Fierz}} \frac{m_e c^2}{E_\beta} + A_\beta \left(\frac{\vec{J}}{J} \cdot \frac{\vec{p}_\beta}{E_\beta} \right) \right], \end{aligned} \quad (\text{B.3})$$

which is a great simplification on Eq. (B.1). We still must write the remaining parameters in terms of the relevant nuclear matrix elements and fundamental coupling constants. These coupling constants are, in general, complex-valued, and JTW does not choose a phase angle for us. We write them out in Eqs. (B.4-B.6).

$$\begin{aligned} \xi &= |M_F|^2 (|C_S|^2 + |C_V|^2 + |C'_S|^2 + |C'_V|^2) \\ &+ |M_{GT}|^2 (|C_T|^2 + |C_A|^2 + |C'_T|^2 + |C'_A|^2) \end{aligned} \quad (\text{B.4})$$

$$b_{\text{Fierz}} \xi = \pm 2\gamma \text{Re}[|M_F|^2 (C_S C_V^* + C'_S C_V'^*) + |M_{GT}|^2 (C_T C_A^* + C'_T C_A'^*)] \quad (\text{B.5})$$

$$\begin{aligned} A_\beta \xi &= |M_{GT}|^2 \lambda_{J'J} \left[\pm 2\text{Re}[C_T C_T'^* - C_A C_A'^*] + 2 \frac{\alpha Z m_e}{p_\beta} \text{Im}[C_T C_A'^* + C'_T C_A^*] \right] \\ &+ \delta_{J'J} M_F M_{GT} \left(\frac{J}{J+1} \right)^{1/2} \left[2 \text{Re}[C_S C_T^* + C'_S C_T'^* - C_V C_A^* - C'_V C_A'^*] \right. \\ &\left. \pm 2 \frac{\alpha Z m_e}{p_\beta} \text{Im}[C_S C_A'^* + C'_S C_A^* - C_V C_T'^* - C'_V C_T^*] \right] \end{aligned} \quad (\text{B.6})$$

Note that JTW presents slightly different expressions for the sign convention in

components of A_β within [5] and [16]. Here, we adopt the convention from the latter publication. Furthermore, we do not require that either M_F or M_{GT} be positive (which would allow us to safely drop their absolute value indicators and make the conventions of these two papers equivalent). In order to obtain the correct, physically observed value for A_β , we require that the $M_F M_{GT}$ term in Eq. (B.6) have an overall positive value. Because we know that the scalar and tensor couplings must be small, and any imaginary contributions to the term must be small, we conclude that

$$M_F M_{GT} (C_V C_A'^* + C_V' C_A^*) < 0. \quad (\text{B.7})$$

B.2 Holstein

Holstein [17] [24] generously provides explicit equations to match both Eq. (B.1) (i.e. Holstein's Eq. (51), where neutrino direction is a parameter of the probability distribution) and Eq. (B.3) (Holstein's Eq. (52), where neutrino direction has already been integrated over).

Here's Holstein's Eq. (52):

$$\begin{aligned} d^3\Gamma_{\text{Holstein}} = & 2G_v^2 \cos^2 \theta_c \frac{F_\mp(Z, E_\beta)}{(2\pi)^4} p_\beta E_\beta (E_0 - E_\beta)^2 dE_\beta d^3\hat{\Omega}_\beta \\ & \times \left\{ F_0(E_\beta) + \Lambda_1 F_1(E_\beta) \hat{\mathbf{n}} \cdot \frac{\vec{p}_\beta}{E_\beta} + \Lambda_2 F_2(E_\beta) \left[\left(\hat{\mathbf{n}} \cdot \frac{\vec{p}_\beta}{E_\beta} \right)^2 - \frac{1}{3} \frac{p_\beta^2}{E_\beta^2} \right] \right. \\ & \left. + \Lambda_3 F_3(E_\beta) \left[\left(\hat{\mathbf{n}} \cdot \frac{\vec{p}_\beta}{E_\beta} \right)^3 - \frac{3}{5} \frac{p_\beta^2}{E_\beta^2} \hat{\mathbf{n}} \cdot \frac{\vec{p}_\beta}{E_\beta} \right] \right\} \end{aligned} \quad (\text{B.8})$$

A careful reader will eventually note that Holstein's spectral functions $F_i(E_\beta)$ are not the same as the $F_i(E_\beta, u, v, s)$ in any limit, despite the notational similarities. Among other rules, Holstein's spectral functions obey these:

$$F_i(E_\beta) \neq F_i(E_\beta, u, v, s) \quad (\text{B.9})$$

$$F_i(E_\beta) = H_i(E_\beta, u, v, 0) \quad (\text{B.10})$$

$$f_i(E_\beta) = F_i(E_\beta, u, v, 0). \quad (\text{B.11})$$

For the $F_i(E_\beta)$ functions of interest to us here, we find the following relationships:

$$\begin{aligned}
F_0(E_\beta) &= H_0(E_\beta, J, J', 0) = F_1(E_\beta, J, J', 0) &= f_1(E_\beta) \\
F_1(E_\beta) &= H_1(E_\beta, J, J', 0) = F_4(E_\beta, J, J', 0) + \frac{1}{3}F_7(E_\beta, J, J', 0) &= f_4(E_\beta) + \frac{1}{3}f_7(E_\beta) \\
F_2(E_\beta) &= H_2(E_\beta, J, J', 0) = F_{10}(E_\beta, J, J', 0) + \frac{1}{2}F_{13}(E_\beta, J, J', 0) &= f_{10}(E_\beta) + \frac{1}{3}f_{13}(E_\beta) \\
F_3(E_\beta) &= H_3(E_\beta, J, J', 0) = F_{18}(E_\beta, J, J', 0) &= f_{18}(E_\beta). \quad (\text{B.12})
\end{aligned}$$

Note that the $f_i(E_\beta)$ in Eq. B.12 are the same spectral functions used to describe a polarized decay spectrum when the neutrino (ie, the recoil) is also observed – though of course such a spectrum must have other terms as well. For the spectrum of interest to us here, in which the neutrino direction has already been integrated over, we can simply look up the $H_i(E_\beta, J, J', 0) = H_i(E, u, v, s=0)$ spectral functions, and leave it at that. We find:

$$\begin{aligned}
F_0(E_\beta) &= |a_1|^2 + 2 \operatorname{Re}[a_1^* a_2] \frac{1}{3M^2} \left[m_e^2 + 4E_\beta E_0 + 2 \frac{m_e^2}{E_\beta} E_0 - 4E_\beta^2 \right] \\
&\quad + |c_1|^2 + 2 \operatorname{Re}[c_1^* c_2] \frac{1}{9M^2} \left[11m_e^2 + 20E_\beta E_0 - 2 \frac{m_e^2}{E_\beta} E_0 - 20E_\beta^2 \right] \\
&\quad - 2 \frac{E_0}{3M} \operatorname{Re}[c_1^*(c_1 + d \pm b)] + \frac{2E_\beta}{3M} (3|a_1|^2 + \operatorname{Re}[c_1^*(5c_1 \pm 2b)]) \\
&\quad - \frac{m_e^2}{3ME_\beta} \operatorname{Re} \left[-3a_1^* e + c_1^* \left(2c_1 + d \pm 2b - h \frac{E_0 - E_\beta}{2M} \right) \right] \quad (\text{B.13})
\end{aligned}$$

$$\begin{aligned}
F_1(E_\beta) &= \delta_{u,v} \left(\frac{u}{u+1} \right)^{1/2} \left\{ 2 \operatorname{Re} \left[a_1^* \left(c_1 - \frac{E_0}{3M} (c_1 + d \pm b) + \frac{E_\beta}{3M} (7c_1 \pm b + d) \right) \right] \right. \\
&\quad \left. + 2 \operatorname{Re}[a_1^* c_2 + c_1^* a_2] \left(\frac{4E_\beta(E_0 - E_\beta) + 3m_e^2}{3M^2} \right) \right\} \\
&\mp \frac{(-1)^s \gamma_{u,v}}{u+1} \operatorname{Re} \left\{ c_1^* \left(c_1 + 2c_2 \left(\frac{8E_\beta(E_0 - E_\beta) + 3m_e^2}{3M^2} \right) - \frac{2E_0}{3M} (c_1 + d \pm b) \right. \right. \\
&\quad \left. \left. + \frac{E_\beta}{3M} (11c_1 - d \pm 5b) \right) \right\} + \frac{\lambda_{u,v}}{u+1} \operatorname{Re} \left\{ c_1^* \left[-f \left(\frac{5E_\beta}{M} \right) \right. \right. \\
&\quad \left. \left. + g \left(\frac{3}{2} \right)^{1/2} \left(\frac{E_0^2 - 11E_0E_\beta + 6m_e^2 + 4E_\beta^2}{6M^2} \right) \pm 3j_2 \left(\frac{8E_\beta^2 - 5E_0E_\beta - 3m_e^2}{6M^2} \right) \right] \right\} \quad (\text{B.14})
\end{aligned}$$

$$\begin{aligned}
F_2(E_\beta) = & \theta_{u,v} \frac{E_\beta}{2M} \operatorname{Re} \left[c_1^* \left(c_1 + c_2 \frac{8(E_0 - E_\beta)}{3M} - d \pm b \right) \right] \\
& - \delta_{u,v} \frac{E_\beta}{M} \left[\frac{u(u+1)}{(2u-1)(2u+3)} \right]^{1/2} \operatorname{Re} \left\{ a_1^* \left(\left(\frac{3}{2} \right)^{1/2} f + g \frac{E_\beta + 2E_0}{4M} \right. \right. \\
& \left. \left. \pm \left(\frac{3}{2} \right)^{1/2} j_2 \frac{E_0 - E_\beta}{2M} \right) \right\} + (-1)^s \kappa_{u,v} \frac{E_\beta}{2M} \operatorname{Re} \left[c_1^* \left(\pm 3f \pm \left(\frac{3}{2} \right)^{1/2} g \frac{E_0 - E_\beta}{M} \right. \right. \\
& \left. \left. + 3j_2 \frac{E_0 - 2E_\beta}{2M} \right) \right] + \epsilon_{u,v} \operatorname{Re}[c_1^* j_3] \left(\frac{21E_\beta^2}{8M^2} \right)
\end{aligned} \tag{B.15}$$

$$\begin{aligned}
F_3(E_\beta) = & -\delta_{u,v} (3u^2 + 3u - 1) \left[\frac{u}{(u-1)(u+1)(u+2)(2u-1)(2u+3)} \right]^{1/2} \\
& \times \operatorname{Re}[a_1^* j_3] \left(\frac{E_\beta^2 \sqrt{15}}{4M^2} \right) + \frac{\rho_{u,v}}{u+1} \operatorname{Re} \left[c_1^* (g\sqrt{3} + j_2\sqrt{2}) \left(\frac{5E_\beta^2}{4M^2} \right) \right] \\
& \pm \frac{(-1)^s \sigma_{u,v}}{u+1} \operatorname{Re}[c_1^* j_3] \left(\frac{5E_\beta^2}{2M^2} \right)
\end{aligned} \tag{B.16}$$

and we might really appreciate if these things could be simplified a bit.

The terms $a_1, a_2, b, c_1, c_2, d, e, f, g, h, j_2, j_3$ are “structure functions”. Holstein gives some predictions for their form, assuming the impulse approximation holds, in his Eq. (67). For the most part, the values and form of these structure functions are beyond the scope of this thesis, so I will not re-write them all here. It should be noted that the numerical values used for these parameters came from a private communication from Ian Towner to the collaboration. However, it is important to note the expressions for a_i and c_i , because these will directly come into play when we try to reconcile Holstein’s expression with JTW’s. Therefore,

$$a(q^2) \approx \frac{g_V(q^2)}{\left(1 + \frac{\Delta}{2M}\right)} \left[M_F + \frac{1}{6}(q^2 - \Delta^2)M_{r^2} + \frac{1}{3}\Delta M_{\mathbf{r} \cdot \mathbf{p}} \right] \tag{B.17}$$

$$\begin{aligned}
c(q^2) \approx & \frac{g_A(q^2)}{\left(1 + \frac{\Delta}{2M}\right)} \left[M_{GT} + \frac{1}{6}(q^2 - \Delta^2)M_{\sigma r^2} + \frac{1}{6\sqrt{10}}(2\Delta^2 + q^2)M_{1y} \right. \\
& \left. + A \frac{\Delta}{2M} M_{\sigma L} + \frac{1}{2}\Delta M_{\sigma rp} \right]
\end{aligned} \tag{B.18}$$

...where the M_{xxx} ’s are certain nuclear matrix elements. However, Eqs. (B.13-B.16) are not written in terms of $a(q^2)$ and $c(q^2)$, but rather in terms of a_1, a_2, c_1 , and c_2 .

In fact, Holstein is implicitly using series expansions to remove the dependence on recoil momentum, so that

$$a(q^2) = a_1 + \left(\frac{q^2}{M^2}\right) a_2 + \dots \quad (\text{B.19})$$

$$c(q^2) = c_1 + \left(\frac{q^2}{M^2}\right) c_2 + \dots \quad (\text{B.20})$$

Next, Holstein goes and tweaks those $F_i(E_\beta)$ terms that we've already written out, by adding in an adjustment for Coulomb corrections. Those corrections have this form:

$$F_i(E_\beta) \rightarrow \tilde{F}_i(E_\beta) := F_\mp(Z, E_\beta) [F_i(E_\beta) + \Delta F_i(E_\beta)] \quad (\text{B.21})$$

To obtain expressions for the $\Delta F_i(E_\beta)$, Holstein invokes some Feynman diagrams and provides expressions for several integrals, all of which are both complex and complicated. The modified spectral functions are provided in terms of functions of these integrals. Since nobody wants to have to evaluate those integrals, Holstein makes a further approximation by taking only the first term in an expansion of the $\Delta F_i(E_\beta)$ in terms of $Z\alpha$, where $Z\alpha \ll 1$. Then, the resulting expressions for $\Delta F_i(E_\beta)$ can be written in terms of much more straightforward integrals over form factors for electric charge and weak charge.

If we make the further assumption that these form factors are identical, and that both types of charge are spread over a ball of uniform density with radius R , then we find:

$$X = Y = \frac{9\pi R}{140} \quad (\text{B.22})$$

in the Eqs. (B.23 - B.25) that follow.

Because Holstein doesn't actually write this stuff out in terms of $F_i(E_\beta)$, but rather in terms of $F_i(E_\beta, u, v, s)$, this correction presents yet another opportunity for the reader to interpret his notation incorrectly. We note that one must remember to make use of the relations in Eq. (B.12). Furthermore, Holstein notes that some of the terms $F_i(E_\beta, u, v, s)$ are suppressed already, and he does not consider those terms further. We will take this approximation to be adequate for our purposes here.

So, we'll write out the functions for these corrections.

$$\begin{aligned}\Delta F_1(E_\beta, u, v, s) = & \mp \left(\frac{8\alpha Z}{3\pi} \right) X \left[E_\beta \left(8|a|^2 + \frac{28}{3}|c|^2 \right) + E_0 \left(|a|^2 - \frac{1}{3}|c|^2 \right) \right. \\ & \left. + 3 \left(\frac{m_e c^2}{E_\beta} \right) (|a|^2 + |c|^2) \right]\end{aligned}\quad (\text{B.23})$$

$$\Delta F_4(E_\beta, u, v, s) = \mp \left(\frac{8\alpha Z}{3\pi} \right) 9XE_\beta \left[2\delta_{u,v} \left(\frac{u}{u+1} \right)^{1/2} \text{Re}[a^*c] \mp (-1)^s \left(\frac{\gamma_{u,v}}{u+1} \right) |c|^2 \right]\quad (\text{B.24})$$

$$\begin{aligned}\Delta F_7(E_\beta, u, v, s) = & \mp \left(\frac{8\alpha Z}{3\pi} \right) X (E_0 - E_\beta) \left[2\delta_{u,v} \left(\frac{u}{u+1} \right)^{1/2} \text{Re}[a^*c] \right. \\ & \left. \mp (-1)^s \left(\frac{\gamma_{u,v}}{u+1} \right) |c|^2 \right]\end{aligned}\quad (\text{B.25})$$

We note that the above corrections have been written in terms of $a(q^2)$ and $c(q^2)$, and we must use Eqs. (B.19, B.20) to put the results in terms of a_1 , a_2 , c_1 , and c_2 so that they can be correctly combined with Eqs. (B.13-B.16).

If we evaluate Holstein's Eqs. (B8), which I will absolutely not type out here, for the case $u = v = J = J' = 3/2$, we find the following values:

$$\begin{aligned}\delta_{u,v} &= 1 & \theta_{u,v} &= 1 & \rho_{u,v} &= \frac{-41}{40} \\ \gamma_{u,v} &= 1 & \kappa_{u,v} &= \frac{1}{2\sqrt{2}} & \sigma_{u,v} &= \frac{-41}{4\sqrt{35}} \\ \lambda_{u,v} &= \frac{-\sqrt{2}}{5} & \epsilon_{u,v} &= \frac{-1}{2\sqrt{5}} & \phi_{u,v} &= 0\end{aligned}\quad (\text{B.26})$$

Furthermore, in our calculations here, we will be considering only the β^+ decay modes, and therefore we take the *lower* sign when the option arises. We also will use $s = 0$, so that $(-1)^s = +1$.

- - - - -

Let's define some of that notation! Firstly,

$$\text{Holstein's } \hat{n} = \text{JTW's } \mathbf{j}, \quad (\text{B.27})$$

and the Λ_i are given by Holstein's Eq. (48):

$$\Lambda_1 := \frac{\langle M \rangle}{J} \quad (\text{B.28})$$

$$\Lambda_2 := 1 - \frac{3\langle M^2 \rangle}{J(J+1)} \quad (\text{B.29})$$

$$\Lambda_3 := \frac{\langle M \rangle}{J} - \frac{5\langle M^3 \rangle}{J(3J^2 + 3J - 1)}. \quad (\text{B.30})$$

We immediately see that Holstein's Λ_1 is closely related to JTW's $\frac{\vec{J}}{J}$, and a bit later after John points it out to us, we see that Holstein's Λ_2 is closely related to JTW's T_{align} . JTW doesn't have any equivalent to Λ_3 . In particular, we find:

$$\Lambda_1 \hat{\mathbf{j}} = \frac{\langle M \rangle}{J} \hat{\mathbf{j}} = \frac{\vec{J}}{J} \quad (\text{B.31})$$

$$\Lambda_2 = T_{\text{align}} \frac{(2J-1)}{(J+1)}. \quad (\text{B.32})$$

Appendix C

Comparing Notation between Holstein and JTW

C.1 Comparison Guide

This is a short guide to differences in notation, sign convention, and normalization. There are several tables here, chosen to aid in conversion between the two conventions. This section also includes handwritten notes.

C.2 Imported from Another Appendix

Here are some equations. I want to keep these somewhere in this chapter. For the equations below, I am intentionally not including the ROC terms. We take only enough Holstein terms to construct the expressions JTW gives us.

$$\xi = G_v^2 \cos \theta_C f_1(E) \quad (C.1)$$

$$a_{\beta\nu} = f_2(E) / f_1(E) \quad (C.2)$$

$$\frac{\langle \vec{J} \rangle}{J} \cdot \frac{\vec{p}}{E} A_\beta = \Lambda_1 \hat{n} \cdot \frac{\vec{p}}{E} f_4(E) / f_1(E) \quad (C.3)$$

$$\frac{\langle \vec{J} \rangle}{J} \cdot \frac{\vec{p}_\nu}{E_\nu} B_\nu = \Lambda_1 \hat{n} \cdot \vec{k} f_6(E) / f_1(E) \quad (C.4)$$

$$\frac{\langle \vec{J} \rangle}{J} \cdot \frac{(\vec{p} \times \vec{p}_\nu)}{EE_\nu} D_{\text{TR}} = \Lambda_1 \hat{n} \cdot \left(\frac{\vec{p}}{E} \times \hat{k} \right) f_8(E) / f_1(E) \quad (C.5)$$

Holstein	JTW	Thesis	Comments
k			Neutrino momentum 4-vector
	E_ν		Neutrino energy
\hat{k}	$\frac{\mathbf{p}_\nu}{E_\nu}$		3D Neutrino emission direction unit vector. Neutrinos are always treated as massless.
p			Beta momentum 4-vector, or sometimes the magnitude of the beta momentum 3-vector. Never the magnitude of the 4-vector.
E	E_e	E_β	Beta energy
\mathbf{p}	\mathbf{p}_e	\vec{p}_β	Beta momentum 3-vector
q			Recoil momentum 4-vector, or sometimes a magnitude.

Table C.1: A comparison of some kinematic terms in JTW [5] [16] and Holstein [17]. Yes, the bolding/italicization carries meaning.

Holstein	JTW	Comments
u	J	Initial state total nuclear angular momentum.
v	J'	Final state total nuclear angular momentum.
s	No equivalent?	Umm... I should check on this.

Table C.2: A comparison of some angular momenta in JTW [5] [16] and Holstein [17].

$$\begin{aligned}
 & \left[\frac{J(J+1) - 3\langle(\vec{J} \cdot \hat{j})^2\rangle}{J(2J-1)} \right] \left[\frac{1}{3} \frac{\vec{p} \cdot \vec{p}_\nu}{EE_\nu} - \frac{(\vec{p} \cdot \hat{j})(\vec{p}_\nu \cdot \hat{j})}{EE_\nu} \right] c_{\text{align}} \\
 &= \Lambda_2 \left[(\hat{n} \cdot \frac{\vec{p}}{E})(\hat{n} \cdot \hat{k}) - \frac{1}{3} (\frac{\vec{p}}{E} \cdot \hat{k}) \right] f_{12}(E) / f_1(E) \tag{C.6}
 \end{aligned}$$

Holstein	JTW	Thesis	Comments
$G_v^2 \cos \theta_C f_1(E)$	ξ	$\xi(E_\beta)$	Normalization. Proportional to the fractional decay rate.
\hat{n}	\mathbf{j}	$\hat{\mathbf{j}}$	Nuclear polarization unit vector. Also the axis of quantization.
J	J		Total nuclear angular momentum quantum number
$\langle M \rangle$	$ \langle \mathbf{J} \rangle $		Angular momentum projection along the axis of quantization
$\Lambda^{(1)} \hat{n} = \frac{\langle M \rangle}{J} \hat{n}$	$\frac{\langle \mathbf{J} \rangle}{J}$	$\Lambda_1 \hat{\mathbf{n}}$	Dipole element vector. Proportional to nuclear polarization. (Rephrase this.)
$\Lambda^{(1)} = \frac{\langle M \rangle}{J}$...	Λ_1	...
$\Lambda^{(2)}$	$\frac{J(J+1)-3\langle(\vec{\mathbf{J}} \cdot \hat{\mathbf{j}})^2\rangle}{J(2J-1)} \frac{(2J-1)}{(J+1)}$	$T_{\text{align}}(\vec{\mathbf{J}}) \frac{(2J-1)}{(J+1)}$	Quadrupole element
$\Lambda^{(3)}$	No equivalent	Λ_3	Octopole element
$\Lambda^{(4)}$	No equivalent	Λ_4	Hexadecapole element

Table C.3: A comparison of the multipole elements and their normalizations (and some other stuff) in JTW [5] [16] and Holstein [17].

Term	Integral
$f_1(E_\beta)$	$\leftrightarrow \int 1 d\hat{\Omega}_k = 4\pi$
$f_2(E_\beta)$	$\leftrightarrow \int \left(\frac{\vec{p}_\beta \cdot \hat{k}}{E_\beta} \right) d\hat{\Omega}_k = 0$
$f_3(E_\beta)$	$\leftrightarrow \int \left(\left(\frac{\vec{p}_\beta \cdot \hat{k}}{E_\beta} \right)^2 - \frac{1}{3} \frac{p_\beta^2}{E_\beta^2} \right) d\hat{\Omega}_k = 0$
$f_4(E_\beta)$	$\leftrightarrow \int \left(\hat{n} \cdot \frac{\vec{p}_\beta}{E_\beta} \right) d\hat{\Omega}_k = 4\pi \left(\hat{n} \cdot \frac{\vec{p}_\beta}{E_\beta} \right)$
$f_5(E_\beta)$	$\leftrightarrow \int \left(\hat{n} \cdot \frac{\vec{p}_\beta}{E_\beta} \right) \left(\frac{\vec{p}_\beta \cdot \hat{k}}{E_\beta} \right) d\hat{\Omega}_k = 0$
$f_6(E_\beta)$	$\leftrightarrow \int \left(\hat{n} \cdot \hat{k} \right) d\hat{\Omega}_k = 0$
$f_7(E_\beta)$	$\leftrightarrow \int \left(\hat{n} \cdot \hat{k} \right) \left(\frac{\vec{p}_\beta \cdot \hat{k}}{E_\beta} \right) d\hat{\Omega}_k = \frac{1}{3} 4\pi \left(\hat{n} \cdot \frac{\vec{p}_\beta}{E_\beta} \right)$
$f_8(E_\beta)$	$\leftrightarrow \int \hat{n} \cdot \left(\frac{\vec{p}_\beta \times \hat{k}}{E_\beta} \right) d\hat{\Omega}_k = 0$
$f_9(E_\beta)$	$\leftrightarrow \int \hat{n} \cdot \left(\frac{\vec{p}_\beta \times \hat{k}}{E_\beta} \right) \left(\frac{\vec{p}_\beta \cdot \hat{k}}{E_\beta} \right) d\hat{\Omega}_k = 0$
$f_{10}(E_\beta)$	$\leftrightarrow \int T_2(\hat{n}) : \left[\frac{\vec{p}_\beta}{E}, \frac{\vec{p}_\beta}{E} \right] d\hat{\Omega}_k = 4\pi T_2(\hat{n}) : \left[\frac{\vec{p}_\beta}{E}, \frac{\vec{p}_\beta}{E} \right]$
$f_{11}(E_\beta)$	$\leftrightarrow \int T_2(\hat{n}) : \left[\frac{\vec{p}_\beta}{E}, \frac{\vec{p}_\beta}{E} \right] \left(\frac{\vec{p}_\beta \cdot \hat{k}}{E} \right) d\hat{\Omega}_k = 0$
$f_{12}(E_\beta)$	$\leftrightarrow \int T_2(\hat{n}) : \left[\frac{\vec{p}_\beta}{E}, \hat{k} \right] d\hat{\Omega}_k = 0$
$f_{13}(E_\beta)$	$\leftrightarrow \int T_2(\hat{n}) : \left[\frac{\vec{p}_\beta}{E}, \hat{k} \right] \left(\frac{\vec{p}_\beta \cdot \hat{k}}{E} \right) d\hat{\Omega}_k = \frac{1}{3} 4\pi T_2(\hat{n}) : \left[\frac{\vec{p}_\beta}{E}, \frac{\vec{p}_\beta}{E} \right]$
$f_{14}(E_\beta)$	$\leftrightarrow \int T_2(\hat{n}) : \left[\hat{k}, \hat{k} \right] d\hat{\Omega}_k = 0$
$f_{15}(E_\beta)$	$\leftrightarrow \int T_2(\hat{n}) : \left[\hat{k}, \hat{k} \right] \left(\frac{\vec{p}_\beta \cdot \hat{k}}{E} \right) d\hat{\Omega}_k = 0$
$f_{16}(E_\beta)$	$\leftrightarrow \int T_2(\hat{n}) : \left[\frac{\vec{p}_\beta}{E}, \frac{\vec{p}_\beta}{E} \times \hat{k} \right] d\hat{\Omega}_k = 0$
$f_{17}(E_\beta)$	$\leftrightarrow \int T_2(\hat{n}) : \left[\hat{k}, \frac{\vec{p}_\beta}{E} \times \hat{k} \right] d\hat{\Omega}_k = 0$
$f_{18}(E_\beta)$	$\leftrightarrow \int T_3(\hat{n}) : \left[\frac{\vec{p}_\beta}{E}, \frac{\vec{p}_\beta}{E}, \frac{\vec{p}_\beta}{E} \right] d\hat{\Omega}_k = 4\pi T_3(\hat{n}) : \left[\frac{\vec{p}_\beta}{E}, \frac{\vec{p}_\beta}{E}, \frac{\vec{p}_\beta}{E} \right]$

Table C.4: Integrals of terms from Holstein's Eq. (51) [17].

$C_A = C'_A$; $C_V = \pm \frac{1}{\sqrt{2}} M_{GT} (C_A + C'_A)$ ← prefer ⊕
 $C_V = C'_V$; $a_1 = \pm \frac{1}{\sqrt{2}} M_F (C_V + C'_V)$ ← depends on above sign.

In our code:
 $M_F = 1.0$
 $M_{GT} = -0.62376$

Also in our Code:
 $g_V = 1.00$
 $g_A = 0.91210$

* in Holstein itself, sometimes g_A and g_V show up without their associated M_{GT} and M_F .

* Really, the conversion above doesn't include the extra terms in a_1 and C_V that couple to nuclear elements other than M_F and M_{GT} .

I think the point is that I should actually interpret:

$g_V = \pm \frac{1}{\sqrt{2}} (C_V + C'_V) = 1.0 \rightarrow a_1 = g_V M_F \Rightarrow C_V = C'_V = \frac{1}{\sqrt{2}}$
 $g_A = \pm \frac{1}{\sqrt{2}} (C_A + C'_A) \approx 0.91210 \rightarrow C_A = g_A M_{GT} \Rightarrow C_A = C'_A = \frac{-0.91210}{\sqrt{2}} \approx -0.644952$

* Check: with $C_A = C'_A$ and $C_V = C'_V$, does JTW give the right A_β ?

~~$A_\beta = 0.763683; A_\beta = 0.496903 \rightarrow A_\beta = \pm 0.375394$ (Bad!)~~

$A_\beta = 0.763671 \leftarrow$ Allow M_{GT} and M_F to have opposite signs. (Bad!)
 $A_\beta = -0.568045 \leftarrow$ enforce $\oplus M_{GT}$. Or earlier JTW "convention".
 * Because Holstein insists on his own sign convention, we get $M_{GT-Holstein} = -M_{GT-JTW}$

Figure C.1: "Notes 0"

In our code:

$$\boxed{\begin{array}{l} M_F = 1.0 \quad ; \quad g_V = 1.0 \quad \rightarrow \quad g_V M_F = 1.0 \\ M_{GT} = -0.62376 \quad ; \quad g_A = 0.91210 \quad \rightarrow \quad g_A M_{GT} = -0.568931 \end{array}} \Rightarrow p \equiv \frac{g_A M_{GT}}{g_V M_F}$$

$p \approx -0.568931$
Holstein

* If we require that $C_A, C_A', C_V, C_V', M_F, M_{GT}$ are all real, and enforce that these can all take values which allow for Holstein and JTW to be equivalent in some limits, we require:

$$\begin{array}{lll} \text{JTW} & \text{Holstein} & \text{Holstein} \quad \text{JTW} \\ \xi = f_1(E) & \rightarrow |a_1|^2 = |M_F|^2 (|C_V|^2 + |C_V'|^2) \\ A \cdot \xi = f_4(E) & \quad \quad |C_1|^2 = |M_{GT}|^2 (|C_A|^2 + |C_A'|^2) \\ \downarrow & \downarrow & \downarrow \\ \rightarrow |q|^2 = 2|M_{GT}|^2 \cdot \text{Re}[C_A C_A'^*] \end{array}$$

$$\begin{aligned} \text{Re}[q^* C_1] &= -\text{Re}[M_F M_{GT} (C_V C_A'^* + C_V' C_A)] && \leftarrow \text{later} \\ \text{Re}[q^* C_1] &= -\text{Re}[|M_F||M_{GT}|(C_V C_A'^* + C_V' C_A)] && \leftarrow \text{earlier.} \end{aligned}$$

The Results:

$$\begin{array}{ll} \text{Holstein} & \text{JTW} \\ C_V = C_V' & a_1 = \pm \frac{1}{\sqrt{2}} M_F (C_V + C_V') = \pm M_F (\sqrt{2}) (C_V) \\ C_A = C_A' & C_1 = \pm \frac{1}{\sqrt{2}} M_{GT} (C_A + C_A') = \pm M_{GT} (\sqrt{2}) (C_A) \end{array}$$

$$a_1 \approx g_V M_{F,H};$$

$$C_1 \approx g_A M_{GT,H};$$

~~Holstein~~

$$\boxed{M_{GT, \text{Holstein}} = -M_{GT, \text{JTW}}}$$

which sign?!

$$a_1 \approx g_V M_F; \quad g_V = \pm \frac{1}{\sqrt{2}} (C_V + C_V') = 1.0; \quad M_F = 1.0 \quad ; \quad C_V = C_V'$$

$$C_1 \approx g_A M_{GT}; \quad g_A = \pm \frac{1}{\sqrt{2}} (C_A + C_A') \approx 0.91210; \quad M_{GT} = -0.62376; \quad C_A = C_A'$$

$\uparrow \uparrow$
JTW terms

Figure C.2: "Notes 1"

$$\begin{aligned}
b \cdot \bar{z} &= \pm 2\gamma \operatorname{Re} \left[|M_F|^2 (C_S C_V^* + C'_S C_V'^*) + |M_{GT}|^2 (C_T C_A^* + C'_T C_A'^*) \right] \\
&= -2\gamma \left[|M_F|^2 (C_S C_V^* + C'_S C_V'^*) + |M_{GT}|^2 (C_T C_A^* + C'_T C_A'^*) \right] \\
&= -2\gamma |M_F|^2 (C_S + C'_S) C_V^* + -2\gamma |M_{GT}|^2 (C_T + C'_T) C_A^* \\
&= -2\gamma |M_F|^2 \cdot \frac{1}{\sqrt{2}} g_V \underbrace{(C_S + C'_S)}_{+\sqrt{2} g_S} + -2\gamma |M_{GT}|^2 \underbrace{\left(\frac{-1}{\sqrt{2}}\right)}_{-\sqrt{2} g_T} g_A \underbrace{(C_T + C'_T)}_{-\sqrt{2} g_T} \\
&= -2\gamma |M_F|^2 \cdot g_V \cdot g_S - 2\gamma |M_{GT}|^2 \cdot g_A \cdot g_T \\
\underline{b \cdot \bar{z}} &= -2\gamma \left[|M_F|^2 g_V g_S + |M_{GT}|^2 g_A g_T \right]
\end{aligned}$$

~~REMARK~~ $\gamma = (1 - \alpha^2 z^2)^{1/2}$

Figure C.3: "Notes 2"

To Match Up Holstein and JT W:

$$g_V = \frac{1}{\sqrt{2}}(C_V + C'_V) ; \quad C_V = C'_V = \frac{1}{\sqrt{2}}g_V = \frac{1}{\sqrt{2}}$$

$$M_F = 1.0 \quad a_1 \approx g_V M_F$$

$$g_A = \frac{-1}{\sqrt{2}}(C_A + C'_A) ; \quad C_A = C'_A = \frac{-1}{\sqrt{2}}g_A \approx \frac{-1}{\sqrt{2}}(0.91210) \quad c_1 \approx g_A M_{GT}$$

$$M_{GT} = -0.62376$$

Also define:

$$g_\phi \equiv \frac{1}{\sqrt{2}}(C_\phi + C'_\phi) ; \quad C_\phi = C'_\phi = \frac{1}{\sqrt{2}}g_\phi \approx 0$$

$$= \frac{1}{\sqrt{2}}C_\phi$$

$$g_T \equiv \frac{-1}{\sqrt{2}}(C_T + C'_T) ; \quad C_T = C'_T = \frac{-1}{\sqrt{2}}g_T \approx 0$$

$$= \frac{-1}{\sqrt{2}}C_T$$

Then, we find:

$$\ddot{\zeta} = |M_F|^2(g_V^2 + g_\phi^2) + |M_{GT}|^2(g_A^2 + g_T^2)$$

$$A_p \ddot{\zeta} = \frac{2}{5}|M_{GT}|^2(g_V^2 + g_T^2) + 2(\frac{3}{5})^{\frac{1}{2}}M_F M_{GT}(g_V g_A - g_\phi g_T)$$

$$b \cdot \ddot{\zeta} = -2\gamma [|M_F|^2 g_V g_\phi + |M_{GT}|^2 g_A g_T] ; \quad \gamma \equiv (1 - \alpha^2 z^2)^{\frac{1}{2}}$$

$$(E) \rightarrow F_o(E) + |M_F|^2 g_\phi^2 + |M_{GT}|^2 g_T^2$$

$$F_o(E) \rightarrow F_i(E) + \delta_{wv} \left(\frac{u}{u+1} \right) (-2) \cdot M_F M_{GT} g_\phi g_T + \alpha'_{wv} \left(\frac{1}{wv} \right) |M_{GT}|^2 g_T^2$$

Figure C.4: "Notes 3"

- * In some limits, Holstein and JTW are equivalent. For simplicity, we will require that JTW's terms $C_A, C_A', C_V, C_V', M_F$, and M_{GT} are entirely real.
- * The physical interpretation of this is that we ~~don't~~ require time-reversal symmetry to be obeyed.
- * We use the following relationships:

$$\begin{aligned} \zeta &= \zeta(E) \rightarrow |\zeta|^2 = |M_F|^{1/2} \cdot (|C_V|^2 + |C_V'|^2) \\ A_B \zeta &= \zeta(E) \rightarrow |\zeta|^2 = |M_{GT}|^{1/2} \cdot (|C_A|^2 + |C_A'|^2) \\ &\quad \text{use the later JTW sign convention.} \\ &\quad \text{Re}[a^* C] = -M_F M_{GT} \cdot \text{Re}[C_V C_A'^* + C_V' C_A^*] \end{aligned}$$

- * Then, via trial and error, we find that the following set of relationships gives consistent results:

$$\begin{aligned} C_V &= C_V'; & a_1 &= \pm \frac{1}{\sqrt{2}} M_F (C_V + C_V') \\ C_A &= C_A'; & g_1 &= \pm \frac{1}{\sqrt{2}} M_{GT} (C_A + C_A') \end{aligned} \} \text{ Thus far, either set of signs is consistent. But they must be opposite.}$$

- * In our code, which evaluates Holstein, we use these:

$$\begin{aligned} g_V &\approx g_V M_F; & M_F &= 1.0; & g_V &= 1.0 \\ g_A &\approx g_A M_{GT}; & M_{GT} &= -0.62376; & g_A &\approx 0.91210 \end{aligned} \} \text{ Note that we believe we know } M_F \text{ better than we know } g_A. \text{ So, to measure "A", we vary } g_A \text{ and leave } M_{GT} \text{ fixed.}$$

- * We'll define some quantities, ρ :

$$\rho_{JTW} = \frac{C_A \cdot M_{GT}}{C_V \cdot M_F}; \quad \rho_{Holstein} = \frac{g_A \cdot M_{GT}}{g_V \cdot M_F} \approx -0.562931$$

* This ρ_{JTW} uses our own definition from PRL.

* Note that A_B comes out physically wrong unless ρ_{JTW} is \oplus ie, in A_B , there's a term $\sim \cancel{M_F M_{GT} \cdot \text{Re}[C_V C_A'^* + C_V' C_A^*]}$ and we need the whole thing to come out \oplus . $\therefore C_V$'s and C_A 's must have opposite signs.

- * We'll take the convention that every body has the same matrix elements:

$$\begin{aligned} M_{GT, JTW} &= M_{GT, Holstein} \\ M_{F, JTW} &= M_{F, Holstein} \end{aligned}$$

- * Then:

$$\begin{aligned} C_V &= C_V' \Rightarrow \oplus \\ C_A &= C_A' \Rightarrow \ominus \end{aligned} \} \text{ This because at the end of the day, we want Holstein's } a_1 \text{ to be } \oplus, \text{ and } g_1 \text{ to be } \ominus, \text{ or else we don't produce the right physics.}$$

$$\begin{aligned} g_V &= \frac{1}{\sqrt{2}} (C_V + C_V') = 1.0 \\ g_A &= \frac{1}{\sqrt{2}} (C_A + C_A') \approx +0.91210 \end{aligned} \} \quad \begin{aligned} C_V &= C_V' = \frac{+1}{\sqrt{2}} g_V = \frac{1}{\sqrt{2}} \\ C_A &= C_A' = \frac{-1}{\sqrt{2}} g_A \approx \frac{-1}{\sqrt{2}} (0.91210) \end{aligned}$$

Figure C.5: "Notes 4"

- * In some limits, Holstein and JTW are equivalent. We require that JTW's terms $C_A, C_A', C_V, C_V', M_F$, and M_{GT} must all be entirely real. We can probably do this WLOG. (Or without very much loss of generality, at least.)

- * Use the following relationships:

$$\xi = f_i(E) \rightarrow |q_i|^2 = |M_F|^2 (|C_V|^2 + |C_V'|^2)$$

$$|c_i|^2 = |M_{GT}|^2 (|C_A|^2 + |C_A'|^2)$$

$$A \cdot \xi = f_n(E) \rightarrow |C_V|^2 = 2 \cdot |M_{GT}|^2 \cdot \text{Re}[C_A C_A'^*]$$

$$\text{Re}[c_i] = -\text{Re}[M_F M_{GT} (C_V C_A'^* + C_V' C_A)] \leftarrow \begin{array}{l} \text{later JTW} \\ \text{convention.} \\ \text{we'll only use this.} \end{array}$$

- * Then, the following relationships give us internally consistent results:

for q_i and c_i :
do I know?!

$$\begin{aligned} C_V &= C_V' ; & a_i &= \pm \frac{1}{\sqrt{2}} M_F (C_V + C_V') \\ C_A &= C_A' ; & c_i &= \mp \frac{1}{\sqrt{2}} M_{GT} (C_A + C_A') \end{aligned} \quad \begin{array}{l} \text{either set of signs is consistent.} \\ \text{But they must be opposite.} \end{array}$$

- * In our code (which evaluates Holstein), we use these values:

\oplus	$a_i \approx g_V M_F$	$M_F = 1.0$	$g_V = 1.0$
\ominus	$C_i \approx g_A M_{GT}$	$M_{GT} = -0.62376$	$g_A = -0.91210$

- * We can also define:

$\rho_{\text{Holstein}} \equiv \frac{g_A M_{GT}}{g_V M_F} \approx -0.568931$	$\rho_{\text{JTW}} \equiv \frac{C_A M_{GT}}{C_V M_F} \leftarrow \text{we use } \rho_{\text{JTW}} \text{ def. in PRL.}$
------------------------------------------------------------------------------	------------------------------------------------------------------------------------------------------------------------

- * We do not get the correct JTW A_β unless we require that ρ_{JTW} is \oplus . Equivalently, we require that $\text{Re}[M_F M_{GT} (C_V C_A'^* + C_V' C_A)]$ must be \oplus . But M_{GT} is \ominus ! \rightarrow Option 1: Take $M_{GT, \text{JTW}} = -M_{GT, \text{Holstein}}$
 \rightarrow Option 2: Take $C_A = C_A'$ to be \ominus , and $C_V = C_V'$ to be \oplus .

(really, there are other options.
 But let's leave M_F and K_V alone.)

- * For Holstein to come out right, we need c_i to be \ominus , and q_i to be \oplus . I think.

$$g_V = \frac{1}{\sqrt{2}} (C_V + C_V') = 1.0$$

$$g_A = \frac{1}{\sqrt{2}} (C_A + C_A') = 0.91210 \Rightarrow C_A \text{ must be } \ominus \text{ then, bc } g_A \text{ is } \oplus \text{ and } M_{GT, \text{Holstein}} \text{ is } \ominus, \text{ and we need } C_V \text{ to be } \oplus.$$

- * OK. Now what do I do with C_A and C_V ? \rightarrow can't just stick them into M_F and M_{GT} . even in JTW it doesn't come out consistent.

- * Have to write JTW in Holstein notation so I can figure out where to put C_A, C_V in.

Figure C.6: "Notes 5"

Appendix D

Derivation of the b_{Fierz} Dependence of the Superratio Asymmetry

Recall the integrated JTW probability distribution for outgoing beta particles from Eq. (B.3):

$$\begin{aligned} d^3\Gamma(E_\beta, \hat{\Omega}_\beta) dE_\beta d^3\hat{\Omega}_\beta &= \frac{2}{(2\pi)^4} F_\mp(Z, E_\beta) p_\beta E_\beta (E_0 - E_\beta)^2 dE_\beta d^3\hat{\Omega}_\beta \xi \\ &\times \left[1 + b_{\text{Fierz}} \frac{m_e c^2}{E_\beta} + A_\beta \left(\frac{\vec{J}}{J} \cdot \frac{\vec{p}_\beta}{E_\beta} \right) \right]. \end{aligned} \quad (\text{D.1})$$

We note that the only angular dependence remaining in this equation is the dot product between the direction of beta emission and the direction of nuclear spin-polarization. This allows us to pull out a further factor of 2π by choosing the axis of polarization as defining our coordinate system, and integrating over the “ ϕ_β ” coordinate. The result is a bit more friendly to work with:

$$d^2\Gamma(E_\beta, \theta) dE_\beta d\theta = W(E_\beta) \left[1 + b_{\text{Fierz}} \frac{m_e c^2}{E_\beta} + A_\beta \frac{v_\beta}{c} |\vec{P}| \cos \theta \right] dE_\beta d\theta, \quad (\text{D.2})$$

where θ is the angle between the beta emission direction and the polarization direction, and is the only angular dependence that remains. Here, we have grouped the overall energy dependence into $W(E_\beta)$, so that

$$W(E_\beta) = \frac{2}{(2\pi)^3} F_\mp(Z, E_\beta) p_\beta E_\beta (E_0 - E_\beta)^2. \quad (\text{D.3})$$

In the TRINAT geometry with two polarization states (+/-) and two detectors (T/B) aligned along the axis of polarization, we are able to describe four different count rates, with different combinations of polarization states and detectors. Thus, neglecting beta scattering effects, we have:

$$r_{T+}(E_\beta) = \varepsilon_T(E_\beta) \Omega_T N_+ \left[1 + b_{\text{Fierz}} \frac{m_e c^2}{E_\beta} + A_\beta \frac{v}{c} |\vec{P}_+| \langle \cos \theta \rangle_{T+} \right] \quad (\text{D.4})$$

$$r_{B+}(E_\beta) = \varepsilon_B(E_\beta) \Omega_B N_+ \left[1 + b_{\text{Fierz}} \frac{m_e c^2}{E_\beta} + A_\beta \frac{v}{c} |\vec{P}_+| \langle \cos \theta \rangle_{B+} \right] \quad (\text{D.5})$$

$$r_{T-}(E_\beta) = \varepsilon_T(E_\beta) \Omega_T N_- \left[1 + b_{\text{Fierz}} \frac{m_e c^2}{E_\beta} + A_\beta \frac{v}{c} |\vec{P}_-| \langle \cos \theta \rangle_{T-} \right] \quad (\text{D.6})$$

$$r_{B-}(E_\beta) = \varepsilon_B(E_\beta) \Omega_B N_- \left[1 + b_{\text{Fierz}} \frac{m_e c^2}{E_\beta} + A_\beta \frac{v}{c} |\vec{P}_-| \langle \cos \theta \rangle_{B-} \right], \quad (\text{D.7})$$

where $\varepsilon_{T/B}(E_\beta)$ are the (top/bottom) detector efficiencies, $\Omega_{T/B}$ are the fractional solid angles for the (top/bottom) detector from the trap position, N_{+-} are the number of atoms trapped in each (+/-) polarization state, and $|\vec{P}_{+-}|$ are the magnitudes of the polarization along the detector axis for each polarization state. $\langle \cos \theta \rangle_{T/B,+-}$ is the average of $\cos \theta$ for *observed* outgoing betas, for each detector and polarization state combination. This latter term is approximately ± 1 as a result of our detector geometry, but contains important sign information. For a pointlike trap in the center of the chamber, 103.484 mm from either (DSSSD) detector, each of which is taken to be circular with a radius of 15.5 mm, we find that $\langle |\cos \theta| \rangle_{T/B,+-} \approx 0.994484$, and is the same for all four cases. Note that a horizontally displaced trap will decrease the magnitude of $\langle |\cos \theta| \rangle$, but as it is an expectation value of an absolute value, all four will remain equal to one another. In the case of a vertically displaced trap, these four values will no longer all be equal, however it will still be the case that $\langle |\cos \theta| \rangle_{T+} = \langle |\cos \theta| \rangle_{T-}$, and $\langle |\cos \theta| \rangle_{B+} = \langle |\cos \theta| \rangle_{B-}$.

In the case of the present experiment, we note that $|\vec{P}_+| = |\vec{P}_-|$ is correct to a high degree of precision.

Appendix E

Derivation of the b_{Fierz} Dependence of the Superratio Asymmetry (Old)

For simplicity, we will henceforth assume that the trap is vertically centered, and take $|\vec{P}_+| = |\vec{P}_-|$. We also define the following:

$$A' = A'(E_\beta) \equiv A_\beta \frac{v}{c} |\vec{P}| \langle |\cos \theta| \rangle \quad (\text{E.1})$$

$$b' = b'(E_\beta) \equiv b_{\text{Fierz}} \frac{mc^2}{E_\beta}, \quad (\text{E.2})$$

and choose a coordinate system in which the + polarization state is, in some sense, ‘pointing up’ toward the top detector, such that

$$\langle \cos \theta \rangle_{T+} \approx +1 \quad (\text{E.3})$$

$$\langle \cos \theta \rangle_{B+} \approx -1 \quad (\text{E.4})$$

$$\langle \cos \theta \rangle_{T-} \approx -1 \quad (\text{E.5})$$

$$\langle \cos \theta \rangle_{B-} \approx +1. \quad (\text{E.6})$$

This allows us to rewrite the four count rates in simplified notation, as:

$$r_{T+} = \varepsilon_T N_+ (1 + b' + A') \quad (\text{E.7})$$

$$r_{B+} = \varepsilon_B N_+ (1 + b' - A') \quad (\text{E.8})$$

$$r_{T-} = \varepsilon_T N_- (1 + b' - A') \quad (\text{E.9})$$

$$r_{B-} = \varepsilon_B N_- (1 + b' + A') . \quad (\text{E.10})$$

We further define the ‘superratio’, s , to be:

$$s = \frac{r_{T-} r_{B+}}{r_{T+} r_{B-}} . \quad (\text{E.11})$$

We are now in a position to define the ‘superratio asymmetry’, A_{super} , as

$$A_{\text{super}} = A_{\text{super}}(E_\beta) \equiv \frac{1 - \sqrt{s}}{1 + \sqrt{s}} . \quad (\text{E.12})$$

This is explicitly an experimental quantity that is measured directly by the above combination of count rates.

Writing the superratio out explicitly in terms of A' and b' , factors of $\varepsilon_{T/B}$ and $N_{+/-}$ cancel out entirely, and we find that

$$s = \frac{(1 + b' - A')^2}{(1 + b' + A')^2} . \quad (\text{E.13})$$

From here it is immediately clear that in absence of other corrections (*e.g.* backscattering, unpolarized background, ...), if $b' = 0$ it follows that $A_{\text{super}} = A'$. In the case where $b' \neq 0$, we find that

$$A_{\text{super}} = \frac{A'}{1 + b'} \quad (\text{E.14})$$

$$\approx A' (1 - b' + b'^2) , \quad (\text{E.15})$$

where we have utilized the assumption that $b' \ll 1$. Thus,

$$A_{\text{super}} \approx A_\beta \frac{v}{c} |\vec{P}| \langle |\cos \theta| \rangle - A_\beta \frac{v}{c} |\vec{P}| \langle |\cos \theta| \rangle \left(b_{\text{Fierz}} \frac{mc^2}{E_\beta} \right) + A_\beta \frac{v}{c} |\vec{P}| \langle |\cos \theta| \rangle \left(b_{\text{Fierz}} \frac{mc^2}{E_\beta} \right)^2 . \quad (\text{E.16})$$

Appendix F

Some Corrections to the Superratio Stuff (Old)

We consider further modifications to the rates described in Eqs. (D.4-D.7). In particular, we consider the effect of non-identical polarization magnitudes for the two polarization states and a trap displaced from the center.

We define for the polarization states:

$$P \equiv \frac{1}{2} (|\vec{P}_+| + |\vec{P}_-|) \quad (\text{F.1})$$

$$\Delta P \equiv \frac{1}{2} (|\vec{P}_+| - |\vec{P}_-|) \quad (\text{F.2})$$

and immediately find that

$$|\vec{P}_+| = P + \Delta P \quad (\text{F.3})$$

$$|\vec{P}_-| = P - \Delta P. \quad (\text{F.4})$$

Further, we also define:

$$\langle |\cos \theta| \rangle_T \equiv \langle |\cos \theta| \rangle_{T+} = \langle |\cos \theta| \rangle_{T-} \quad (\text{F.5})$$

$$\langle |\cos \theta| \rangle_B \equiv \langle |\cos \theta| \rangle_{B+} = \langle |\cos \theta| \rangle_{B-}, \quad (\text{F.6})$$

and

$$\langle |\cos \theta| \rangle \equiv \frac{1}{2} (\langle |\cos \theta| \rangle_T + \langle |\cos \theta| \rangle_B) \quad (\text{F.7})$$

$$\Delta \langle |\cos \theta| \rangle \equiv \frac{1}{2} (\langle |\cos \theta| \rangle_T - \langle |\cos \theta| \rangle_B). \quad (\text{F.8})$$

It immediately follows that

$$\langle |\cos \theta| \rangle_T = \langle |\cos \theta| \rangle + \Delta \langle |\cos \theta| \rangle \quad (\text{F.9})$$

$$\langle |\cos \theta| \rangle_B = \langle |\cos \theta| \rangle - \Delta \langle |\cos \theta| \rangle. \quad (\text{F.10})$$

With this new set of variables defined, we can re-write Eqs. (D.4-D.7) as

$$r_{T+}(E_\beta) = \varepsilon_T(E_\beta) N_+ \left[1 + b' + (A_\beta \frac{v}{c})(P + \Delta P) (\langle |\cos \theta| \rangle + \Delta \langle |\cos \theta| \rangle) \right] \quad (\text{F.11})$$

$$r_{B+}(E_\beta) = \varepsilon_B(E_\beta) N_+ \left[1 + b' - (A_\beta \frac{v}{c})(P + \Delta P) (\langle |\cos \theta| \rangle - \Delta \langle |\cos \theta| \rangle) \right] \quad (\text{F.12})$$

$$r_{T-}(E_\beta) = \varepsilon_T(E_\beta) N_- \left[1 + b' - (A_\beta \frac{v}{c})(P - \Delta P) (\langle |\cos \theta| \rangle + \Delta \langle |\cos \theta| \rangle) \right] \quad (\text{F.13})$$

$$r_{B-}(E_\beta) = \varepsilon_B(E_\beta) N_- \left[1 + b' + (A_\beta \frac{v}{c})(P - \Delta P) (\langle |\cos \theta| \rangle - \Delta \langle |\cos \theta| \rangle) \right] \quad (\text{F.14})$$

and the superratio becomes

$$s = \frac{(1 + b' - (A_\beta \frac{v}{c})(P - \Delta P) (\langle |\cos \theta| \rangle + \Delta \langle |\cos \theta| \rangle)) (1 + b' - (A_\beta \frac{v}{c})(P + \Delta P) (\langle |\cos \theta| \rangle - \Delta \langle |\cos \theta| \rangle))}{(1 + b' + (A_\beta \frac{v}{c})(P + \Delta P) (\langle |\cos \theta| \rangle + \Delta \langle |\cos \theta| \rangle)) (1 + b' + (A_\beta \frac{v}{c})(P - \Delta P) (\langle |\cos \theta| \rangle - \Delta \langle |\cos \theta| \rangle))}$$

where $\varepsilon_{T/B}$ and $N_{+/-}$ still completely cancel out. After a bit of algebra, this simplifies to:

$$s = \frac{(1 + b' - A' + A_\beta \frac{v}{c} \Delta P \Delta \langle |\cos \theta| \rangle)^2 - (A_\beta \frac{v}{c})^2 (\Delta P \langle |\cos \theta| \rangle - P \Delta \langle |\cos \theta| \rangle)^2}{(1 + b' + A' + A_\beta \frac{v}{c} \Delta P \Delta \langle |\cos \theta| \rangle)^2 - (A_\beta \frac{v}{c})^2 (\Delta P \langle |\cos \theta| \rangle + P \Delta \langle |\cos \theta| \rangle)^2} \quad (\text{F.16})$$

Note that in the superratio ΔP and $\Delta \langle |\cos \theta| \rangle$ have cancelled out to first order, and the remaining dependencies are quadratic only. Eq. (F.16) is exact, but still a huge enough expression to be pretty unwieldy to work with. Let's introduce some

shorthand notation to make this less painful:

$$A'' := A_\beta \frac{v}{c} \quad (\text{F.17})$$

$$c := \langle |\cos \theta| \rangle \quad (\text{F.18})$$

$$\Delta c := \Delta \langle |\cos \theta| \rangle \quad (\text{F.19})$$

$$r' := 1 + b' + A_\beta \frac{v}{c} \Delta P \Delta \langle |\cos \theta| \rangle \quad (\text{F.20})$$

In this notation, we find that

$$s = \frac{(r' - A')^2 - (A'')^2 (\Delta P c - P \Delta c)^2}{(r' + A')^2 - (A'')^2 (\Delta P c + P \Delta c)^2}, \quad (\text{F.21})$$

which hurts a lot less to look at. Then, the superratio asymmetry is

$$A_{\text{super}} = \frac{1 - \sqrt{\frac{(r' - A')^2 - (A'')^2 (\Delta P c - P \Delta c)^2}{(r' + A')^2 - (A'')^2 (\Delta P c + P \Delta c)^2}}}{1 + \sqrt{\frac{(r' - A')^2 - (A'')^2 (\Delta P c - P \Delta c)^2}{(r' + A')^2 - (A'')^2 (\Delta P c + P \Delta c)^2}}} \quad (\text{F.22})$$

$$= \frac{\left[\sqrt{(r' + A')^2 - (A'')^2 (\Delta P c + P \Delta c)^2} - \sqrt{(r' - A')^2 - (A'')^2 (\Delta P c - P \Delta c)^2} \right]^2}{\left[(r' + A')^2 - (A'')^2 (\Delta P c + P \Delta c)^2 \right] - \left[(r' - A')^2 - (A'')^2 (\Delta P c - P \Delta c)^2 \right]} \quad (\text{F.23})$$

$$= \frac{\left(\begin{array}{l} 2 \left[(r')^2 + (A')^2 - (A'')^2 ((P \Delta c)^2 + (\Delta P c)^2) \right] \\ -2 \left[(r' + A')^2 - (A'')^2 (\Delta P c + P \Delta c)^2 \right]^{1/2} \left[(r' - A')^2 - (A'')^2 (\Delta P c - P \Delta c)^2 \right]^{1/2} \end{array} \right)}{4 \left[(r' A') - (A'')^2 (P c \Delta P \Delta c) \right]} \quad (\text{F.24})$$